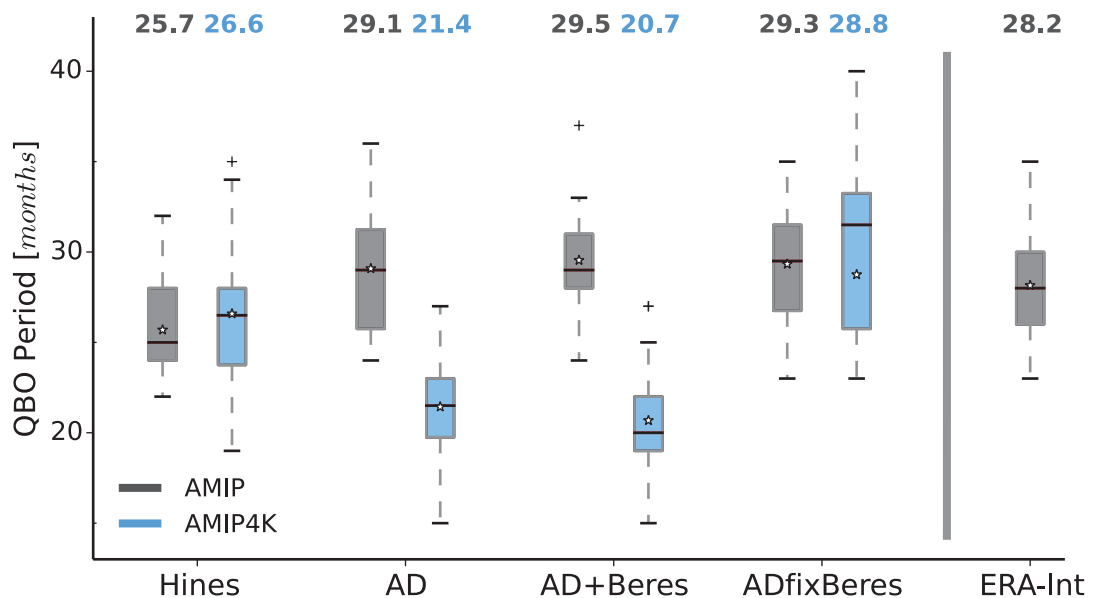




The role of convectively generated gravity waves in driving the Quasi-Biennial Oscillation



Sebastian Schirber

Hamburg 2014

Hinweis

Die Berichte zur Erdsystemforschung werden vom Max-Planck-Institut für Meteorologie in Hamburg in unregelmäßiger Abfolge herausgegeben.

Sie enthalten wissenschaftliche und technische Beiträge, inklusive Dissertationen.

Die Beiträge geben nicht notwendigerweise die Auffassung des Instituts wieder.

Die "Berichte zur Erdsystemforschung" führen die vorherigen Reihen "Reports" und "Examensarbeiten" weiter.

Anschrift / Address

Max-Planck-Institut für Meteorologie
Bundesstrasse 53
20146 Hamburg
Deutschland

Tel./Phone: +49 (0)40 4 11 73 - 0
Fax: +49 (0)40 4 11 73 - 298

name.surname@mpimet.mpg.de
www.mpimet.mpg.de

Notice

The Reports on Earth System Science are published by the Max Planck Institute for Meteorology in Hamburg. They appear in irregular intervals.

They contain scientific and technical contributions, including Ph. D. theses.

The Reports do not necessarily reflect the opinion of the Institute.

The "Reports on Earth System Science" continue the former "Reports" and "Examensarbeiten" of the Max Planck Institute.

Layout

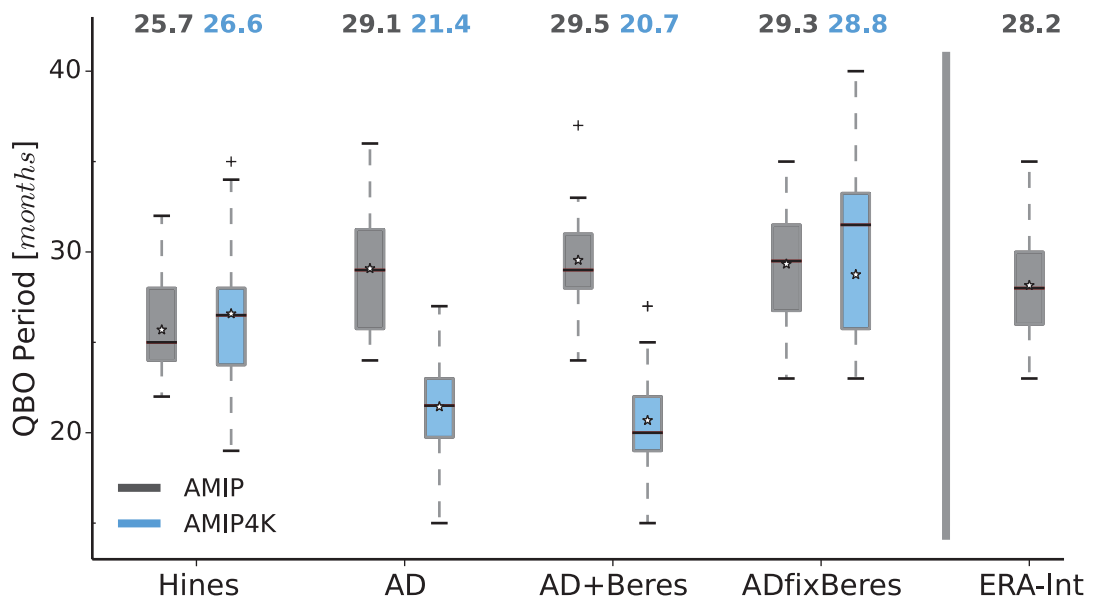
Bettina Diallo and Norbert P. Noreiks
Communication

Copyright

Photos below: ©MPI-M
Photos on the back from left to right:
Christian Klepp, Jochem Marotzke,
Christian Klepp, Clotilde Dubois,
Christian Klepp, Katsumasa Tanaka



The role of convectively generated gravity waves in driving the Quasi-Biennial Oscillation



Sebastian Schirber

Hamburg 2014

Sebastian Schirber

Max-Planck-Institut für Meteorologie
Bundesstrasse 53
20146 Hamburg

Als Dissertation angenommen
vom Fachbereich Geowissenschaften der Universität Hamburg

auf Grund der Gutachten von
Prof. Dr. Bjorn Stevens
und
Dr. Elisa Manzini

Hamburg, den 28.10.2014
Prof. Dr. Christian Betzler
Leiter des Departments Geowissenschaften

Contents

1	Introduction	1
1.1	The Quasi-Biennial Oscillation	2
1.1.1	The QBO mechanism	3
1.1.2	Modeling the QBO	5
1.1.3	The QBO forcing in a GCM	6
1.2	A physically based gravity wave parameterization	8
1.3	How ENSO modifies the QBO	10
1.4	The QBO in a warmer climate	12
2	A convection based gravity wave parameterization	13
2.1	Experimental setup	13
2.1.1	A climate model with three gravity wave parameterizations	13
2.1.2	Mechanisms of a convection based gravity wave scheme and implementation	14
2.1.3	Experiments and observational datasets	17
2.2	A variable source spectrum of gravity wave momentum flux	18
2.2.1	Spatial distribution and seasonality of momentum flux	18
2.2.2	Effect of the background wind on the source spectrum	19
2.2.3	Effect of convective heating properties on the source spectrum	22
2.3	Summary	24
3	Improvements on the QBO	25
3.1	The QBO	26
3.1.1	Comparison with ECHAM6-Hines and ERA-Interim	26
3.1.2	Seasonal effects of parameterized, variable gravity wave sources on the QBO	28
3.2	Discussion and implications for tuning the gravity wave schemes	32
3.2.1	Spectral characteristics of the source momentum fluxes: Tuning the propagation scheme	32
3.2.2	Amplitude of the source spectrum: Tuning for the QBO period	34
3.3	Summary	34
4	Influence of ENSO on the QBO	37
4.1	Experimental setup	37
4.2	Changes in the background state	40
4.2.1	Surface temperature and precipitation	40
4.2.2	Wave activity and upwelling	41

4.3	Evolution of two QBO phases	43
4.3.1	QBOW	43
4.3.2	QBOE	45
4.4	Discussion	47
4.4.1	QBOW	49
4.4.2	QBOE	50
4.5	Summary	50
5	Sensitivity of the QBO to different gravity wave parameterizations in a warmer climate	53
5.1	Experimental Setup	53
5.1.1	Setup of gravity wave parameterizations	53
5.1.2	Source spectra of momentum flux	56
5.2	Results	57
5.2.1	QBO characteristics in a warmer climate	57
5.2.2	Resolved waves and upwelling	60
5.2.3	Gravity wave momentum fluxes and acceleration due to gravity waves	62
5.3	Summary and discussion	64
6	Conclusions	67
6.1	Concluding remarks and outlook	70
	Appendix	vii
	Symbols	ix
	Acronyms	xi
	Abstract (English)	xiii
	Abstract (German)	xv
	Acknowledgements	xvii
	List of Figures	xxiv
	List of Tables	xxv
	References	xxxvi

Chapter 1

Introduction

The stratosphere plays an important role for weather and climate of the earth system. Situated above the troposphere and below the mesosphere, the stratosphere extends from about 15 *km* to 50 *km* in the atmosphere. Instead of being isolated domains, the troposphere and the stratosphere are coupled dynamically, radiatively and chemically. In the stratosphere, ozone absorbs ultraviolet radiation and therefore regulates the incoming solar radiation at the surface. The strong solar absorption of ozone leads to a strong stratification in the stratosphere where temperature increases with height. In contrast to the troposphere, the strong stratification and the lack of abundant water vapor inhibits convection in the stratosphere. Instead, two other processes drive stratospheric dynamics. First, the differential input of energy between the summer pole and the winter pole drives, via thermal wind balance, large scale dynamics in the stratosphere such as the polar vortex in the winter hemisphere and easterlies in the summer hemisphere.

Second, tropospheric waves are a key element in driving stratospheric dynamics. Those waves range from large scale Kelvin, Rossby and Rossby-gravity waves to intermediate inertia-gravity and smaller scale gravity waves (gravity wave). The waves emanate from various tropospheric sources like convection, orography, frontal system or more general instabilities, and propagate into the stratosphere where they deposit energy and momentum when breaking. The exertion and input of momentum into the stratosphere drives several dynamical phenomena such as the prominent Quasi-Biennial Oscillation (QBO) of equatorial zonal winds, one of climate's important phenomenon in the stratosphere. The QBO is driven by equatorial Kelvin waves, Rossby-gravity waves and gravity waves.

Due to the limited spatial resolution of most atmospheric general circulation models (GCM), the effect of unresolved, small scale gravity waves needs to be parameterized. Focusing on the tropics, gravity waves emanate primarily from convection, being highly variable in temporal occurrence and geographical distribution. However, gravity wave parameterizations in the tropics include most commonly constant wave sources. In this thesis we improve the representation of tropical gravity waves in the atmospheric general circulation model ECHAM6. Instead of launching a subjectively prescribed and spatially and temporally constant spectrum of waves, we link the gravity waves to their tropical sources, the convection. The goal of this thesis thereafter is to explore the

benefits of the physically based representation of gravity wave sources on the stratospheric QBO on seasonal, interannual and climatological timescales. More specifically we ask: (I) Does the seasonal cycle in the physically based gravity waves improve QBO quantities on the seasonal timescale? (II) How does the interannual variability of wave activity associated with El Niño / Southern Oscillation project on the QBO? (III) How does a physically based gravity wave parameterization compare to other gravity wave parameterizations with fixed gravity wave sources in driving the QBO in a warmer climate?

In the remainder of this introduction we explain the QBO phenomenology and the QBO mechanism, before we present how models with different complexities simulate the QBO. In more detail, we motivate the implementation of a physically based gravity wave source parameterization. After introducing the effect of El Niño / Southern Oscillation (ENSO) on the QBO forcings on interannual timescales, we close the introduction with the role of gravity wave parameterizations on QBO changes in a warmer climate.

1.1 The Quasi-Biennial Oscillation

The Quasi-Biennial Oscillation (QBO) of equatorial zonal winds is a prominent feature of stratospheric dynamics and a major source of variability in the stratosphere. Characterized by a periodic oscillation with a mean period of ~ 28 months, observed QBO periods range between 22 and 34 months. The alternating jets of the QBO propagate from about 5 hPa downward through the lower stratosphere until the jets dissipate near the region of the tropopause around 100 hPa , see figure 1.1 which shows the QBO in ERA Interim. The wind variance associated with the QBO shows large values between 5 hPa and 40 hPa and peaks around 15 hPa . The easterly jet, with a maximum of $\sim -30 \text{ m/s}$, is stronger than the westerly jet with a maximum of $\sim 15 \text{ m/s}$, yielding a mean QBO amplitude of $\sim 20 \text{ m/s}$. Besides the asymmetry in jet strength, the downward propagation speed of the westerly and easterly jet also differ - the westerly jet descends quicker and more regularly than the easterly jet. For more details on the phenomenology of the QBO see the review by (Baldwin et al., 2001). Summarizing the most peculiar properties of the QBO, Baldwin et al. (2001) point out three features:

- The quasi-biennial periodicity - which is not synchronized with the annual cycle.
- The downward propagation of QBO jets - without the loss of amplitude.
- The super-rotation with a westerly jet at the equator - which violates the conservation of angular momentum.

We will explain and return to these features after presenting the QBO mechanism in the next section.

Being a major source of variability in the middle and lower stratosphere, the QBO affects dynamics and chemical constituents in the stratosphere. Due to thermal wind balance in the lower stratosphere, wind anomalies induce anomalies in temperature, and vice versa. We therefore observe wind and temperature anomalies associated with

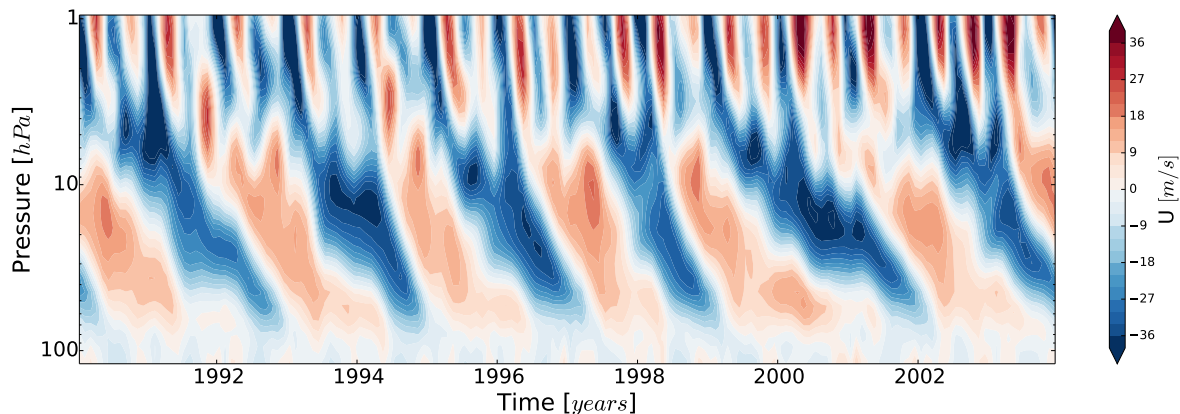


Figure 1.1: The QBO in ERA Interim. Timeseries of meridional (5°N to 5°S lat) and zonal mean zonal wind U in the stratosphere.

the different QBO phases in the middle and lower equatorial stratosphere, which also extend to extratropical latitudes (Randel and Cobb, 1994). The QBO also influences concentrations of several trace gases in the stratosphere, including methane, water vapor and most prominently ozone. Dunkerton and Baldwin (1991) show strong correlations between column ozone and zonal wind of the QBO.

The QBO influences also other parts of the atmosphere, in both the stratosphere and the troposphere. Holton and Tan (1980) show that the easterly phase of the QBO is associated with weakening of the northern wintertime stratospheric polar vortex. Anomalies in the wintertime stratospheric circulation can extend down until the tropospheric surface, see Baldwin and Dunkerton (2001). Recent work shows that the QBO exhibits predictability in the tropics (Pohlmann et al., 2013) and weak predictability in the north Atlantic sector (Scaife et al., 2014), following the physical path of the combined work of Holton and Tan (1980) and Baldwin and Dunkerton (2001). In the tropical troposphere, the QBO also influences tropical cyclone tracks (Ho et al., 2009), the boreal summer monsoon (Giorgetta et al., 1999) and tropical deep convection (Collimore et al., 2003; Liess and Geller, 2012). The presented QBO teleconnections, affecting tropospheric and extratropical regions, highlights the necessity and importance of the QBO - apart from studying wave - mean flow interactions in a fluid on a rotating sphere.

1.1.1 The QBO mechanism

The QBO jets are driven downward by waves which emanate from the troposphere and travel upwards into the stratosphere. At the alternating shear zones of the QBO winds, the waves break in regions where the waves' horizontal phase speed c is close to the wind speed of the QBO, see the illustration in figure 1.2. When breaking, the waves deposit momentum and accelerate the background flow in regions of strongest wind shear which are situated below the QBO jet maxima. The breaking waves accelerate the jets below the jet maxima and therefore cause a downward propagation of the wind maxima. The successive descent of easterly and westerly jets eventually forms an oscillation with a quasi-biennial period, the QBO. In the absence of tropospheric

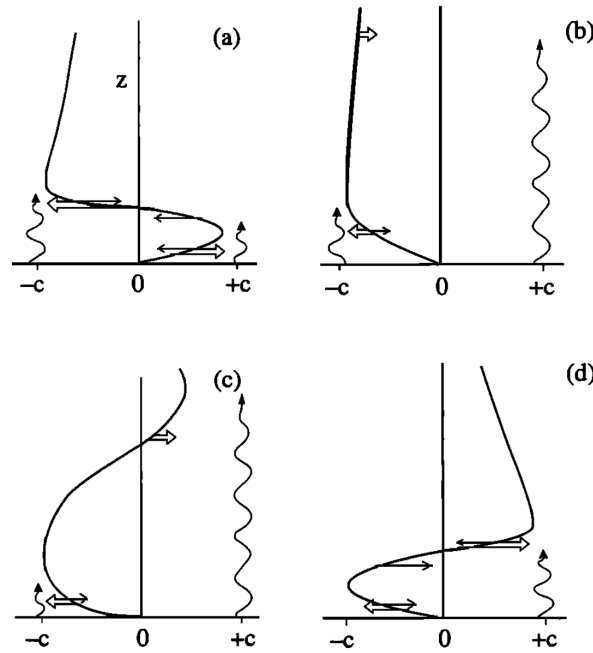


Figure 1.2: The QBO mechanism. Schematic representation of the temporal evolution (a-d) of QBO jets (solid line), driven by vertically propagating waves (curved arrows). Vertical axis depicts height, horizontal axis depicts zonal wind and horizontal phase speed. Double arrows illustrate wave-driven acceleration of the QBO jets, single arrows depict acceleration due to viscosity. Waves break where their horizontal phase speed c is close to the value of the QBO jets, the background wind. Illustration from Plumb (1984); Baldwin et al. (2001).

waves, a stratospheric QBO would not develop. Note that the schematic in figure 1.2 shows only two waves, while in reality waves with a wide range of phase speeds drive the QBO.

The horizontal wavelength of the waves driving the QBO spans several orders of magnitude, from large scale Kelvin and Rossby-gravity waves over inertia-gravity waves to smaller scale gravity wave with shorter horizontal wavelengths. Dunkerton (1997) show that, besides the large scale waves, the contribution of intermediate inertia-gravity waves and mesoscale gravity waves is necessary to produce a QBO with realistic period and amplitude. For more details on the nature, origin and occurrence of gravity waves see the following chapter 1.2 or the review by Fritts and Alexander (2003).

We can explain the above mentioned three features of the QBO phenomenology of Baldwin et al. (2001) considering the presented mechanism. The period of the QBO is primarily driven by the amount of excited large-, medium- and small-scale wave momentum in the troposphere and not by the seasonal cycle. The amount of momentum transported by waves in present day climate leads to a QBO with a period of more than two years. If the amount of excited wave momentum changes, due to an external forcing, the QBO period is expected to adjust to the change in forcing with a change in period. An increase in excited waves is expected to shorten the QBO period, while a decrease in wave activity is expected to prolong the QBO period. When propagating upward, waves transport momentum from the troposphere to the stratosphere and when breaking, waves deposit momentum which constitutes a source of momentum in

the stratosphere. Therefore the jets descend without the loss of amplitude and in the case of the westerly jet, the input of momentum allows for the super-rotation of zonal winds.

1.1.2 Modeling the QBO

In earth system science, knowledge and understanding of processes can generally be gained by observations, theoretical reasoning, physical experiments and numerical models - or a combination of several aspects. Due to the lack of comprehensive observations in certain cases or due to the complexity of the earth system, theoretical reasoning, laboratory experiments and numerical models often play a crucial role in gaining knowledge and physical understanding. In particular numerical models are used to prove, challenge or falsify hypothesis of the mechanisms of physical processes. In the case of the QBO, observations of stratospheric zonal wind and temperature allow a detailed description of the phenomenology of the QBO, see the previous chapter and Baldwin et al. (2001). However in the past, observations did not allow to shed light on the mechanisms of QBO dynamics. Numerical models, and in particular simple conceptual one- (1D) and two-dimensional (2D) models, helped to reveal the physical mechanisms behind the quasi-biennial oscillation of stratospheric zonal winds.

Using a simple model with no rotation, Lindzen and Holton (1968) were the first to show that a QBO develops considering only (I) tropospheric waves that travel upward and break in the stratosphere and (II) vertical diffusion, yielding the tendency equation of momentum

$$\overline{u_t} = -\frac{F_z}{\rho} + \frac{\nu}{\rho}(\overline{\rho u_z})_z \quad (1.1)$$

with zonal wind $u(z)$, constant mean kinematic viscosity ν , density ρ and total wave momentum flux $F(t, z)$ in $[kg/(m \cdot s^2)]$ with $F_z(u_z)$. Subscripts denote derivatives, overbars denote the zonal mean. The model was revisited by Holton and Lindzen (1972) before Plumb (1977) showed that the model also sustains a QBO with only two discrete internal gravity waves with opposing phase speeds. Plumb and Bell (1982) find in a 2D model that the QBO induces, via thermal wind balance, a secondary circulation in the meridional plane. The combined effect of the horizontal and vertical advection of the secondary circulation inhibits the downward propagation of both easterly and westerly QBO jets. Furthermore, Saravanan (1990) finds that also the tropical upwelling, the ascending branch of the Brewer-Dobson circulation (Brewer, 1949; Dobson, 1956), opposes the downward propagation of the QBO. Therefore, the combination of the self-induced secondary circulation of the QBO and the tropical upwelling counteracts the tropospheric wave forcing of the QBO. The previous findings with simple numerical models are supported by laboratory experiments (Plumb and McEwan, 1978), observations including the detailed divergence of wave momentum flux at QBO shear zones (Ern et al., 2014) and more complex state-of-the-art numerical models. Summarizing all relevant mechanisms influencing the QBO, the tendency equation of momentum for a simple 1D model yields

$$\overline{u_t} = -\frac{F_z}{\rho} + \frac{\nu}{\rho}(\overline{\rho u_z})_z - \overline{w \cdot u_z} + SC \quad (1.2)$$

with vertical velocity $w(z)$ of the Brewer-Dobson circulation and the effects of the secondary circulation $SC(u)$.

Increasing the complexity of numerical models by further spatial dimensions, three-dimensional general circulation models (GCM) cover the entire globe in order to simulate the general circulation of the atmosphere more realistically. Acknowledging the importance of the stratosphere in atmospheric sciences and the dynamical coupling between the troposphere and the stratosphere (Baldwin and Dunkerton, 2001), coupled ocean-atmosphere GCMs begin to incorporate the stratosphere by extending and increasing the vertical resolution in so-called “High-top models”. In this work we employ the 6th version of the atmospheric GCM ECHAM, developed at the Max-Planck-Institute for Meteorology (MPI) in Hamburg (Stevens et al., 2013). The high-top model ECHAM6 is the atmospheric component of an earth system model with several components including the ocean, sea ice, land processes and a carbon cycle (Giorgetta et al., 2013).

For computational reasons, state-of-the-art earth system models are truncated at fairly coarse spatial resolutions, typically of the order of 100 *km*. Many physical processes with substantial impact on the large-scale state, such as precipitation formation, radiative transfer, turbulence, convection and waves with short wavelengths occur at much smaller scales. We represent these small-scale processes in earth system models by so-called “parameterizations”. Parameterizations are statistical-, empirical-, theoretical- or heuristic-based formulations which determine the effect of unresolved processes on the resolved state - in terms of the resolved state itself.

Regarding the QBO, also lower dimensional numerical models include parameterizations taking into account the effect of waves, of diffusion, of upwelling or of the secondary circulation (Lindzen and Holton, 1968; Saravanan, 1990; Dunkerton, 1997)). GCMs with increased dimensions and higher resolution intrinsically include the effects of equatorial upwelling and the secondary circulation and thus GCMs do not need to parameterize these processes. However depending on the horizontal resolution, GCMs resolve only a fraction of the waves which force the QBO. Several GCMs, with sufficiently high horizontal resolution, succeed in generating a QBO or produce QBO-like oscillations (Hamilton et al., 1999; Watanabe, 2005; Watanabe and Miura, 2008). Because a high model resolution is computationally expensive, many GCMs exhibit a coarser resolution than necessary to cover the full range of waves driving the QBO. Due to the limited resolution of current GCMs, the effect of unresolved gravity waves generally needs to be parameterized before GCMs can produce a QBO (Scaife et al., 2000; Giorgetta et al., 2002; Shibata and Deushi, 2005; Richter, 2014). Gravity wave parameterizations remain an essential ingredient in many GCMs which generate a QBO, especially in the case of fully coupled state-of-the-art earth system models which are usually employed to run comprehensive climate change simulations.

1.1.3 The QBO forcing in a GCM

In order to understand changes in the QBO phenomenology, such as due to a warmer climate, we need to assess the different forcing mechanisms acting on the QBO. Combining the previous two chapters on the QBO mechanisms and on QBO modeling,

we identify the following QBO mechanisms in general circulation models. In a GCM with a gravity wave parameterization, we separate the waves driving the QBO into (I) resolved, large scale waves and (II) unresolved, parameterized gravity waves. The advection term consists of (III) the horizontal and vertical component of the self-induced secondary circulation and (IV) the vertical upwelling associated with the ascending branch of the Brewer-Dobson circulation in the tropics. While the tropospheric wave components (I) and (II) drive the QBO, the net effect of both advection-related components (III) and (IV) oppose the wave forcing. While we can diagnose the net effect of advection on the QBO in the transformed Eulerian mean (TEM) framework, isolating the components (III) and (IV) from the net advective tendencies is non trivial. Considering a broad latitudinal band which includes both the ascending and descending branch of the secondary circulation of the QBO, we can construct a proxy for the tropical upwelling (IV), independent of (III). Thus whenever showing upwelling w^* in this thesis, we average meridionally between at least -25° and $+25^\circ$ latitude.

The effect of the secondary circulation (III) on the QBO is independent of external influences and depends solely on the strength of the QBO amplitude. Therefore we only call (I), (II) and (IV) “QBO forcings”, because those mechanisms can change externally due to changes in the troposphere or stratosphere. Other studies (Krismer and Giorgetta, 2014) relate the term “QBO forcing” to the tendency of zonal wind $\frac{\partial U}{\partial t}$ which acts on the QBO and causes the downward propagation of the QBO. We deviate from this definition in this work. Because the individual tendency components also depend strongly on the QBO amplitude, we can’t unambiguously assign changes in the tendency components to changes in the forcing - in cases when also the QBO amplitude changes. For more details see chapter 4.4 and figure 4.12. In this thesis, we therefore relate “QBO forcing” to the general process causing the change in tendency. In detail, we relate “QBO forcing” to physical quantities expressing the general process, such as momentum flux B for gravity waves, the vertical component F_z of the Eliassen-Palm (EP) flux vector for resolved waves and the vertical velocity w^* of a transformed Eulerian mean analysis for the tropical branch of the Brewer-Dobson circulation, i.e. the upwelling.

In this thesis we focus on the tropics and try to isolate the effects of the gravity waves (II) on the QBO. Therefore we try to minimize changes in the remaining two QBO forcings, the resolved waves (I) and the upwelling (IV). While we diagnose the changes of (I), we can limit changes in (IV) due to a particular experimental setup. The Brewer-Dobson circulation, and therefore the strength of tropical upwelling, is driven primarily by waves, resolved and parameterized, outside the tropics. Keeping the gravity wave parameterization in the extratropics unchanged minimizes changes in the forcing of the Brewer-Dobson circulation in all experiments. This experimental setup aims at minimizing changes in the Brewer-Dobson circulation and therefore changes in the QBO forcings due to tropical upwelling. This approach is important for chapters 3 and 5 and for details on the experimental setup see chapter 2.1.1.

1.2 A physically based gravity wave parameterization

Several gravity wave parameterizations include two simplifying assumptions about the momentum flux source spectrum and the amount of excited momentum flux of gravity waves: (I) the source spectrum's shape of excited gravity waves is prescribed and (II) the amount of excited gravity wave momentum flux is constant in space and time. However observations deviate from these assumptions: (I) gravity waves emanate from multiple sources which each show unique spectral characteristics depending on the source (Alexander et al., 2010). Besides orographically based gravity waves, whose effects are usually represented by a separate parameterization (McFarlane, 1987; Lott and Miller, 1997), gravity waves are generated by frontal systems, convection and more general tropospheric instabilities. (II) These sources exhibit high spatial and temporal variability, implying similar variability for the excited gravity waves; for more details on gravity waves see the review paper by Fritts and Alexander (2003). Focusing on the tropics, theoretical (Salby and Garcia, 1987), observational (Pfister et al., 1993; McLandress et al., 2000; Jewtoukoff et al., 2013; Geller et al., 2013) and numerical studies (Alexander and Holton, 1997; Piani et al., 2000; Lane et al., 2001; Song et al., 2003) attribute gravity wave activity in the stratosphere to the underlying convection. In the tropics it is therefore reasonable to assume that convection plays the dominant role in gravity wave generation. For an illustration of gravity waves excited by tropospheric convection, see figure 1.3 with result from a case study with a non-hydrostatic 2D cloud resolving model, performed by Holton and Alexander (1999). Due to the condensation of water vapour, a squall-line releases heat in the troposphere, extending from the surface to tropopause regions at ~ 14 km. The buoyancy anomaly in temperature associated with the tropospheric heating propagates vertically into the stably stratified stratosphere above. Gravity waves inherit their name from the restoring force, gravity, that acts on buoyancy anomalies in stably stratified fluids.

Physically based gravity wave source parameterizations take account of gravity waves excited by convection (Chun and Baik, 2002; Beres et al., 2004; Choi and Chun, 2011). This class of parameterizations generates an interactive source spectrum based on the latent heating properties and the background wind, respectively parameterized and resolved in GCMs. The advantages of such an approach concentrate on the following aspects. First, the amount of excited momentum flux shows a model-intrinsic temporal and spatial variability which, second, is also prone to changes on seasonal, interannual and climatological timescales. Third, the spectral shape depends on the physical properties of the parameterized convective event, which removes the need to subjectively prescribe the shape of the source spectrum. The last aspect is emphasized by McLandress and Scinocca (2005) who show that three different gravity wave propagation schemes can be tuned in a way to yield nearly identical responses on the profiles of wind tendencies. The authors conclude that models would benefit rather from a more realistic source spectrum than from a better dissipation mechanism.

Several model studies implement aspects of a convection based gravity wave source parameterizations into GCMs. Whereas Geller et al. (2011) add a prescribed seasonal variation in space and time on the amplitude of prescribed gravity waves, Richter et al.

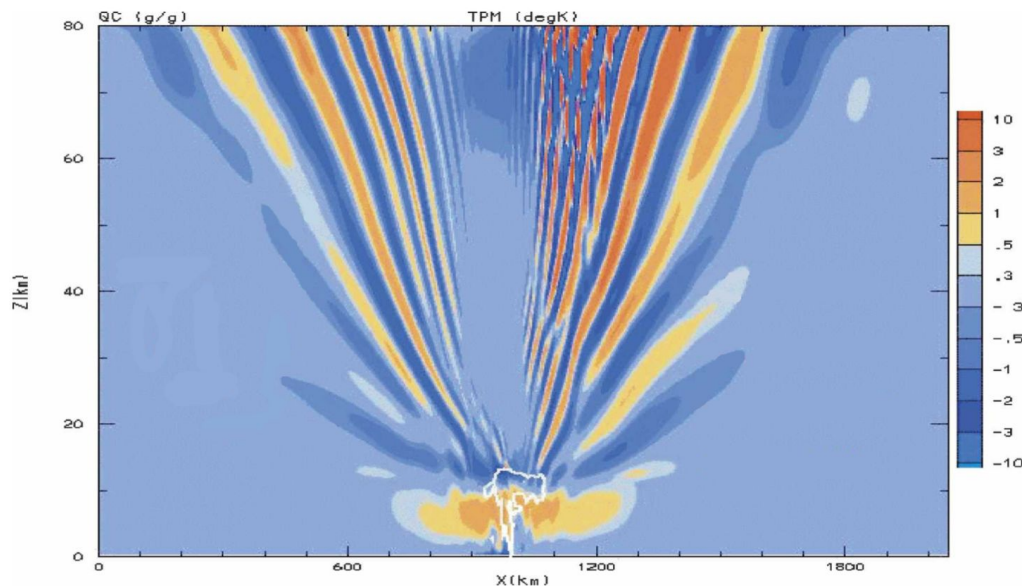


Figure 1.3: gravity waves excited by a squall-line modeled with a 2D cloud resolving model. Background colors show temperature perturbations of gravity waves in K and the white contour shows the location of the convective heating in the troposphere. The horizontal axis shows the horizontal extent in km , the vertical axis height in km . Figure adopted from Alexander and Barnet (2007).

(2010) present a configuration of the Whole Atmosphere Community Climate Model (WACCM) with entirely physically based gravity wave source parameterizations. Lott and Guez (2013) simulate a QBO with the GCM LMDz, introducing a stochastic gravity wave parameterization in which the waves' amplitudes are directly linked to the modeled precipitation. Concentrating on the QBO, Kim et al. (2013) show improvements of the simulated QBO in the Met Office Unified Model due to an implementation of the source parameterizations after Choi and Chun (2011), which generates roughly 50% of the total gravity wave fluxes in the tropics. The authors show a greater variability of QBO periods, which is closer to observations, and a strengthening of the annual cycle of zonal winds.

In this work, we implement a convection based gravity wave scheme which represents the unique source of tropical gravity waves in the atmospheric GCM ECHAM6. In chapter 2 we first introduce the gravity wave scheme conceptually and elaborate the physical links to the underlying convection. After presenting the seasonality of gravity wave source strength we show how spatially varying background winds change properties of the gravity wave source spectra. We further isolate the physical input properties which dominate the different spectral characteristics of the gravity wave source spectra. Finally we highlight the sensitivity of the gravity wave source parameterization to the underlying convection scheme and compare the heating depths statistics of convection, which is parameterized in the model, to derived observations.

Given the chosen experimental setup of a physical based gravity wave parameterization

as the only source of gravity waves in the tropics, we are able to show the full effect of the source variability on the stratospheric QBO. In chapter 3 we first show the effects of the implemented gravity wave parameterization setup focusing on improvements on the QBO amplitude. By further applying an EOF analysis on the timeseries of zonal wind we show the link between the amount of the exerted acceleration and the downward propagation rate of the QBO jets. We end chapter 3 with a focus on seasonality of the downward propagation rate of the QBO jets, comparing a GCM with constant gravity wave sources and a GCM with physically based gravity wave sources with radiosonde observations of zonal wind.

1.3 How ENSO modifies the QBO

El Niño / Southern Oscillation (ENSO) strongly changes the atmospheric and oceanic state on interannual timescales. The phenomenon originates in the Pacific and is characterized by two opposing phases of an oscillation, El Niño and La Niña. During El Niño conditions, positive SST anomalies dominate the central and eastern pacific, while negative SST anomalies prevail during La Niña conditions. SST anomalies during ENSO events are associated with changes in atmospheric temperature, precipitation, sea level pressure, zonal winds and thermocline depth in the upper ocean (Trenberth and Caron, 2000). The anomalies for both El Niño and La Niña peak during northern hemispheric winter and the period of the oscillation varies between 2 and 7 years. For an overview on the definition of ENSO see Trenberth (1997) and for a review on ENSO variability see Wang and Fiedler (2006).

In the tropics, anomalous sea surface temperatures lead to anomalies in precipitation (Soden, 2000). Anomalous precipitation is a manifestation of changes in convective activity and consequently changes in the excited equatorial waves (Bergman and Salby, 1994; Alexander and Holton, 1997; Tsuda et al., 2009). In detail, an increase in temperature and precipitation during El Niño is a manifestation of increased wave activity, and vice versa during La Niña (Wang and Geller, 2003; Wang and Alexander, 2010). Anomalous tropospheric wave activity influences the two general QBO forcing mechanisms. On one hand an increase in tropospheric wave activity during El Niño leads to an increase of stratospheric wave forcing of the QBO, and vice versa for La Niña (Pfister et al., 1993). On the other hand, an increase in wave activity during El Niño also leads to an intensification of the Brewer-Dobson circulation, which is associated with an increase in upwelling in QBO regions (Hardiman et al., 2007; Randel et al., 2009). Consequently, during La Niña the suppressed wave activity is expected to lead to a weaker upwelling in the lower stratosphere. Because the QBO forcing due to upwelling counteracts the stratospheric wave forcing of the QBO, an ad hoc estimate of which mechanism dominates during El Niño and La Niña is difficult. Therefore modeling and observational studies analyze the effect of ENSO on the QBO. Apart from several studies which do not identify an ENSO signal in the QBO (Angell, 1986; Barnett, 1991; Kane, 1992, 2004), one observational (Taguchi, 2010) and one model study (Calvo et al., 2010) show a modulation of the QBO due to ENSO.

The observational study by Taguchi (2010) analyzes radiosonde data of 55 years of monthly mean zonal wind in an EOF space, inspired by Wallace et al. (1993) and

similar to the analysis in chapter 3.1.2. The study shows a weaker QBO amplitude during El Niño compared to during La Niña conditions with the westerly phase of the QBO dominating the amplitude reduction. The authors further show a faster QBO downward propagation rate during El Niño conditions, dominated by the westerly QBO phase. The easterly QBO phase also shows a faster downward propagation rate, but results are statistically insignificant. The observational studies suffer several shortcomings: (I) The chosen EOF method represents the QBO amplitude and the QBO phase propagation in a compact two-dimensional space which allows to apply straightforward statistics. However this approach also entails disadvantages, because the EOF analysis incorporates an integral value for QBO properties between 10 *hPa* and the QBO base at ~ 80 *hPa*. In this vertical range, both easterly and westerly QBO phases are always simultaneously present. Therefore the chosen EOF analysis of zonal winds provides an integral value for both easterly and westerly QBO phase. However the chosen EOF analysis is not able to relate QBO properties to a certain QBO phase in an unambiguous way. (II) The observational record also includes other forcings like volcanic eruptions or long term solar variability, which possibly contaminates the ENSO signal in the observational record. Yuan et al. (2013) extend the work of Taguchi (2010), repeating the analysis with a different set of radiosonde data and observing similar results. Considering the above shortcomings, we summarize only the most sound findings by neglecting the separation into easterly and westerly QBO phases: During El Niño conditions the QBO amplitude reduces and the QBO downward propagation speed increases, compared to during La Niña conditions.

The model study by Calvo et al. (2010) uses the GCM MAECHAM5, the middle atmosphere configuration of ECHAM5, to perform a 100 year long control run with climatological mean SSTs. Selecting distinct QBO easterly and westerly phases in the control simulation, the authors repeat, for each selected phase, the simulations for 14 months replacing the climatological SSTs with SSTs of the strong El Niño 1997/1998. Combining all easterly and all westerly QBO phases of the control run and the El Niño runs to an ensemble, the authors find no change in QBO amplitude for both easterly and westerly QBO phases. While the QBO downward propagation rate for the easterly jet shows no change, the QBO downward propagation rate of the westerly jet increases during El Niño conditions. The authors attribute the increased downward propagation rate of the westerly jet to an increase in wave activity during El Niño condition compared to the control run. Note that the employed model uses a gravity wave parameterization with prescribed and constant gravity wave sources which are not subject to react to the changed tropospheric conditions of El Niño.

Both the observational and model study contribute to understanding the effect of ENSO on the QBO but also lack aspects necessary to deeper understand the presented results. The observational study focuses on the phenomenology of the QBO during ENSO, omitting the physical mechanisms that cause changes in QBO properties. However observations of stratospheric upwelling and wave activity, with the necessary degree of detail and temporal resolution to explain QBO changes due to ENSO, are not available. The modeling study omits to present the changes in upwelling due to ENSO. In addition, the employed gravity wave parameterization includes constant gravity wave sources which do not follow changes of the tropospheric background state, which occur during ENSO. Finally the modeling study only compares a single El Niño event with

a climatological mean, omitting the effect of La Niña conditions.

In chapter 4 we present results from a model study which includes an analysis of all three QBO-driving mechanisms of a GCM in a comprehensive experimental setup. We first show changes due to ENSO (I) in the resolved waves, (II) in the parameterized waves, which are physically based in this study, and (III) in the upwelling in a comprehensive, idealized model framework. We further analyze the changes between El Niño and La Niña conditions for two distinct phases of the QBO. We choose, for the first time, a comprehensive approach to show how changes of all QBO driving mechanisms, due to ENSO, affect the QBO.

1.4 The QBO in a warmer climate

In a future, warmer climate the QBO behaviour is strongly dependent on the employed model. On one hand, Giorgetta and Doege (2005) show a shortening of the QBO period in a doubled CO₂ climate, because they prescribe an increased activity of parameterized gravity waves in the warmer climate. On the other hand, two variants of the Model for Interdisciplinary Research on Climate (MIROC) show a lengthening of the QBO period, along with a decrease in the QBO amplitude under future climate conditions (Kawatani et al., 2011; Watanabe and Kawatani, 2012). Analyzing four models (HadGEM2-CC, MPI-ESM-MR and two variants of MIROC-ESM) of the Coupled Model Intercomparison Project Phase 5 (CMIP5), Kawatani and Hamilton (2013) associate an increased upwelling with a decrease in QBO amplitude in the lower stratosphere. While the decrease in QBO amplitude is consistent within all four models and also with observations, changes in QBO period differ between models, even in sign. While HadGEM2-CC shows a shorter QBO period, the two MIROC-ESM variants show a longer QBO period in a future climate, and MPI-ESM-MR shows a lengthening before the year 2000 followed by a shortening of the QBO period thereafter (Kawatani and Hamilton, 2013, supplementary information).

All four models, analyzed by Kawatani and Hamilton (2013), employ gravity wave parameterizations with prescribed, constant gravity wave sources which are generally tuned, within the range of observational constraints, in present day climate. In chapter 5, we analyze the sensitivity of QBO changes, due to a warmer climate, to different tropical gravity wave parameterization setups within the same model framework. This is the first time that multiple gravity wave parameterizations in the tropics are systematically analyzed within the same model framework with respect to QBO changes in a warmer climate. This approach helps to quantify the contribution of gravity wave parameterizations to the spread in simulated QBO period changes of CMIP5 models.

Chapter 2

A convection based gravity wave parameterization in a general circulation model: Implementation and the physical link to sources

In this chapter we document the experimental setup of the different gravity wave parameterizations employed in ECHAM6 with a focus on the newly implemented convection based gravity wave parameterization. The new gravity wave scheme introduces spatial and temporal variability in the amount of excited gravity wave. We further show how physical properties, like the convective heating and the background wind, determine the nature and properties of the excited gravity waves. We close the chapter with a comparison of the parameterized convective heating characteristics with observations and discuss the effects of the comparison on the gravity wave source properties.

2.1 Experimental setup

2.1.1 A climate model with three gravity wave parameterizations

We use the atmospheric general circulation model ECHAM6 (Stevens et al., 2013), the latest version of the atmospheric component of the earth system model developed at the Max Planck Institute for Meteorology (MPI-ESM) (Giorgetta et al., 2013). The simulations performed here use a spectral truncation at wavenumber 63 and an associated Gaussian grid of $\sim 1.9^\circ$ resolution. The vertical grid consists of 95 hybrid sigma pressure levels, with a spacing of roughly 700m in the lower stratosphere, resolving the atmosphere from the surface up to 0.01 hPa. In ECHAM6 the parameterization of cumulus convection is based on the mass-flux scheme by Tiedtke (1989) with modification for deep convection incorporated by Nordeng (1996). The model parameterizes the effects of unresolved, non-orographic gravity waves with a scheme after Hines which

is based on the Doppler spread theory (Hines, 1997a,b). The prescribed spectrum of waves emanating from the troposphere is broad band with constant amplitude in time and space, although in the standard model setup, a latitudinal amplitude enhancement is introduced around the equator in order to obtain a QBO with a realistic period (Schmidt et al., 2013). For details on the middle atmospheric circulation of ECHAM6 see Schmidt et al. (2013) with a description of the QBO and the resolved waves in Krismer et al. (2013).

In addition to the Hines scheme, we implement the convection based gravity wave source parameterization after Beres et al. (2004) which is coupled to the gravity wave propagation parameterization after Alexander and Dunkerton (1999, hereafter AD99). Since convection is the primary source of tropical gravity wave, which are covered by the Beres scheme, we disable the Hines scheme within the tropics (latitude $|\Phi| \leq 20^\circ$) entirely by setting u_{rms} , the parameter for the source strength, to 0 m/s . Outside the tropics, the Hines scheme increases linearly between $20^\circ \leq \Phi \leq 30^\circ$ and remains constant with u_{rms} at 1 m/s in the extratropics ($|\Phi| \geq 30^\circ$). This somewhat arbitrary latitudinal partition of the two gravity wave parameterizations is based on the latitudinal extent of the Beres scheme, shown in figure 2.2 which is discussed in more detail in chapter 2.2. The orographic gravity wave scheme (Lott and Miller, 1997) is primarily active in the extratropics and remains untouched in this model setup. For a schematic overview of the three gravity wave parameterizations in this model setup see figure 2.1. In the chosen setting with the non-orographic Hines and Beres gravity wave source parameterizations, the Beres scheme produces additional wave momentum flux in the extratropical regions of the storm tracks. We decide to include this contribution for two reasons: first the additional acceleration does not deteriorate the model's zonal mean circulation (not shown); second an arbitrary and artificial latitudinal restriction to the tropics is not based on physical arguments.

2.1.2 Mechanisms of a convection based gravity wave scheme and implementation

The Beres scheme produces a spectrum of gravity waves depending on the latent heating properties and the background wind in grid boxes with active, parameterized convection. The parameterization generates an individual distribution of wave momentum flux $B_0 = \overline{u'w'}$ in [m^2/s^2] as a function of horizontal phase speed c in [m/s]. The shape and amplitude of the individual source spectra are dependent on the heating depth, the heating rate, the mean wind in the heating region and several prescribed parameters, each described briefly in the following paragraphs. For a more quantitative description including a theoretical derivation and detailed equations for the spectrum of source momentum flux see Beres et al. (2004).

The vertical extent of condensational heating within a cloud, the heating depth H_q , governs the dominant vertical wavelength of the excited waves. Since the vertical wavelength translates to a horizontal phase speed, the heating depth determines the position of the maxima in the phase speed spectrum: Large heating depths generate gravity wave spectra peaking at high phase speeds, whereas small heating depths generate gravity wave spectra peaking at low phase speeds. Being an equally important

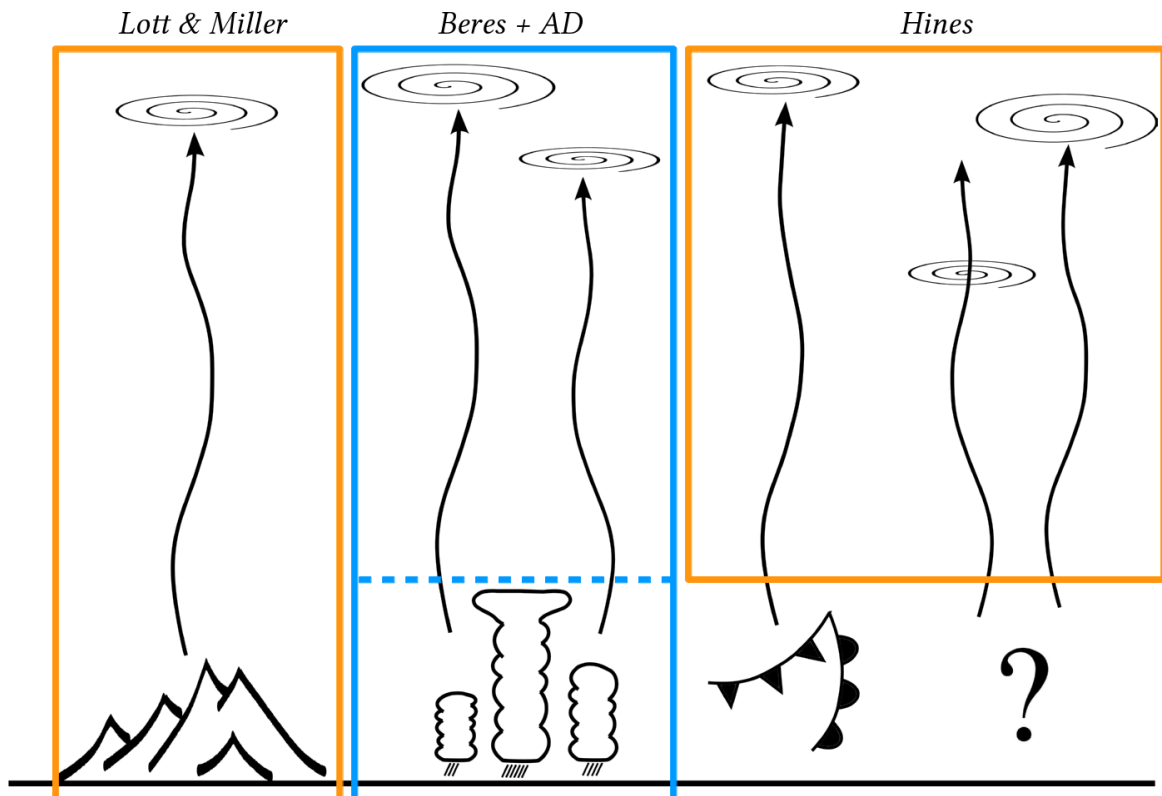


Figure 2.1: Illustration of the setup of gravity wave parameterizations. The *Lott & Miller* scheme parameterizes orographic gravity waves and the *Hines* schemes covers frontal system and more general instabilities (orange). The implemented, convectively based *Beres* gravity wave source parameterization is coupled to the gravity wave propagation parameterization *AD* (blue). While the *Lott & Miller* and the *Beres + AD* schemes include the link to physical sources, *Hines* launches gravity waves independent of the physical background state. The illustration does not account for the schemes' spatial distribution of gravity wave activity.

input variable, the vertical mean heating rate Q_0 strongly influences the overall amount of momentum flux, the wave’s amplitude. In the employed GCM, the convection parameterization does not provide information about individual convective events and the associated heating properties, like Q_0 , of these sub-grid scale events. The bulk mass flux scheme rather gives mean heating properties of all single convective events occurring within one gridbox. Under the assumption that the mean effect of all individual convective events is realistically represented by the bulk scheme, we estimate the heating rate in a simple approach as

$$Q_0 = \frac{Q_{max}}{C_F}$$

with Q_{max} being the peak heating rate within the GCM grid box and C_F the fraction of convection, which is assumed to be a constant 3.5% of a grid box. We highlight that the heating rate acts strongly nonlinear on the wave amplitudes: $B_0 \propto Q_0^2$, see equation (30) in Beres et al. (2004). Therefore the heating rate characteristics of the convection scheme, and in particular heating rate distributions at different heating depths, are crucial for the shape of the gravity wave source spectrum.

The horizontal wind shear across the vertical extent of the heating governs the asymmetries of the source spectra. The wind shear across the vertical extent of the heating is approximated as the mean wind across convection relative to the wind at 700 hPa ΔU with

$$\Delta U = \frac{1}{H_t - H_b} \int_{H_b}^{H_t} (u(h) - u_{700}) dh$$

with H_b the cloud base and H_t the cloud top, $u(h)$ the horizontal wind speed projected onto the plane of the horizontal wind at 700hPa, u_{700} , which is assumed to act as the steering level of the convective cell. Given a positive mean wind ΔU , momentum fluxes with negative phase speeds relative to u_{700} dominate the spectrum and vice versa (Pfister et al., 1993). The reason for this upstream enhancement of momentum fluxes is twofold. On one hand, a mechanism similar to critical level filtering reduces momentum fluxes of waves propagating in the direction of the storm-relative mean wind. On the other hand, a mechanism similar to the “obstacle effect“ increases momentum fluxes of waves propagating in the opposite direction of the storm-relative mean wind; see Beres et al. (2002) for a more detailed explanation. The horizontal orientation of phase speeds is determined by the steering level of a convective cell, chosen as the horizontal wind at 700hPa. Analogously to the assumption in the previous paragraph about mean gridbox heating, we assume that the mean gridbox values of wind are representative for wind of the convective fraction of the gridbox. In the two azimuths of wave orientation, the phase speeds are Doppler shifted with respect to the wind speed at 700hPa. The source spectrum spans waves from $-100m/s$ to $100m/s$ with a resolution of $1m/s$.

In contrast to the preceding input variables which are interactively given by the GCM at each timestep, the source parameterization also requires several constant parameters which need to be prescribed. Following the nomenclature from Beres et al. (2004), we use $L = 1000km$ for the spatial averaging domain and $\sigma_x = 3.5km$ for the horizontal extent of the individual convective cell. The parameterization initiates waves only when

the convection scheme is active and omits shallow convection by applying a minimum heating depth of $2.5km$. In order to account for the earth's sphericity, the source spectrum is scaled by latitude with $B = \rho_0 \cdot B_0 \cdot \cos(\Phi)$. Waves are launched at the cloud top, with ρ_0 in B the density at cloud top, from where the propagation routine by Alexander and Dunkerton (1999) calculates for each individual phase speed bin its corresponding breaking level in the atmosphere above. The scheme with modifications after Ortland and Alexander (2006) is based on the simple assumption that momentum fluxes carried by waves are deposited entirely at the initial onset of linear instability. Given the background wind and density profiles, this concept allows a mapping of a tropospheric spectrum of momentum flux to mean flow acceleration in the layers above. We use a horizontal wavelength $\lambda_h = 100km$ and an intermittency factor $\epsilon = 0.003$. For a detailed explanation of the concept of intermittency see Alexander and Dunkerton (1999). In our application with 201 discretely resolved spectral phase speed bins, $\epsilon \cdot 201 \simeq 0.6$ describes the occurrence of any spectral point, a value of order one.

2.1.3 Experiments and observational datasets

We explore the effects of the Beres gravity wave source parameterization coupled to AD99 (ECHAM6-Beres) in a 30 year atmospheric simulation with prescribed climatological sea surface temperatures (SST) and sea ice concentrations (SIC), compiled from observed SSTs and SICs. We use monthly mean values of a 30 year period for figures 2.2 and 2.4, but 6-hourly instantaneous output covering a 5 year period to compile figures 2.3, 2.5 and 2.6. In order to evaluate zonal winds U of the two model setups we use two different reanalysis products, NCEP (Kistler et al., 2001) and ERA-Interim (Dee et al., 2011).

For the evaluation of quantities of the convection scheme in chapter 2.2.3, we derive from observations two quantities: a maximum heating rate distribution and a cloud top distribution. First, the heating rates are derived from rain rates provided by Tropical Rainfall Measurement Mission (TRMM) using the algorithm (Ryu et al., 2011) that includes both convective and stratiform rain types. Second, cloud top heights are derived from global merged infrared satellite measurements of brightness temperature using the NCEP reanalysis to convert the brightness temperature into geometric height (Ortland et al., 2011). Note that the two employed observational quantities are not measured directly but are rather products derived from observations. Therefore, retrieval errors in the original observations and simplified assumptions in the derivation of the final product introduce additional uncertainty. In order to compare cloud observations with model data in a consistent way, we use temporally instantaneous data every 3 hours covering the year 2007, we remove non-cloudy data points and average observations spatially on $2^\circ \times 2^\circ$ resolution before performing the analysis.

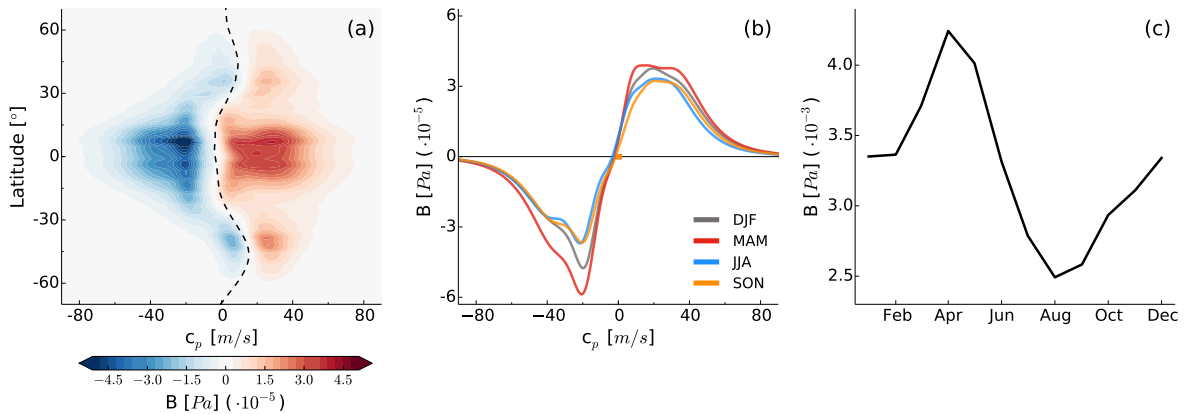


Figure 2.2: Source spectrum B of zonal momentum flux and its seasonal variability. (a) Latitudinal distribution of time and zonal mean source momentum flux as a function of phase speed. The dashed black line shows the zonal mean wind at 700hPa, the basis for the Doppler shift of the spectrum. (b) Zonal and meridional (5°N to 5°S lat) mean source spectra of zonal momentum flux in the four seasons. (c) Annual cycle of total zonal momentum flux B , zonal and meridional (5°N to 5°S lat) mean integrated over phase speed. All time averages cover 30 years (a-c).

2.2 A variable source spectrum of gravity wave momentum flux

In this chapter we highlight the fundamental aspects that are introduced by a convection based parameterization for gravity waves. First, we examine the temporal and spatial distribution of excited momentum flux, concentrating on the overall amount of momentum flux by integrating the source spectrum. In a second step, we look in more detail at the spectral characteristics of the source spectrum and provide the link between resolved input quantities, such as background wind and convective properties, and source spectrum properties, like its shape and its asymmetry. Having identified the decisive properties of the input quantities, we evaluate the quantities produced by the model with observational datasets.

As described in chapter 2.1.2, waves are launched along the direction of u_{700} which results in a meridional and zonal component in wave forcing and acceleration. Because the orientation of u_{700} is oriented dominantly in the zonal direction, the source spectrum in the meridional direction only reaches approximately 30% of the wave amplitude in zonal direction (not shown). Because we additionally focus on the zonally oriented winds of the QBO, we restrict the following analysis to zonal components even though waves are also launched in the meridional direction.

2.2.1 Spatial distribution and seasonality of momentum flux

The gravity wave source spectrum of momentum fluxes from the Beres scheme shows temporal and spatial variability due to the parameterization's coupling to resolved quantities. Largest source momentum fluxes occur in tropical regions, $|\Phi| < 20^\circ$,

where convection is most active throughout the year, see figure 2.2(a). However the parameterization also initiates waves in the midlatitudinal regions of the storm tracks, which are more active in the southern hemisphere. Since cloud heating depths are bigger in the tropics than in the midlatitudes, the wave spectrum peaks at and extends to higher phase speeds in the tropics compared to the midlatitudes. The phase speed spectrum is Doppler shifted with respect to the 700hPa zonal wind which is particularly important at the midlatitudes where a nonzero background wind prevails. In the tropics however, mean background winds are small which leads to a source spectrum with peak momentum fluxes at about $+20m/s$ and $-20m/s$ phase speed, see figure 2.2(b). The source spectrum compares well in latitudinal distribution with results from the WACCM model with the same gravity wave source parameterization (Beres et al., 2005; Richter et al., 2010). Besides differences in the convection parameterization between the two model version, the implementation of the Beres scheme in WACCM also includes a base limit for when the Doppler shift is applied: Only when the wind speed at 700 hPa is above 10 m/s, the phase speeds of the source spectrum are Doppler shifted. An inclusion of this base limit into our code would generate a source spectrum with momentum fluxes dominating at positive phase speeds (not shown). However we remove this, somewhat arbitrary, limit on the Doppler shift in our implementation of the code. Therefore, while positive phase speeds dominate the source spectrum in the WACCM model, ECHAM6-Beres shows more momentum flux at negative phase speeds than at positive phase speeds.

The source momentum flux shows a strong seasonal cycle, manifested in the mean seasonal spectra and the annual cycle of integrated source momentum flux, shown in figure 2.2 (b,c). The amount of momentum flux peaks in spring and shows a minimum in late summer, which quantitatively represents a reduction of approximately 40% from the peak in April to the minimum in August. The seasonality in source momentum flux is the basis for further analysis on the seasonality of the QBO in chapter 3.1.2.

It would be desirable to be able to identify a single physical input quantity which causes the seasonality in the amount of excited momentum flux B of figure 2.2(c). Even though the seasonality of the heating rate Q_0 is dominating the seasonality of B (not shown), we can't isolate a single, unique physical quantity which fully explains the seasonal cycle of B . Besides the seasonality in Q_0 , variability in tropospheric wind shear and other convective properties also contribute to the seasonal cycle in the amount of source momentum flux. In the following two sections however, we individually highlight the two most relevant physical input quantities, the background wind and the convective heating properties, which decisively control the characteristics of the source spectrum.

2.2.2 Effect of the background wind on the source spectrum

We show the effect of the background wind on the source spectrum for two selected regions, centered over the Indonesian archipelago and over South America. The source spectra in these two regions exhibit strong asymmetries, favouring momentum fluxes with positive phase speeds over Indonesia and momentum fluxes with negative phase speeds over South America, see figure 2.3(a,c). The asymmetries are dominated by deep

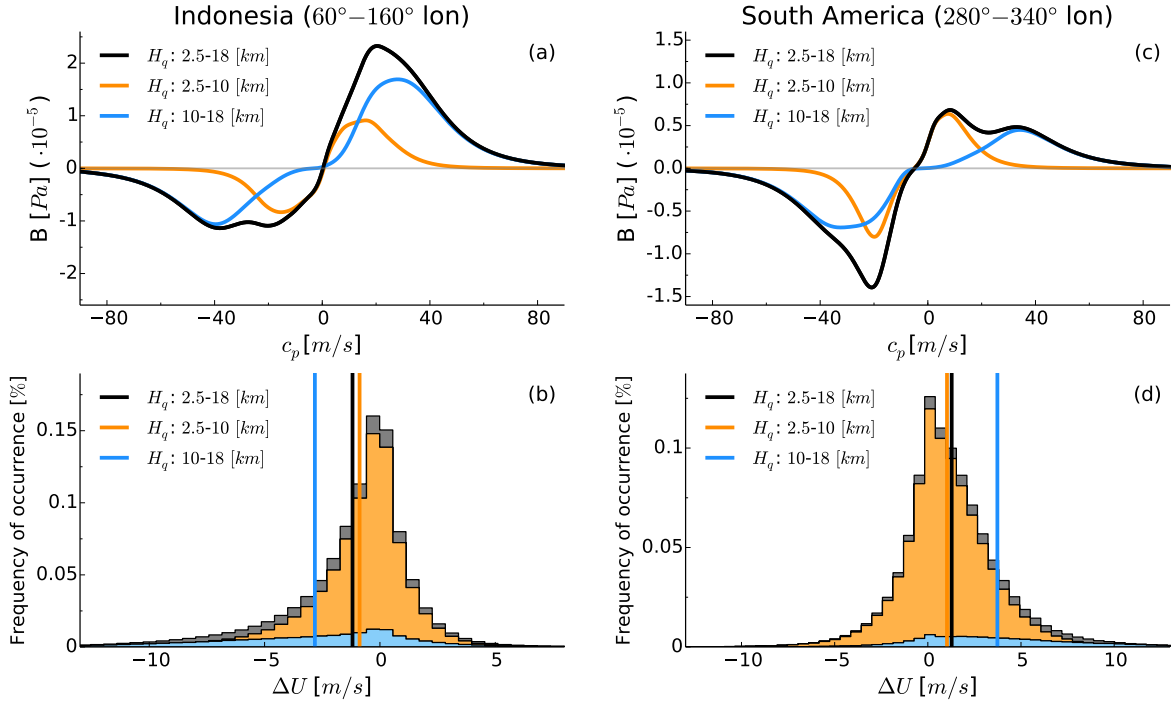


Figure 2.3: Effect of the background wind on the source spectrum, shown for two selected regions, centered over Indonesia (60° - 160° lon) (a,b) and over South America (280° - 340° lon) (c,d). Colors illustrate different regimes of heating depth: contribution from shallow heating depths (2.5 - 10 km, orange) and from deep heating depths (10 - 18 km, blue) to the entire range (2.5 - 18 km, black). Zonal, meridional (5° N to 5° S lat) and time (5 years) mean source spectra of zonal momentum flux (a,c). The spectral asymmetry is caused by wind shear, approximated as the mean wind relative to the zonal wind at 700 hPa ΔU , within the vertical extent of the heating. The histogram of ΔU is shown for different regimes of cloud heating depths (b,d) while the vertical lines denote the distribution mean.

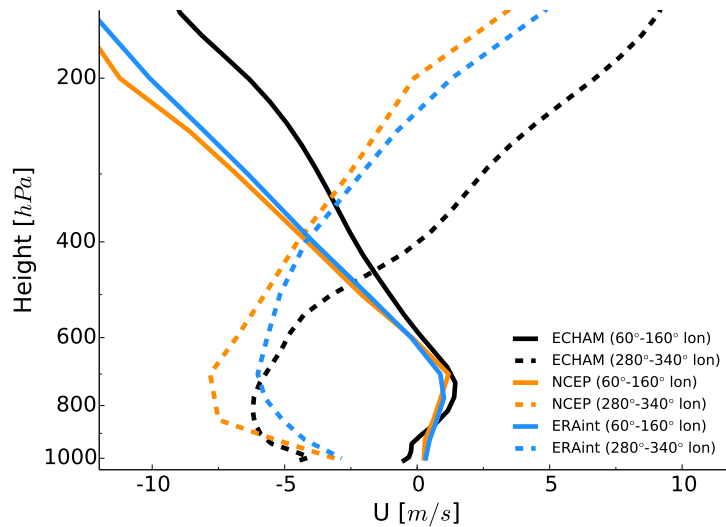


Figure 2.4: Zonal, meridional (5°N to 5°S lat) and time mean vertical wind profile for two regions, covering the eastern Indian ocean and Indonesia ($60^{\circ} - 160^{\circ}$ lon, solid) and South America ($280^{\circ} - 340^{\circ}$ lon, dashed). Comparison of ECHAM6-Beres simulation (black) with two reanalysis products: NCEP (orange) and ERA-Interim (blue). ECHAM6-Beres covers 30 years, NCEP 62 years and ERA-Interim 20 years.

convective clouds, depicted by the blue curve, whereas the contribution of the more shallow clouds is almost symmetric, depicted by the orange curve in figure 2.3(a,c).

As outlined in chapter 2.1, a positive wind shear produces a source spectrum with dominating negative phase speeds and vice versa. This result from a case study with a cloud resolving model (Beres et al., 2002) and localized observations (Pfister et al., 1993) is now extended to large geographical regions using model calculations of gravity waves generated with linear theory (Beres et al., 2004). The histogram of wind shear $\langle \frac{\partial U}{\partial z} \rangle$ in figure 2.3(b,d) shows a clear non-zero mean value, especially for the regime of deep convective clouds which cause the spectral asymmetry. While a negative wind shear leads to a source spectrum with dominant positive phase speeds over Indonesia, a positive wind shear can be associated with a source spectrum with dominant negative phase speeds over South America.

The modeled wind shear over the two selected regions agrees with reanalysis data, see figure 2.4. Although ECHAM shows a westerly bias in the upper troposphere in both regions, the vertical wind shear in the model is qualitatively consistent with reanalysis. In the free atmosphere, the region centered over the Indonesian archipelago shows a negative wind shear and the region over South America a positive wind shear. To summarize, different background winds, which qualitatively agree with reanalysis products, cause significant asymmetries in the gravity wave source spectrum in large geographical regions.

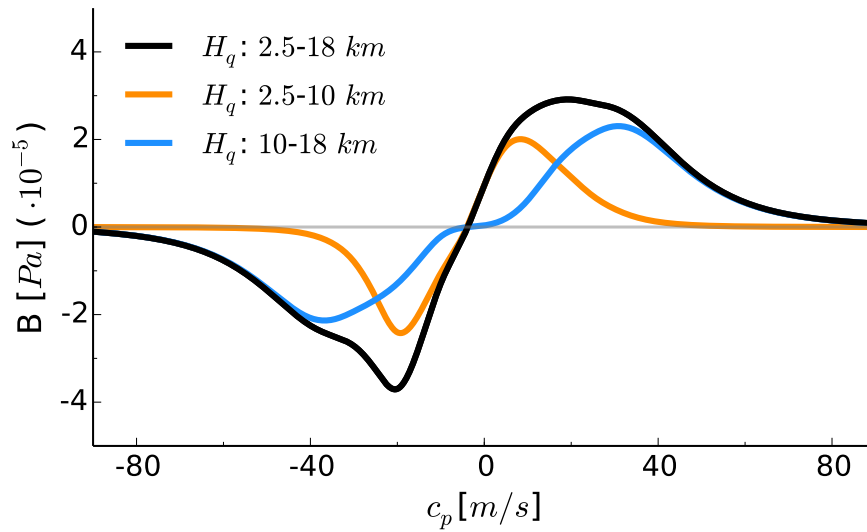


Figure 2.5: Separation of source spectrum into regimes of heating depth H_q . Zonal, meridional (5°N to 5°S lat) and time (5 years) mean source spectrum B for all cloud heating depths (black), shallow cloud heating depths (orange) and deep cloud heating depths (blue).

2.2.3 Effect of convective heating properties on the source spectrum

The source momentum fluxes show a strong dependence on properties of the convection scheme. The most important quantities are the heating depth and the maximum heating rate within a GCM grid box, with a particular importance on the histogram of heating depth and the heating rate's dependence on heating depth. The emitted source momentum flux is separated into the two regimes of shallow (orange) and deep (blue) convective clouds, see figure 2.5, illustrated by the peak at higher phasespeeds for deep convective clouds. The total spectrum (black) results from a superposition of both heating depth regimes. The separation into two heating depth regimes can be observed in more detail in figure 2.6(a) which shows the amount of excited momentum flux B as a function of heating depth. Shallow clouds with 2.5 km and 5 km heating depth and deep convective clouds with around 15 km heating depth contribute significantly to the entire source spectrum. Convective clouds with heating depths in the range 6 – 12 km however produce very little momentum flux.

The momentum flux histogram in figure 2.6(a) corresponds only partly to the heating depth histogram in figure 2.6(b), which shows that the convection scheme produces most frequently rather shallow clouds ($< 6\text{km}$), very few midlevel clouds ($6 - 12\text{km}$) and some deep convective clouds ($> 12\text{km}$). The two histograms do not agree because the amplitude of the source spectrum is additionally scaled by a factor $\propto Q_{max}^2$ which strongly increases with increasing heating depth, see 2.6(c). This nonlinear amplification of the source spectra's amplitudes leads to a peak in B at large heating depth, even though convection with large heating depth does not occur very frequently.

A comparison with TRMM and satellite based observations reveals deficiencies in the convection scheme, most apparent in the histogram of heating depth, see figure 2.6(b). Observations show a continuous distribution with dominating midlevel convec-

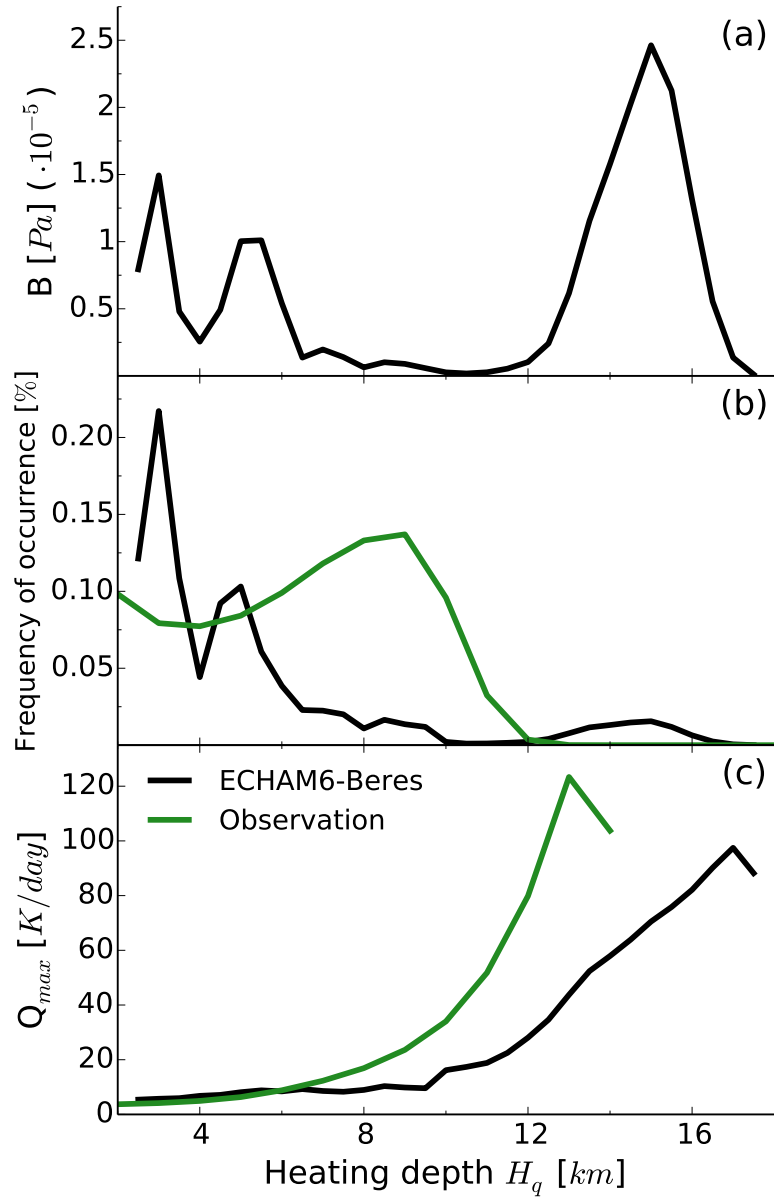


Figure 2.6: Influence of convection properties on the source momentum flux B (a) as a function of heating depth. Heating depth distribution (b) and maximum heating rate within a GCM grid box (c) (black) are compared to estimated observations (green) derived from geostationary infrared satellite data and TRMM.

tion which peaks at 9 km and ends at 12km heating depth rather than the double peak distribution that the convection scheme produces. Most obvious discrepancy appears in the range of 6 – 12km heating depth, where the model lacks convection, and at large heating depths, where the model produces convection in contrast to the observations. For a more detailed discussion and consequences due to the difference in observations and model data see chapter 3.2. The model’s distribution of heating rate Q_{max} however compares qualitatively to the observations, see figure 2.6(c), with a strong increase in Q_{max} with increasing heating depth. The kinks at the upper end of the distributions should not be over-interpreted because these are prone to sampling errors due to the very small number of events at the upper end of the heating depth distribution.

2.3 Summary

We couple the convection based source parameterization of gravity waves after Beres et al. (2004) to the propagation parameterization after Alexander and Dunkerton (1999) and implement the schemes into the atmospheric general circulation model ECHAM6. Compared to a gravity wave source parameterization with constant, prescribed sources, the Beres parameterization improves the representation of gravity waves in two main aspects.

First, the excited gravity waves show a strong spatial, figure 2.2(a), and temporal, figure 2.2(b,c), variability in the amount of total momentum flux. This variability is directly linked to the occurrence of areas of intense convection. Second, the shape of the source spectrum is not prescribed but coupled to heating characteristics of the convection scheme and the background wind. In detail, regionally different background winds over South America and the Indonesian archipelago result in different shapes of the source spectra, with dominating easterly and westerly waves, respectively (figure 2.3). The analysis further reveals that the regime of deep convective clouds causes in large part the spectral asymmetry, because vertical wind shears more effectively affect deep clouds than shallow clouds. Studies (Pfister et al., 1993) on localized geographical regions have shown that wind shear causes asymmetries in the waves’ source spectrum. Our model results show that this effect remains also important when averaging over large geographical domains covering > 10.000 km (order of 100° longitude at the equator).

Chapter 3

A convection based gravity wave parameterization improves the QBO simulated in a general circulation model

We first present the QBO simulated with a convection based gravity wave parameterization as the only source of gravity waves in the tropics. We compare the QBO with reanalysis data and with the QBO simulated with the previously employed gravity wave parameterization with fixed gravity wave sources after Hines. Performing an EOF analysis on the timeseries of QBO winds, we can link the downward propagation speed of the QBO to the amount of zonal wind tendencies. The statistical analysis also allows to evaluate the seasonality in QBO downward propagation speed and to assess the benefits of a physically based gravity wave source parameterization. We close this chapter discussing and identifying the most sensitive tuning parameters of the convection based gravity wave parameterization setup.

Experimental setup

Using the model setup as described in 2.1.1, we explore the effects of the Beres scheme, coupled to AD99, (ECHAM6-Beres) in comparison with a control run which includes a gravity wave parameterization with constant gravity wave sources (ECHAM6-Hines). For both experimental setups we perform a 30 year atmospheric simulation with prescribed climatological sea surface temperatures (SST) and sea ice concentrations (SIC), compiled from observed SSTs and SICs. We use monthly mean values of 30 years as standard temporal resolution for the shown plots, with ERA-Interim as a reference (Dee et al., 2011). For the EOF analysis in chapter 3.1.2, we use monthly mean zonal winds based on radiosonde observations at three equatorial stations and compiled at Freie Universität Berlin (FUB) (<http://www.geo.fu-berlin.de/en/met/ag/strat/produkte/qbo/>).

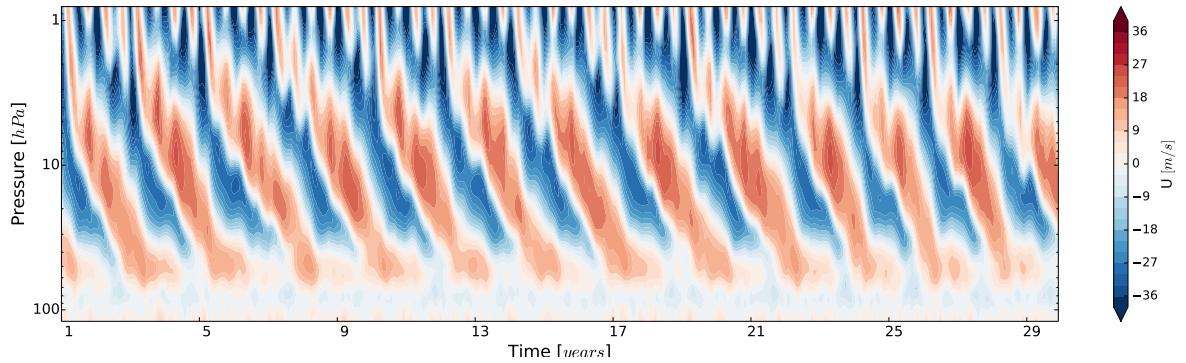


Figure 3.1: The QBO in ECHAM6-Beres. Timeseries of meridional (5°N to 5°S lat) and zonal mean zonal wind from a 30year model run with a purely convection based gravity wave source parameterization.

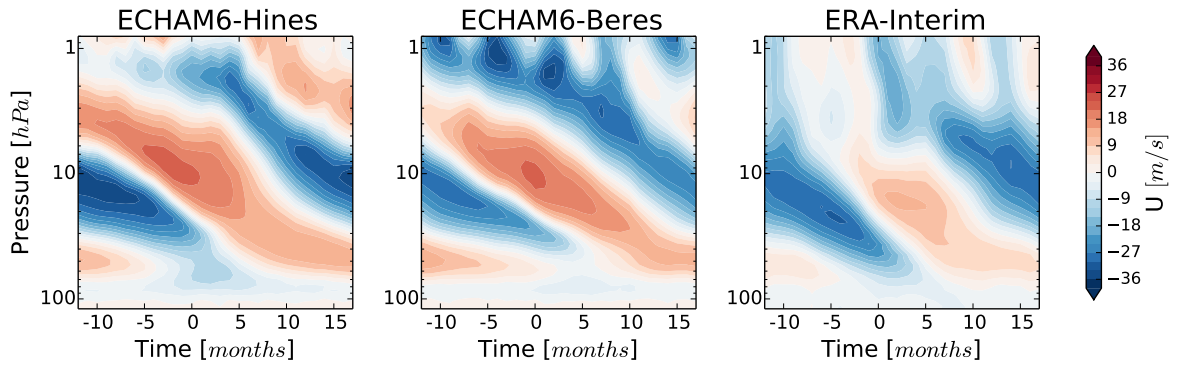


Figure 3.2: QBO composites of meridional (5°N to 5°S lat) and zonal mean zonal wind. Criterion for the composite is the onset of the westerly jet at 20 hPa . Comparison of the gravity wave parameterization with constant sources (ECHAM6-Hines) with the convection based gravity wave parameterization (ECHAM6-Beres) and reanalysis (ERA-Interim).

3.1 The QBO

ECHAM6-Beres produces a QBO with realistic features, see figure 3.1. The simulated evolution of zonal winds shows prominent features of the QBO: A periodic alternation of westerly and easterly winds, an asymmetry in amplitude with easterly jets being stronger than westerly jets, and a mean period of ~ 27.5 months. The simulated period is tuned with the parameters C_F and L , see chapter 2.1 for a more detailed parameter description and chapter 3.2 for a more thorough discussion on parameter tuning.

3.1.1 Comparison with ECHAM6-Hines and ERA-Interim

A comparison with the QBO of ECHAM6-Hines and of ERA-Interim shows improvements and deficiencies of the QBO simulated with ECHAM6-Beres. Both ECHAM6-Hines and ECHAM6-Beres produce a QBO with too strong westerly jet maxima, figure 3.2. However this bias is somewhat reduced in ECHAM6-Beres. The bias in the easterly jet maxima of ECHAM6-Hines is reduced such that the easterly wind speed maximum

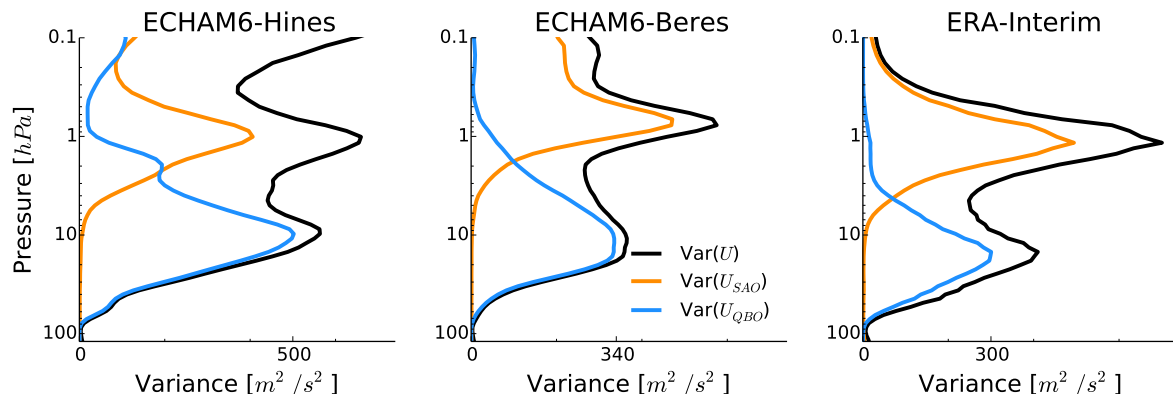


Figure 3.3: Variance over time (30 years) of meridional (5°N to 5°S lat) and zonal mean zonal wind. In order to compute the variance of the Semi-annual Oscillation $\text{Var}(U_{SAO})$ in orange and $\text{Var}(U_{QBO})$ in blue, a Fourier transform in time is applied to the winds, the periods between 5 and 7 months (SAO) and between 23 and 35 months (QBO) are selected to calculate each variance contribution. The variance over all periods $\text{Var}(U)$ is depicted in black. Comparison of the gravity wave parameterization with constant sources (ECHAM6-Hines) with the convection based gravity wave parameterization (ECHAM6-Beres) and reanalysis (ERA-Interim). The label on the x-axis shows the maximum value of $\text{Var}(U_{QBO})$.

in ECHAM6-Beres agrees with reanalysis. The easterly jet in ECHAM6-Beres does not extend as far downwards as in reanalysis data, but ends at 50 hPa rather than 90 hPa as in the reanalysis, which could partly be a result of the generally weaker easterly jet in ECHAM6-Beres. The westerly jet extends towards $\sim 75 \text{ hPa}$ in both model simulations and agrees well with ERA-Interim. In both model simulations, the QBO extends too far into the upper stratosphere above 10 hPa , with an improvement in ECHAM6-Beres. However this improvement comes at the cost of pronounced easterlies at about 1 hPa in ECHAM6-Beres.

The zonal wind variances in ECHAM6-Beres agree well with reanalysis, see figure 3.3. The wind variance in QBO-related periods agrees not only in amplitude but also in the position of the peak, a clear improvement over ECHAM6-Hines. The wind variance at 1 hPa in ECHAM6-Beres agrees reasonably well with ERA-Interim. At higher altitudes around 0.1 hPa , ECHAM6-Beres simulates the decrease in wind variance more realistically than ECHAM6-Hines, but shows higher values than the reanalysis.

The improvement in QBO wind variance in ECHAM6-Beres can partly be explained by different zonal wind tendency profiles in ECHAM6-Beres and ECHAM6-Hines. Figure 3.4 compares tendency profiles from simulations performed over one month and initiated with the same background state. The short temporal coverage guarantees that both parameterizations react to a nearly identical background wind profile. Following Scaife et al. (2000), lowering the waves' breaking levels reduces primarily the QBO amplitude. The comparison between both parameterizations shows that the peaks in the tendency profile in ECHAM6-Beres are situated at lower altitude than in ECHAM6-Hines, thus leading to a reduced QBO amplitude and QBO wind variance.

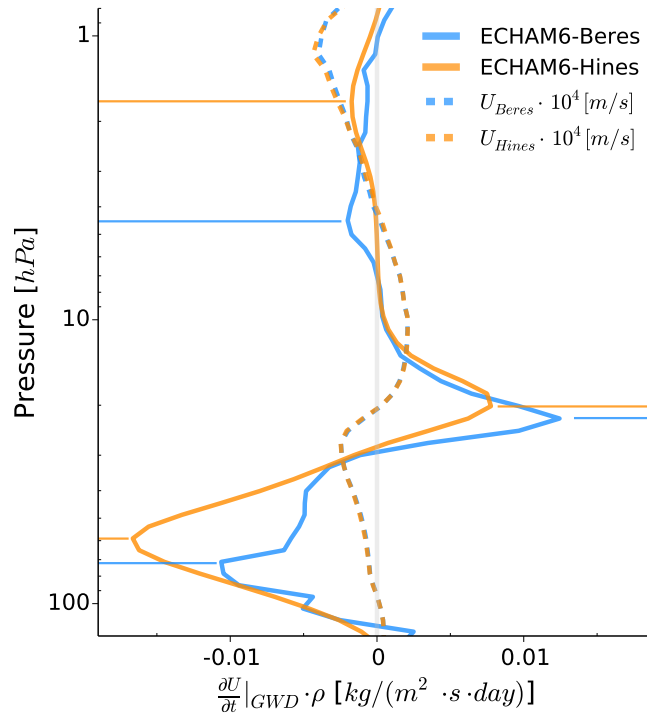


Figure 3.4: Comparison of zonal wind tendency ($\frac{\partial U}{\partial t}|_{GW}$) profiles due to gravity waves in ECHAM6-Beres (orange) with ECHAM6-Hines (blue), tendencies are scaled by density. Maxima in the tendency profiles are highlighted by horizontal lines in according colors, wind profiles are dashed. Zonal and meridional (5°N to 5°S lat) mean over one month.

3.1.2 Seasonal effects of parameterized, variable gravity wave sources on the QBO

Due to the physically based gravity wave sources, figure 2.2(c) shows a strong seasonal cycle in the amount of wave momentum flux emanating from the troposphere. We establish a link between the seasonality of gravity wave source strength, the seasonality in the amount of acceleration in the lower stratosphere, and finally the seasonality of QBO phase progression rate. Following the analysis by Wallace et al. (1993), who apply an EOF analysis on the zonal winds, we further extend the concept in order to show the seasonality of individual tendency components and of the total tendency.

Construction of an EOF analysis

We apply an EOF analysis on a monthly (t) based timeseries of meridionally averaged (5°N to 5°S lat) zonal mean anomalies of a variable $\chi'(z, t)$, computed on each vertical level z between 10 and 70 hPa . The analyzed quantities χ' are zonal wind U , total tendency of the zonal wind $\frac{\partial U}{\partial t}|_{GW+\nabla \cdot EP+ADV}$ and the individual tendency components due to gravity waves $\frac{\partial U}{\partial t}|_{GW}$, due to the divergence of the Eliassen-Palm flux of resolved waves, $\frac{\partial U}{\partial t}|_{\nabla \cdot EP}$, and due to horizontal and vertical advection $\frac{\partial U}{\partial t}|_{ADV}$. All data is smoothed by a simple 3-months running average, but in contrast to Wallace et al. (1993) and Taguchi (2010) not deseasonalized. Each quantity χ' can be expressed as a linear combination of empirical orthogonal functions EOF , which are dependent on height

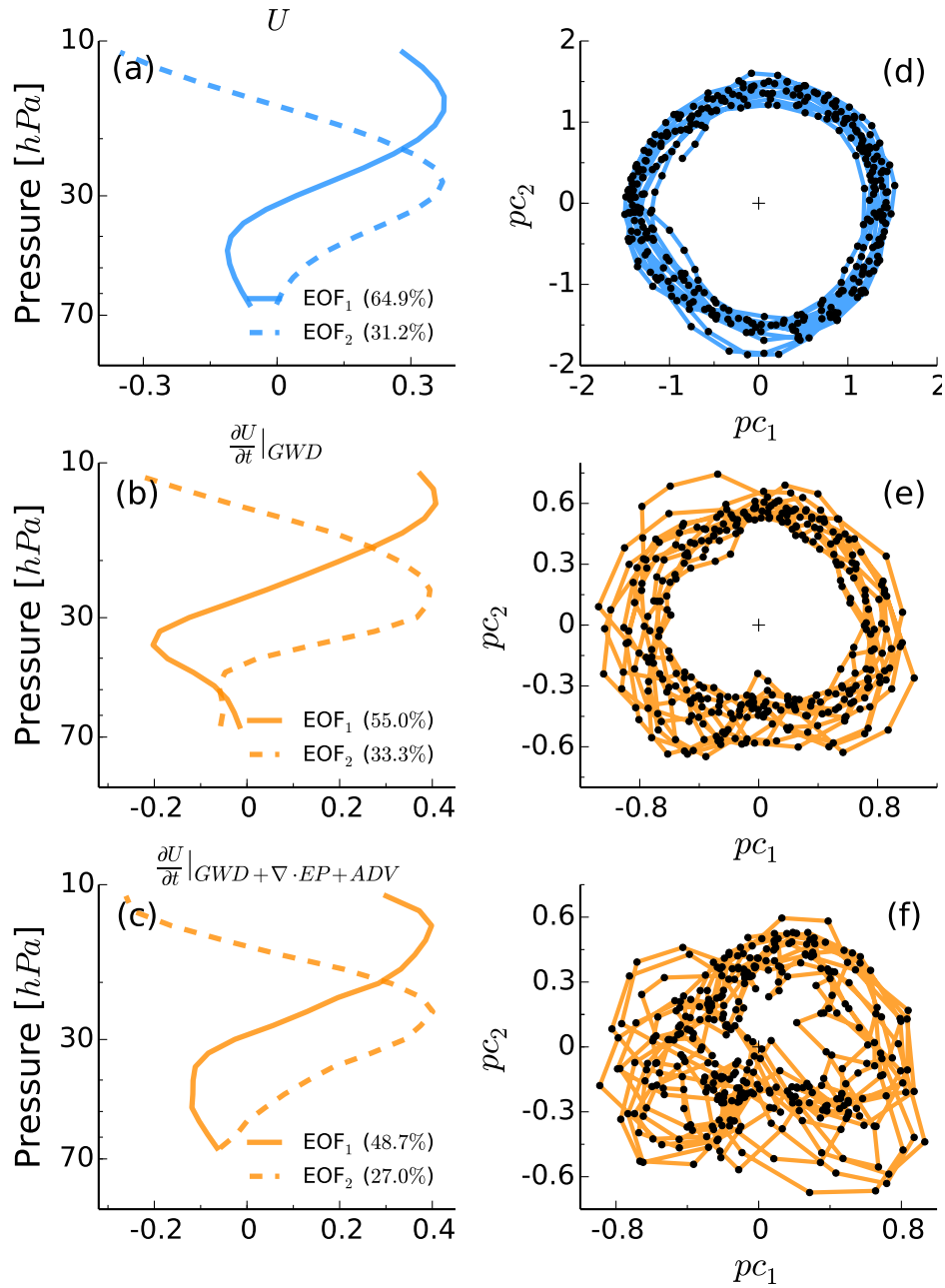


Figure 3.5: Empirical orthogonal functions (*EOF*) (a)-(c) and principal components (*pc*) (d)-(f) of zonal wind U (a,d), tendency of zonal wind due to gravity waves $\frac{\partial U}{\partial t}|_{GW}$ (b,e) and the total tendency of all components $\frac{\partial U}{\partial t}|_{GW+\nabla \cdot EP+ADV}$ (c,f). The numbers in the legend (a)-(c) indicate the fraction of variance that each EOF accounts for. The *pcs* in (d) are scaled to unit variance, units on individual plots are arbitrary. The *EOFs* and *pcs* of $\frac{\partial U}{\partial t}|_{\nabla \cdot EP}$ and $\frac{\partial U}{\partial t}|_{ADV}$ are not shown individually; they are qualitatively similar to $\frac{\partial U}{\partial t}|_{GWC}$ in (b,e).

but constant in time, and principal components pc which represent the corresponding timeseries:

$$\chi'(z, t) \simeq EOF_1(z) \cdot pc_1(t) + EOF_2(z) \cdot pc_2(t) \quad (3.1)$$

omitting higher orders because the first two EOF s cover most of the variance; in the case of U , the two leading EOF s account for 96.1% of the total variance, see figure 3.5(a). The EOF s of the tendency components due to gravity wave and the tendency of all components are shown in figure 3.5(b) and (c).

Due to the high amount of covered variance by the two leading EOF s, the 2D phase space of the pcs serves as a good proxy for the temporal evolution of the QBO, displayed in 3.5(d-f). Each point $\psi(t)$ in phase space corresponds to a state of the QBO in a certain month, while in the course of a full QBO cycle, the points form a circle in phase space. Given the circular characteristics of the temporal evolution in phase space, the data points ψ can be represented by polar coordinates with the radial component $|\psi|$

$$|\psi(t)| = \sqrt{pc_1(t)^2 + pc_2(t)^2} \quad (3.2)$$

and angular component ϕ

$$\phi(t) = \text{atan2}(pc_1(t), pc_2(t)) \quad (3.3)$$

with the function atan2 being based on the function arctan , but extended to return the appropriate quadrant of the computed angle. The function atan2 returns a value in $[0, 2\pi[$ which correspond to angles of the entire circle.

In the case of U , we estimate the progression rate of the QBO phase ϕ'_U in month t as the rate of change of the angle ϕ ,

$$\phi'_U(t) = \frac{1}{2 \cdot 2\pi} [\phi(t-1) + \phi(t+1)] \quad (3.4)$$

with the units *cycle/month*. In the cases when the EOF analysis was applied to the different tendency components, we use $|\psi(t)|$ as a proxy for the amount of the wind tendency in the particular month. For each month we calculate ϕ' from the phase space in U and $|\psi|$ for the individual tendency components and compile the data to show the seasonality of the computed quantities, displayed in figure 3.6.

Results on the seasonal timescale

The seasonality of QBO phase progression and the seasonality of the total tendency are in good agreement, peaking in May and showing a second local maximum in October/November, shown for both ECHAM6-Beres in figure 3.6 (a) and ECHAM6-Hines in figure 3.6 (c). This objective statistical analysis confirms the physical understanding that the QBO descends faster in times when more acceleration is exerted. Focusing on the individual tendency components in figure 3.6 (b) and (d), we see that each component exhibits different characteristics in seasonality. While $\frac{\partial U}{\partial t}|_{\nabla \cdot EP}$ shows a semiannual oscillatory behavior with peaks in March and October, $\frac{\partial U}{\partial t}|_{ADV}$ has a minimum in late spring and maximum in late summer which opposes the maxima and minima of the

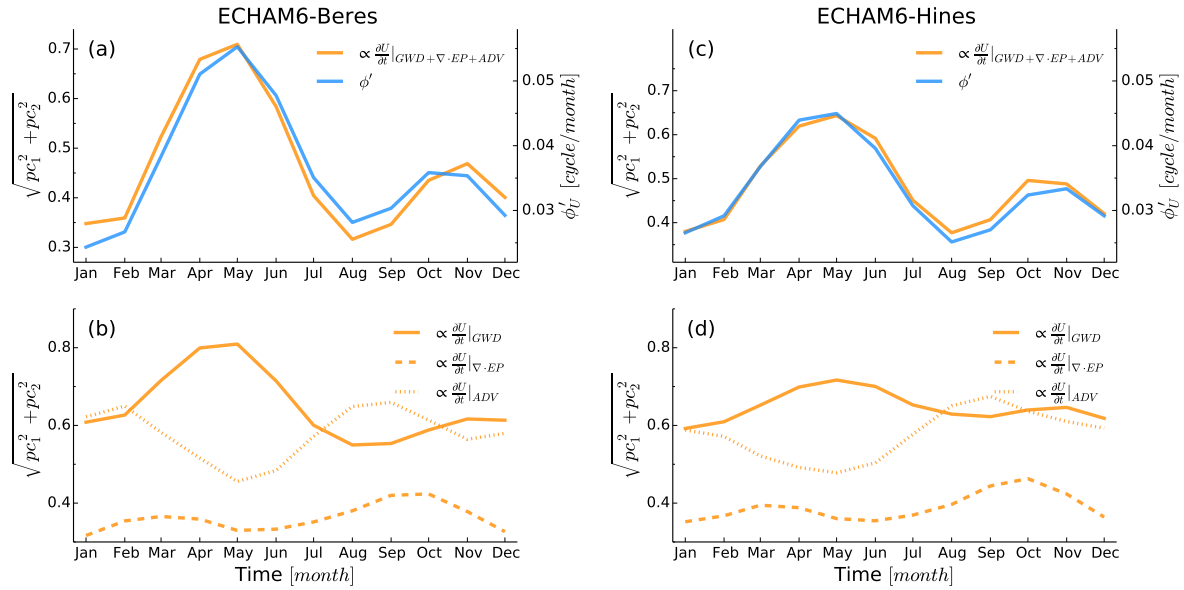


Figure 3.6: Seasonal cycle of progression of QBO phases (blue) and seasonal cycle of amount of zonal wind tendency (orange) for the Beres (a,b) and the Hines scheme (c,d). Comparison of qbo phase progression (blue) with amount of all tendency components (orange) for the Beres (a) and the Hines (c) scheme. Comparison of the individual tendency components of the entire tendency budget for the Beres (b) and the Hines (d) scheme. The drawn tendency is proportional to the actual tendency values, units are arbitrary. Note the two different y-axis in (a,c).

entire tendency of figure 3.6 (a,c). Both $\frac{\partial U}{\partial t}|_{ADV}$ and $\frac{\partial U}{\partial t}|_{\nabla \cdot EP}$ show a qualitatively similar behaviour in both model versions. The seasonality of the tendency due to gravity wave however differs for the different gravity wave parameterizations. While both $\frac{\partial U}{\partial t}|_{GW}$ in ECHAM6-Hines and $\frac{\partial U}{\partial t}|_{GW}$ in ECHAM6-Beres show an annual variation with maximum in April/May and minimum in August/September, the seasonality in ECHAM6-Beres is more pronounced which is manifested in the stronger amplitude of the seasonal variation of $\frac{\partial U}{\partial t}|_{GW}$.

Note that the entire acceleration in the upper panel of figure 3.6 is not attained by simply adding the three tendency components in the lower panel. Each curve is the result of an individual EOF analysis and in the case of the total tendency, the individual tendency components are added before the EOF analysis is performed.

In figure 3.7, the comparison of the two model configurations with observations suggests an improvement due to the variable gravity wave scheme in ECHAM6-Beres. Both model versions show qualitatively a consistent agreement with observations, which is caused by the similar seasonality of $\frac{\partial U}{\partial t}|_{ADV}$. However adding the seasonal cycle of $\frac{\partial U}{\partial t}|_{GW}$ in the case of ECHAM6-Beres leads to better agreement with the observed seasonality. Note that the mean phase progression in both ECHAM6-Hines and ECHAM6-Beres lie within the 2σ ranges of the reanalysis product and that the shown improvement in QBO phase progression rate in ECHAM6-Beres is statistically not significant.

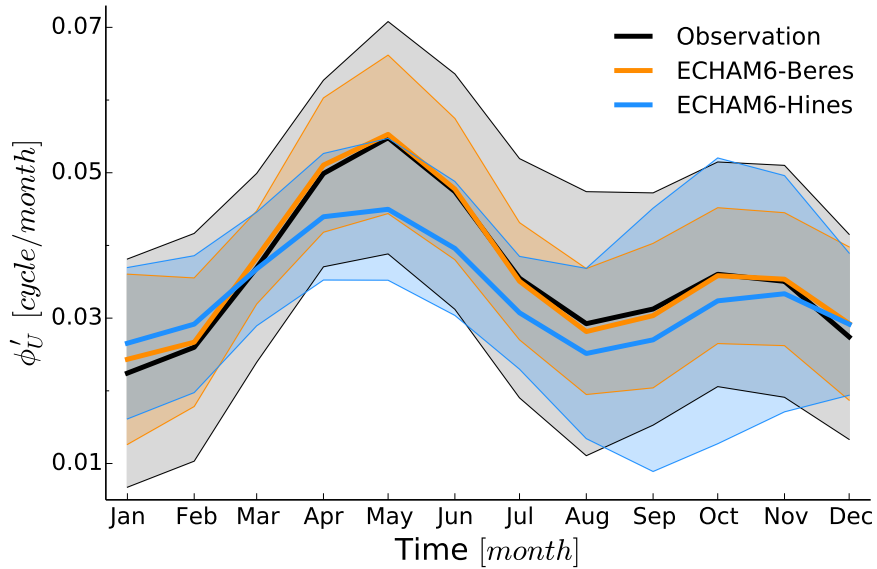


Figure 3.7: Sesaonal cycle of progression of qbo phases ϕ' . The comparison with radiosonde observations from FU Berlin (black) shows an improvement of the convection based gravity wave parameterization in ECHAM6-Beres (orange) over ECHAM6-Hines with a gravity wave parameterization with constant sources (blue). Shaded areas show the $2\text{-}\sigma$ range.

3.2 Discussion and implications for tuning the gravity wave schemes

Most parameterizations include parameters, whose values are only loosely determined by theoretical arguments or observational studies but which substantially impact the output of the parameterization. Changing the value of these parameters within the theoretical and observational limits, in order to generate a more realistic representation of the parameterized processes or affected phenomena, remains a necessary step while implementing a parameterization into a model. Here we refer to this process as 'tuning' and to the adjustable parameters as 'tuning parameters'. In this study, we tune the gravity wave source and gravity wave propagation parameterization in order to obtain a QBO; we specifically choose the QBO period as the most important target criterion. In this chapter we focus on two aspects of the source spectrum, the spectral shape and the amplitude, and we evaluate potentials for tuning each of the two aspects in the context of the Beres + AD99 setup.

3.2.1 Spectral characteristics of the source momentum fluxes: Tuning the propagation scheme

The comparison of convection properties of ECHAM6-Beres with observational products reveals discrepancies which affect the source spectrum's shape. The overrepresentation of deep convective clouds in ECHAM6, figure 2.6(b), results in large source momentum fluxes at large heating depths, see the peak at 15 km in figure 2.6(a). This bias at deep convective events leads to an overrepresentation of source momentum

fluxes at high phase speeds (figure 2.5). Additionally, the design of the Beres scheme already entails an underrepresentation of source momentum flux at low phase speeds: The parameterization does not include the waves generated by the obstacle effect, or “moving mountain mechanism” (Lane et al., 2001). These waves are similar to orographic gravity wave such that the waves are stationary with respect to the convective cell, thus producing momentum fluxes at low phase speeds. For a more detailed discussion on the difficulties of implementing the obstacle effect into gravity wave source parameterizations see Alexander et al. (2006). The combined effect of both aspects, the bias in the convection scheme and the missing obstacle effect, suggests an underrepresentation of small phase speed waves, $|c_p| < 15 \text{ m/s}$, and an overrepresentation of large phase speed waves, $|c_p| > 40 \text{ m/s}$, in the modeled source spectrum.

Results from other model studies and observations support the existence of a modeled overrepresentation of large phase speed waves and underrepresentation of small phase speed waves. Several case studies performed with cloud resolving models show source spectra which peak in the range between 5 and 20 m/s (Alexander and Holton, 1997; Piani and Durran, 2001; Alexander et al., 2006; Kuester et al., 2008). The observational study based on localized airborne measurements by Pfister et al. (1993) reveals source spectra peaking between 0 and 10 m/s , depending on the background wind. Jewtoukoff et al. (2013) analyze high frequency balloon measurements in the stratosphere which show gravity wave spectra peaking between 0 and 15 m/s , while corresponding numerical simulations show peaks at higher phase speeds. Even though one referenced spectrum peaks at 20 m/s , which is in accordance to the peak of the modeled source spectrum (figure 2.2), none of the referenced spectra shows such pronounced momentum fluxes at phase speeds bigger than 40 m/s .

The Beres scheme provides very limited possibilities for tuning the spectral shape because the spectral characteristics are dependent on the convective properties and the background wind, a fundamental concept of the parameterization. If these physical input values however exhibit a robust bias, only a rather brute-force manipulation of the spectral shape is possible, e.g. restricting momentum fluxes to phase speeds $< 50 \text{ m/s}$. Even though other studies and observations suggest that the modeled source spectrum shows deficiencies, we refrain from manually changing the source spectrum for two reasons: First, the high degree of unphysical subjectiveness that would be incorporated into the parameterization and second, the lack of sufficient comprehensive observations of global source spectra characteristics.

However, the indicated underrepresentation of momentum fluxes at low phase speeds is reflected in the values chosen for parameters ϵ and λ_h , relevant for tuning the propagation parameterization. A small value of ϵ and a large value for λ_h both decrease the levels where the waves become convectively unstable, the breaking level. When tuning the propagation parameterization, the values for ϵ and λ_h are chosen such that the peaks in the tendency profile correspond to the levels of the strongest wind shear. Given the underrepresentation of waves with low phase speeds, a high value for λ_h and a small value for ϵ are necessary that waves with large phase speeds break at much lower levels than their critical levels.

3.2.2 Amplitude of the source spectrum: Tuning for the QBO period

The range of total momentum flux excited in the tropics is well observed. Studies based on observations and cloud resolving models show mean momentum fluxes in the range $1 - 5 \text{ mPa}$ (Sato and Dunkerton, 1997; Piani et al., 2000; Grimsdell et al., 2010; Geller et al., 2013), while Dunkerton (1997) states that it requires time averaged, zonal mean flux of tropical gravity waves of approximately 1 mPa to drive the QBO. The observational data constrain the range of total excited momentum flux for justifiable limits on tuning parameters. The two parameters C_F and L , the fraction of convection within a GCM gridbox and the spatial averaging length, respectively, influence the overall amplitude of the source spectrum. The amplitude of the source spectrum affects the amount of exerted acceleration on the jets of the QBO and consequently strongly determines the QBO period, see also Scaife et al. (2000). Both tuning parameters equally change the amount of momentum flux at all phase speeds of the spectrum but have no effect on the spectral shape or the temporal and spatial variability. The gravity wave source parameterization produces, on an annual average, a mean momentum flux of approximately $3 - 3.5 \text{ mPa}$, see figure 2.2 (c). Given that the modeled amount of excited wave momentum flux compares well to observations and that with $C_F = 3.5\%$ and $L = 1000\text{km}$ the parameter values lie within a physical range, we can say that the tuning of the source parameterization obeys the limits of the observations. The tuned amplitude of the source spectrum generates a QBO period of ~ 27.5 months.

3.3 Summary

With a convection based gravity wave source parameterization as the only source of gravity waves, the atmospheric GCM ECHAM6 produces a realistic QBO, see figure 3.1. Compared to the previously employed gravity wave parameterization in ECHAM6, which prescribes spatially and temporally constant sources, the QBO simulated with ECHAM6-Beres shows, on one hand, a slight deterioration of the vertical extent of the easterly jet, shown in figure 3.2. On the other hand however, the wind speeds of the jet maxima and the variance of wind alteration show a clear improvement, see figure 3.3. More generally, we point out that deficiencies in QBO characteristics are not necessarily linked to shortcomings in gravity wave parameterizations. Possible deficiencies in the modeled resolved waves or the upwelling can deteriorate the representation of the QBO as well.

We apply an EOF analysis on the QBO zonal winds and on the individual zonal wind tendency components of the momentum budget of the QBO. The analysis shows that the seasonality of the tendency due to gravity waves dominates the seasonality of the downward propagation of the QBO jets. Note that $\frac{\partial U}{\partial t}|_{GWD}$ in figure 3.6(b) matches the seasonal variation in excited amount of momentum flux in 2.2(c). Due to a more realistic, seasonally varying excitation of parameterized wave fluxes from convection, the modeled QBO suggests an improvement in its jet downward propagation rate, see figure 3.7. We point out that the EOF analysis suffers several simplifications: first,

the EOF analysis produces only vertically integrated values of QBO related quantities, second the series of *EOFs* is truncated after the first two *EOFs*, and third using the length of the vector in phase space as a proxy for the amount of zonal wind tendency is a crude approximation. However, in contrast to the given shortcomings of the analysis, the strong agreement between the amount of tendency and the QBO phase progression in both model versions confirms the applicability of the chosen method, figure 3.6(a,c).

When tuning the parameterization it turns out that the amplitude of the source spectrum, which translates to the total amount of excited momentum flux, and the breaking levels of the propagation parameterization are important factors to produce a QBO in the chosen model setup. Within the range of physically justified limits, both the amplitude and the breaking levels require tuning. However the shape, the asymmetries, the temporal, and the spatial variability of the spectrum remain entirely based on physical values, provided by the model. We show that the physically based character of the source parameterization, coupled to the propagation parameterization of AD99, improves the modeled QBO.

Chapter 4

Influence of ENSO on the QBO: Results from an ensemble of idealized simulations

Having presented the improvements of physically based gravity wave sources on the seasonality of the QBO, we extend the time frame to interannual timescales. El Niño / Southern Oscillation (ENSO) and the QBO are both equatorial phenomena exhibiting variability on the interannual timescale. In this chapter we analyse to which extent anomalies in wave activity associated with ENSO modulate the QBO.

4.1 Experimental setup

Isolating the ENSO signal on the QBO in a long timeseries of data can include cumbersome statistics, because (I) individual ENSO events differ in strength and spatial extent; (II) Any other perturbation or internal variability of the climate system can also affect both the QBO and ENSO and disguise the full ENSO signal on the QBO; (III) The QBO and the ENSO phases vary independently of each other. Therefore, selecting specific ENSO events in a timeseries will give a variety of QBO phases, which does not allow for a systematic statistical analysis. We therefore use two ensembles, each with a different QBO phase, which react to pronounced SST perturbations due to each El Niño (EL) and La Niña (LA) conditions.

We use the model setup as described in chapter 2.1.1 which includes a physically based gravity wave parameterization for convective gravity wave sources. We perform atmosphere-only simulations with prescribed SST and SIC as boundary conditions, similar to AMIP Taylor et al. (2012). In order to achieve a clean and pronounced ENSO signal, we select the strongest El Niño and La Niña events of the past decades and construct a SST and SIC composite of the detrended observed SST and SIC time-series. The El Niño composite consists the years 1972/1973, 1982/1983, and 1997/1998 and the La Niña composite includes the years 1955/1956, 1973/1974, 1975/1976, and 1988/1989. We subjectively select the chosen ENSO events on the basis of several

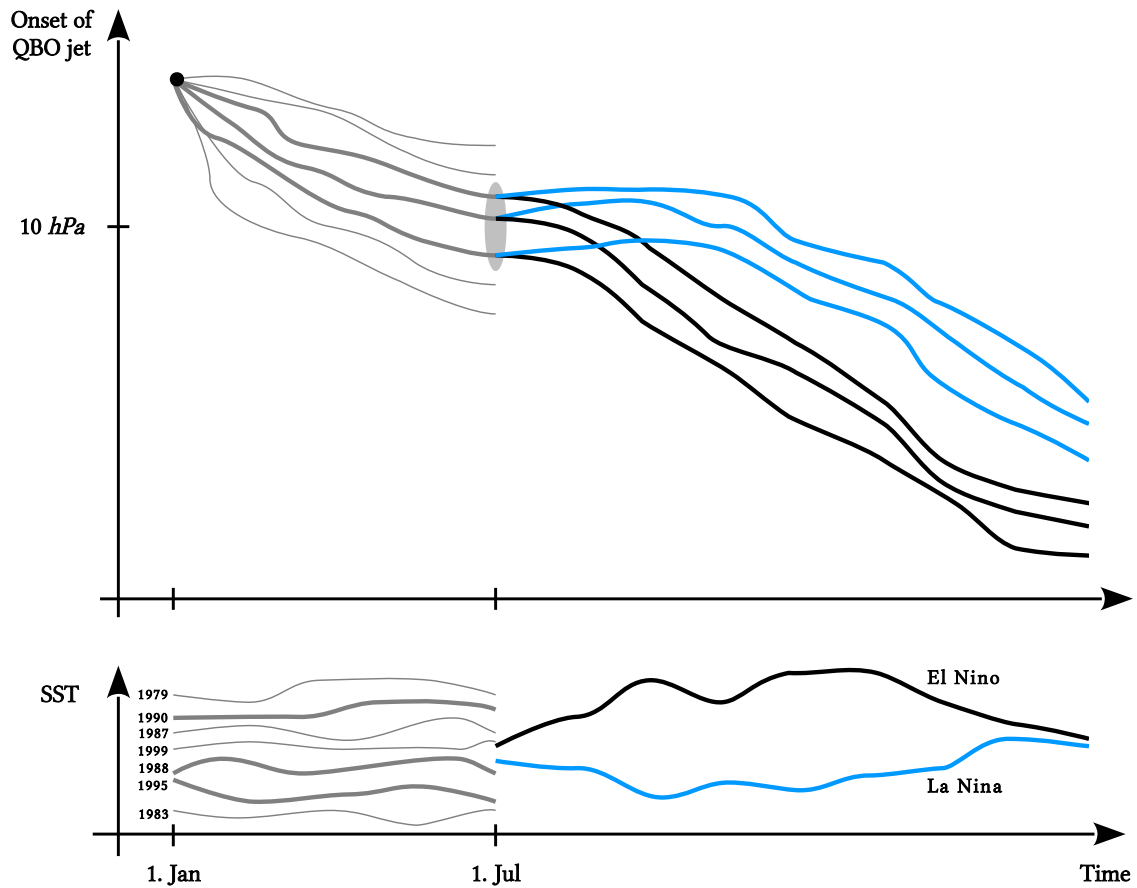


Figure 4.1: Illustration of the experimental setup. First part of the time axis until Jul 1st shows the generation of an ensemble with similar QBO characteristics (thick gray), the second part of the time axis after Jul 1st shows how the same ensemble reacts differently to El Niño (black) and La Niña (blue) conditions. The upper figure shows the position of the onset of the QBO jet, valid for both an easterly and a westerly jet, the lower figure illustrates the different SSTs to generate the ensemble and the different SSTs during El Niño and La Niña. The actual ensemble comprises 10 members, not three as illustrated in the figure and the actual number of model runs from which the ensemble is drawn is 30, not seven as illustrated in the figure.

	QBOW	QBOE
El Niño	# 10	# 10
La Niña	# 10	# 10

Table 4.1: Overview of number of ensemble members for the experimental setup with two initial QBO phases (QBOW and QBOE) and two different ENSO boundary conditions (El Niño and La Niña).

ENSO indices with the aim to gain a strong El Niño and La Niña signal from more than just a single event. The composites cover a period of 18 months, from July 1st of the first year until the end of the second year. Because the ENSO signal peaks in boreal winter, the chosen period covers a full cycle of an ENSO perturbation with near neutral ENSO conditions at the start and at the end of the period. We run the experiments with atmospheric boundary conditions and solar irradiance from the year 1988/89. Even though the ENSO signal is most pronounced in the Pacific, we compile the composite for global SSTs and SICs, including possible teleconnections in regions other than the central Pacific.

We generate two ensembles of each 10 members selected from a pool of each 30 simulations generated with different boundary conditions. The two ensembles constitute an easterly and a westerly QBO phase, which each respond to El Niño and La Niña boundary conditions starting from July 1st. In detail, we generate the ensembles with different QBO initial conditions as follows, illustrated also in figure 4.1. Starting from a single initial QBO profile on January 1st, the QBO evolves independently for each year between 1979 and 2008 for six months. The initially identical QBO evolves under different boundary conditions for the first six months of each year which leads to different QBO profiles on July 1st. From the pool of 30 QBO profiles on July 1st, we draw 10 profiles with similar QBO amplitude and similar positions of the onset of the jets. We repeat the process to create two ensembles, generated with different initial QBO profiles. In one case the initial QBO profile on July 1st exhibits a westerly QBO jet above 10 *hPa* and an easterly jet below 10 *hPa* (QBOW). In the second case the easterly jet is positioned above the westerly jet which prevails below 10 *hPa* (QBOE). For the detailed wind profiles of QBOW see the initial profile of figure 4.6 and for QBOE see figure 4.9. For all analysis and figures in this chapter except figure 4.5, we compute the meridional mean between -10° and $+10^\circ$ latitude.

Summarizing the experimental setup we run the four different types of simulations shown in table 4.1: Having generated two 10 member ensembles of a QBOW and a QBOE initial wind profile on July 1st, we run both ensembles for each El Niño and La Niña boundary conditions lasting 18 months. The chosen experimental setup aims at isolating the effect of the difference between El Niño and La Niña on the QBO. Considering the oscillatory character of the QBO, we analyze the ENSO effect on two QBO phases, QBOW and QBOE.

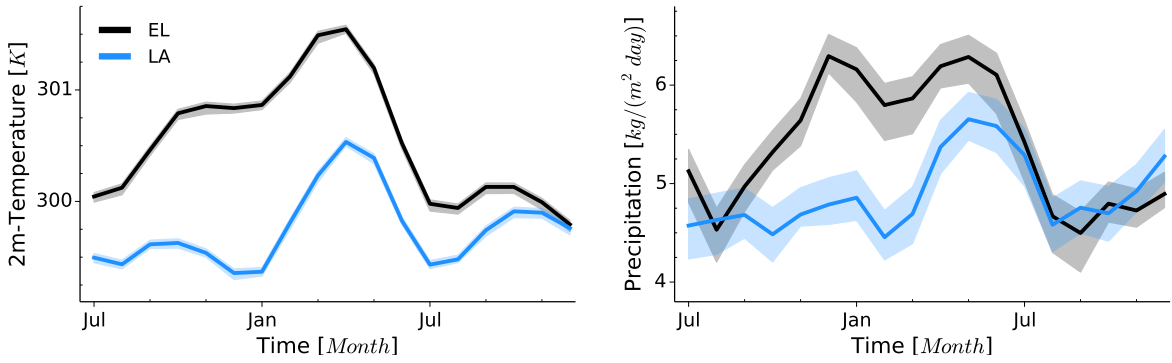


Figure 4.2: Timeseries of zonal and meridional mean temperature at 2 m (left) and precipitation (right) for El Niño (black) and La Niña (blue) conditions during QBOE phase. Temperature at 2 m and precipitation for QBOW phase (not shown) is qualitatively similar to QBOE phase. The shown precipitation is the total precipitation. Solid lines show the ensemble means and shading indicates the range of two standard deviations (2σ).

4.2 Changes in the background state

4.2.1 Surface temperature and precipitation

Before showing the forcing quantities relevant for the QBO, we show how ENSO modulates physical quantities in the troposphere. Although the ENSO signal peaks in the Pacific, we show the mean along the entire equator because the amount of waves in the entire tropics, and not the waves in any specific area, drive the QBO. Considering the entire tropics we furthermore include possible teleconnections related to ENSO. The temperature at 2 m closely follows the SSTs. During El Niño conditions, the temperature at 2 m is generally higher than during La Niña conditions, while the difference peaks with 1.5 K at December and January, see left panel in figure 4.2. Since we prescribe the SSTs for El Niño and La Niña conditions, the ensemble spread in the 2 m temperature is small, possibly related to variability in the large scale circulation over land.

The amount of precipitation is closely linked to the surface temperatures, see right panel in figure 4.2. The total precipitation during El Niño exceeds the precipitation during La Niña, with a mean increase of $\sim 25\%$ during El Niño compared to La Niña between October and March. Since the convective precipitation exceeds the large scale precipitation at the equator by a factor ~ 30 (not shown), the convective precipitation dominates the changes in total precipitation between El Niño and La Niña conditions. The increase in precipitation is closely linked to the amount of convective heating which in turn governs the amplitudes of the excited waves, see chapter 2.2.3 for gravity waves. We therefore expect the increase in precipitation during El Niño to project on the amount of excited waves, presented in the next chapter.

The model results agree with observation which also show an increase in precipitation rate with an increase in tropical SSTs. Regressing tropical precipitation rates from the microwave sounding unit (MSU) with SST anomalies in a 10 year timeseries, Soden (2000) find a regression coefficient of 0.77 mm/day/K . Using this regression coefficient,

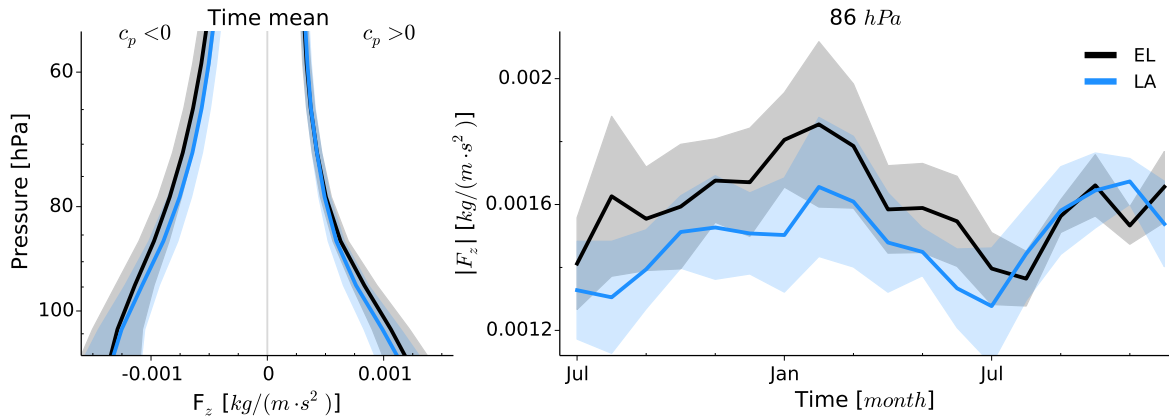


Figure 4.3: Vertical component F_z of the spectral EP-Flux vector for El Niño (black) and La Niña (blue) conditions during QBOW phase. Vertical EP-Flux vector F_z for QBOE phase (not shown) is qualitatively similar to QBOW phase. Zonal and meridional mean of F_z , scaled by density ρ , shows the integral over all frequencies and wave numbers. Solid lines show the ensemble means and shading indicates the range of two standard deviations (2σ). Left panel: Vertical profile of time mean F_z for easterly ($c < 0$) and westerly ($c > 0$) waves. Right panel: Timeseries of absolute $|F_z|$ at 86 hPa, with $|F_z| = |F_{z,c < 0}| + |F_{z,c > 0}|$.

a peak difference of $\sim 1.5 K$ between El Niño and La Niña conditions gives an increase in precipitation rate of $\sim 1.2 \text{ mm/day}$. This simple calculation agrees with the modeled peak increase in precipitation rate of $\sim 1.4 \text{ mm/day}$.

Note that other observational studies do not identify a relationship between ENSO and tropical global mean precipitation. Gu et al. (2007) analyze the timeseries of Global Precipitation Climatology Project (GPCP) and do not find an ENSO signal in the precipitation. However two of the three strongest El Niño events in this timeseries, according to the Nino 3.4 index, coincide with the volcanic eruptions El Chichón (1982/1983) and Pinatubo (1991/1992). Volcanic eruptions suppress precipitation and therefore oppose the suggested increase in tropical precipitation during El Niño events (Gu et al., 2007). The fact that volcanic eruptions dominate the variability in the observed timeseries of tropical precipitation in their analysis may explain why Gu et al. (2007) present different results than Soden (2000).

4.2.2 Wave activity and upwelling

The amount of the resolved waves increases during El Niño compared to La Niña. We use the vertical component F_z of the EP Flux vector as a proxy for resolved wave activity. Note that wave activity, and the wind tendency on the QBO, associated with the meridional component F_y is comparable to the vertical component F_z , but plotting F_y is not feasible for visualization. The amount of momentum carried by resolved waves decreases continuously as waves travel upwards and dissipate, see left panel in figure 4.3. During El Niño, the profiles of F_z increase for both easterly ($c_p < 0$) and westerly ($c_p > 0$) waves on a 18 months time mean. We omit extending the profile above 55 hPa because the different evolution of the QBO jets above will cause different wave filtering and hence differences in the profiles unrelated to the source. The timeseries of

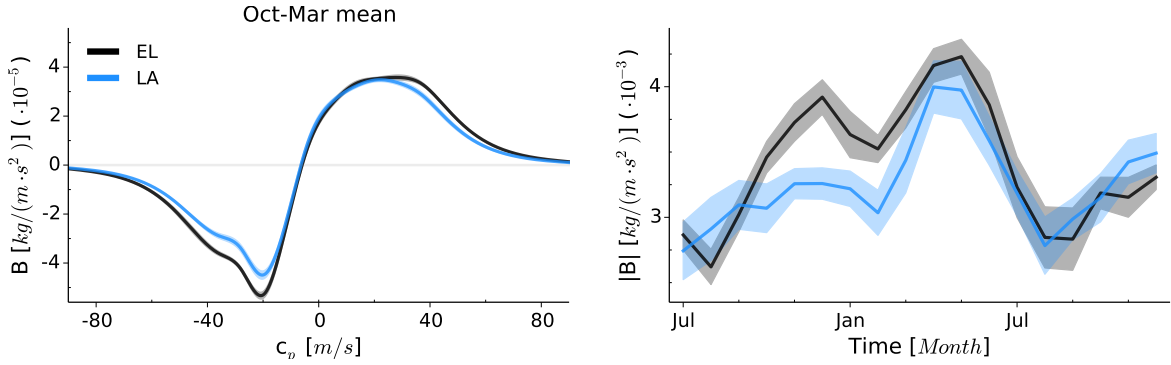


Figure 4.4: Gravity wave source momentum flux B for El Niño (black) and La Niña (blue) conditions during QBOE phase. Gravity wave source momentum flux B for QBOW phase (not shown) is qualitatively similar to QBOE phase. Zonal and meridional mean of B , scaled by density ρ , is determined at the top of convection. Solid lines show the ensemble means and shading indicates the range of two standard deviations (2σ). Left panel: Source spectrum of B as a function of horizontal phasespeed c_p , time mean between October and March. Right panel: Timeseries of total amount of source momentum flux $|B|$ integrated over c_p .

the sum of easterly and westerly waves associated with F_z at 86 hPa, just below the QBO region, shows higher values of momentum fluxes, peaking in DJF, for El Niño compared to La Niña conditions. Note that the 2σ ranges of the El Niño and La Niña timeseries overlap in large parts.

The amount of the parameterized waves responds to the presented changes in tropospheric quantities and increases during El Niño compared to La Niña. The mean source spectrum shows an increase in momentum flux between -60 m/s and -10 m/s phasespeed in the easterly waves, and an increase between 20 m/s and 60 m/s phasespeed in the westerly waves, see left panel in figure 4.4. The timeseries of the total amount of source momentum flux $|B|$ follows, to a first approximation, the timeseries of precipitation, compare right panel of figure 4.2 with right panel of figure 4.4. The total source momentum flux during El Niño is bigger than during La Niña conditions, with a mean increase of $\sim 15\%$ during El Niño compared to La Niña between October and March.

Both resolved and parameterized waves show an increase in wave activity, and also the upwelling w^* in the QBO region increases during El Niño compared to La Niña. The vertical profile of upwelling is positive, and therefore directed upward, throughout the lower stratosphere with a minimum around 50 hPa, see left panel in figure 4.5. During El Niño conditions, we see a general increase, independent of the height of the profile. The timeseries at 30 hPa, chosen as a the mean reference level, shows a strong annual cycle with a minimum in early boreal summer, see right panel of figure 4.5. During El Niño conditions, the upwelling increases compared to La Niña conditions, showing the largest effect around the first boreal winter in the timeseries, in accordance with the strongest difference in ENSO signals and the strongest difference in wave activity.

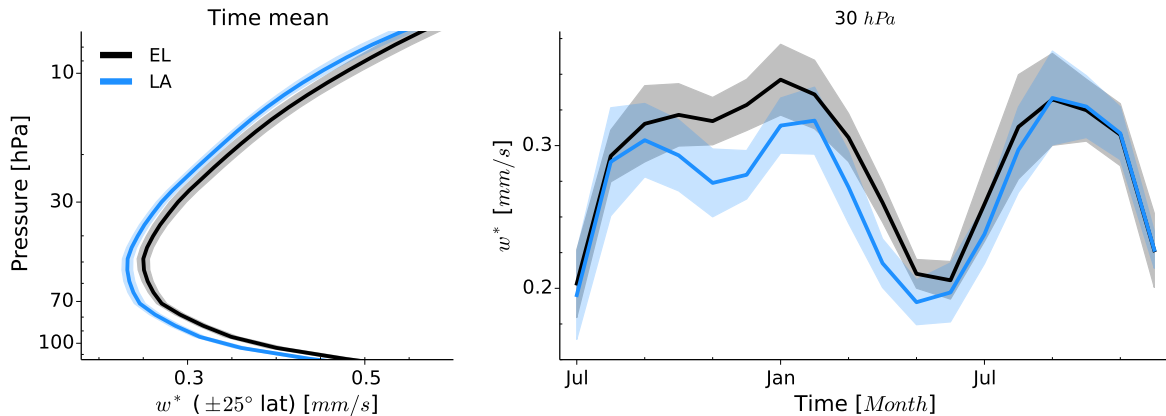


Figure 4.5: Upwelling w^* for El Niño (black) and La Niña (blue) conditions during QBOW phase. Upwelling w^* for QBOE phase (not shown) is qualitatively similar to QBOW phase. Zonal and meridional mean between -25° and $+25^\circ$ latitude. Solid lines show the ensemble means and shading indicates the range of two standard deviations (2σ). Left panel: Vertical profile of time mean. Right panel: Timeseries at 30 hPa.

4.3 Evolution of two QBO phases

As outlined in the experimental setup, we analyze the effect of El Niño and La Niña conditions on the QBO by selecting two phases of the QBO which oppose each other in the position of the jets. We first present results for QBOW, followed by QBOE, before we discuss the results in the subsequent chapter.

4.3.1 QBOW

The initial wind profile of QBOW contains the onset of a westerly jet at around 10 hPa with westerly winds above. Below 10 hPa, the underlying easterly jet extends until 40 hPa, where the remainder of a previous westerly phases resides, see initial profile in July in figure 4.6. In the course of the simulation period, the westerly jet above 10 hPa slowly descends through the lower stratosphere. In the second part of the simulation, the easterly jet below 10 hPa descends and slowly erases the underlying westerly jet, which persists longer during La Niña conditions. Centered around 1 hPa above the main QBO region, the Semi-Annual Oscillation (SAO) shows its periodic change of winds with a period of 6 months. In the following, we present two characteristic QBO quantities, the strength of QBO jets and the downward propagation of the QBO westerly jet and compare these quantities during El Niño and La Niña conditions.

The downward propagation rate illustrates the speed of how quickly the QBO jets descend in time. We determine the onset of the westerly jet and track the vertical position in time, see figure 4.7. At the end of the simulation period of 18 months, the westerly jet extends until 70 hPa during El Niño, while the onset of the westerly jet resides at 50 hPa during La Niña conditions. During El Niño conditions, the QBO westerly jet therefore descends faster than during La Niña conditions. Note that the 2σ ranges of the ensemble do not intersect for most parts, indicating a robust difference between El Niño and La Niña conditions.

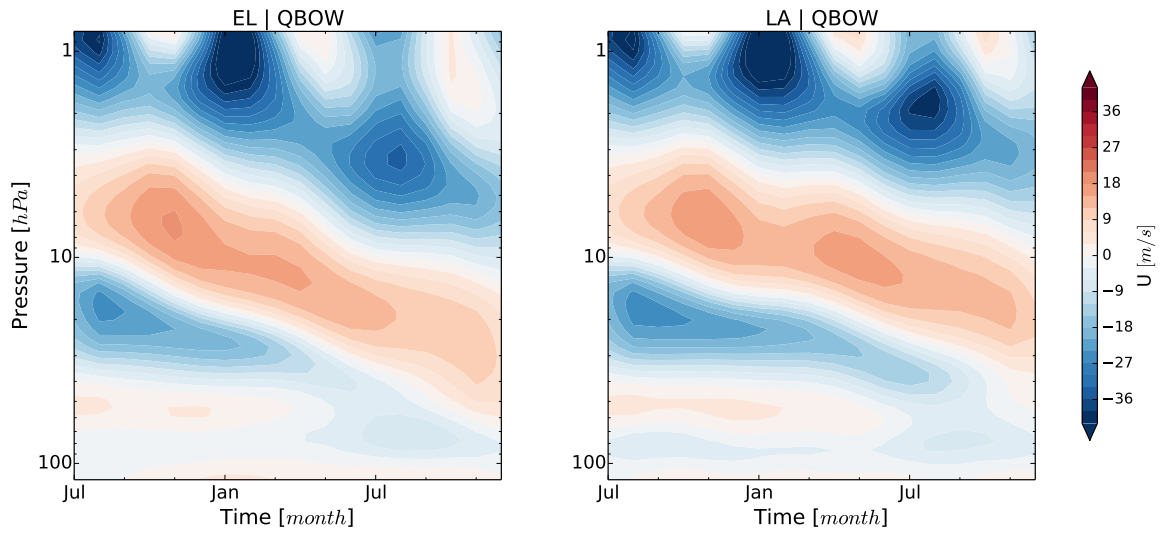


Figure 4.6: Evolution of the QBO for El Niño (left) and La Niña (right) conditions during QBOW phase. Timeseries of the profile of meridional and zonal mean zonal wind U for the ensemble mean.

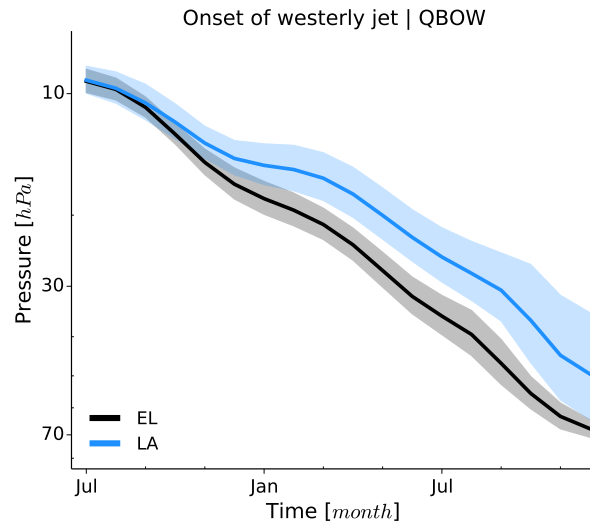


Figure 4.7: Timeseries of the onset of the westerly jet in QBOW for El Niño (black) and La Niña (blue) conditions. Solid lines show the ensemble means and shading indicates the range of two standard deviations (2σ).

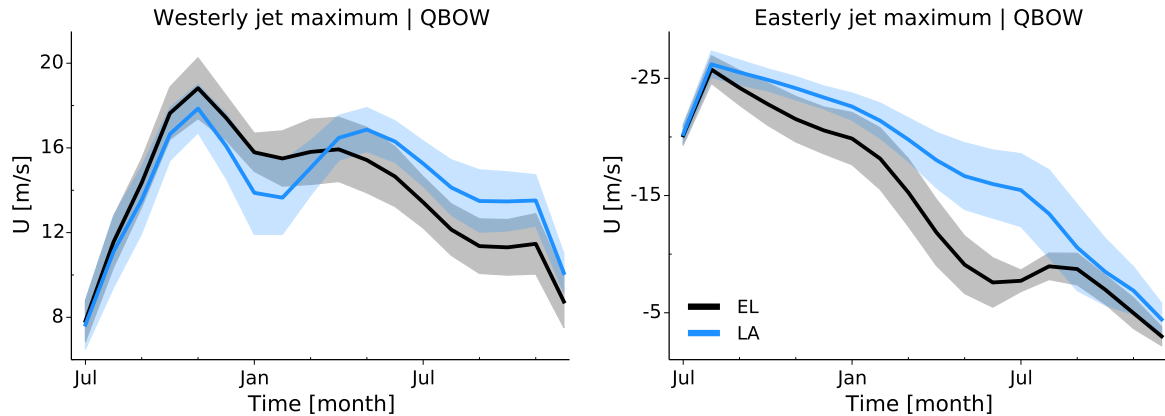


Figure 4.8: Timeseries of the strength of the westerly (left) and easterly (right) jet of QBOW for El Niño (black) and La Niña (blue) conditions. Solid lines show the ensemble means and shading indicates the range of two standard deviations (2σ).

We analyze the strength of the QBO jet by determining the maximum wind speed within the westerly and the easterly jet and track the maximum values in time. The westerly jet, whose position is close to the SAO in the upper stratosphere, exhibits a semiannual signal in jet strength, see left panel in figure 4.8. While the strength of the westerly jet is slightly stronger during El Niño conditions in the first half of the simulation period, the jet strength is weaker during El Niño conditions in the second half of the simulation period, compared to La Niña conditions. The strength of the easterly jet decreases in the course of the simulation during both El Niño and La Niña conditions, while the strength of the easterly jet is generally weaker during El Niño conditions compared to during La Niña conditions, see right panel in figure 4.8.

4.3.2 QBOE

The initial wind profile of QBOE opposes the QBOW profile, with an easterly jet above 10 hPa and a westerly jet below, see initial profiles of figure 4.9. In the course of the experiment, both the easterly and the westerly jet descend through the lower stratosphere while the descending easterly jet eventually terminates the westerly jet in boreal summer of the second year. The downward propagation of the easterly jet is similar for both El Niño and La Niña conditions, see figure 4.10. However the ensemble spread increases strongly during La Niña conditions coinciding with the onset of the strong ENSO signal in early boreal winter. Finally the strength of the QBO westerly jet clearly decreases during La Niña conditions compared to El Niño conditions, see figure 4.11. While the strength of the easterly jet compares well for La Niña and El Niño conditions during the first part of the simulation period, the strength of the easterly jet decreases for La Niña compared to El Niño in the second part of the simulation.

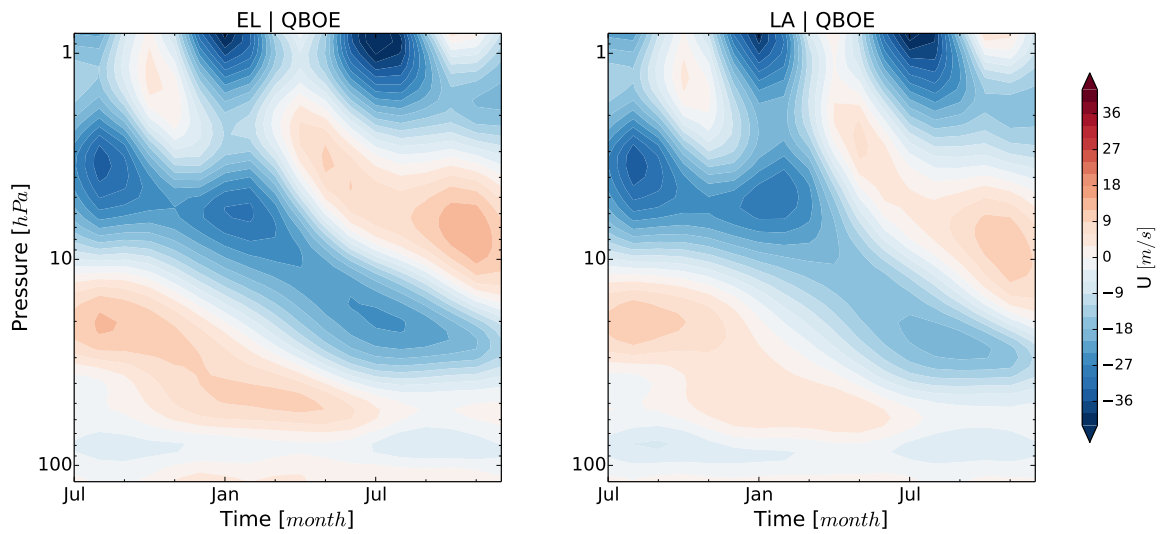


Figure 4.9: Evolution of the QBO for El Niño (left) and La Niña (right) conditions during QBOE phase. Timeseries of the profile of meridional and zonal mean zonal wind U for the ensemble mean.

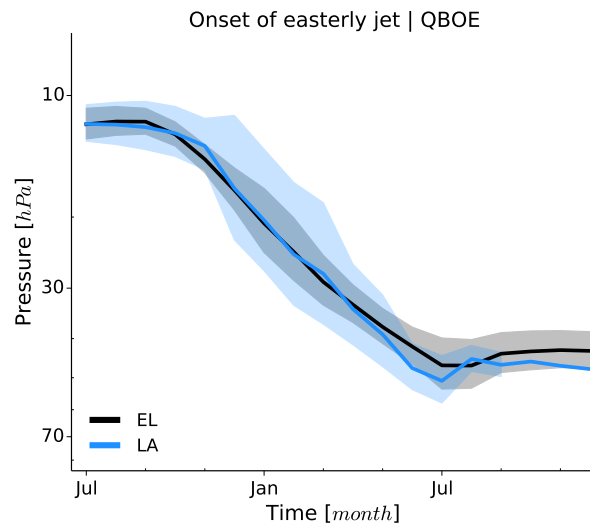


Figure 4.10: Timeseries of the onset of the easterly jet in QBOE for El Niño (black) and La Niña (blue) conditions. Solid lines show the ensemble means and shading indicates the range of two standard deviations (2σ). Note that the ensemble consists of only one member during the last months of La Niña.

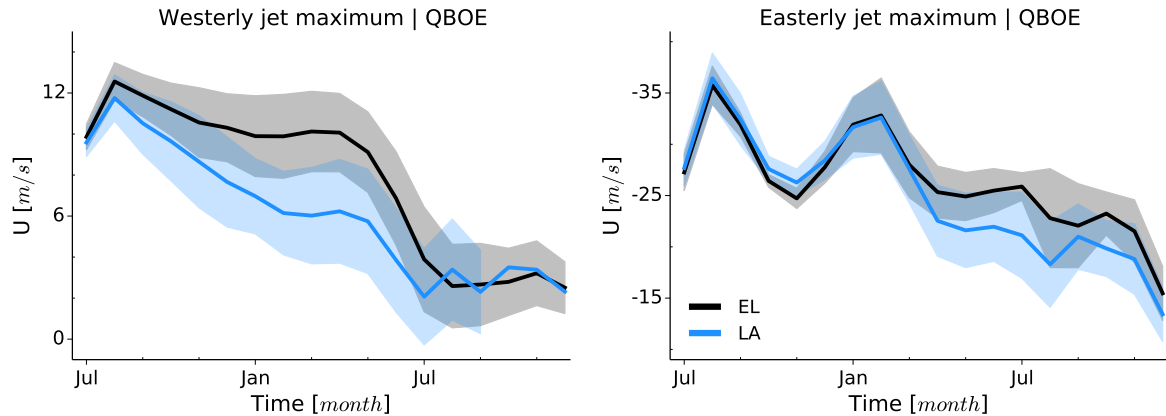


Figure 4.11: Timeseries of the strength of the westerly (left) and easterly (right) jet of QBOE for El Niño (black) and La Niña (blue) conditions. Solid lines show the ensemble means and shading indicates the range of two standard deviations (2σ). Note that the ensemble for the westerly jet consists of only one member during the last months of La Niña.

4.4 Discussion

We briefly summarize the preceding results which serve as the basis for the following discussion. During El Niño conditions, wave activity increases, which on one hand increases the QBO forcing due to waves, on the other hand increases the tropical upwelling which counteracts QBO forcing due to waves. We therefore observe an increase in two opposing QBO forcings in El Niño compared to La Niña conditions. The changes in QBO forcing due to El Niño and La Niña act similarly on both QBOW and QBOE, yet the jets of QBOW and QBOE react differently: On one hand, the westerly jet of QBOW descends quicker, figure 4.7, and the underlying easterly jet below the westerly jet is weaker during El Niño, right panel in figure 4.8. On the other hand, the easterly jet of QBOE descends with similar speed during El Niño and La Niña, figure 4.10, and the underlying westerly jet is stronger during El Niño, left panel in figure 4.11.

The QBO forcing quantities presented in the previous chapter give a first insight into changes in QBO forcing mechanisms. In a next step we analyze the zonal wind tendencies resulting from those QBO forcings to better understand the reaction of the QBO to changes in QBO forcing during El Niño and La Niña conditions. However, comparing the tendency profiles of two QBOs, with different wind profiles, does not induce a straight-forward conclusion because the exerted acceleration due to a given QBO forcing also depends on the QBO wind profile itself. For instance, the strength of the QBO jet itself determines the amount of waves that dissipate and therefore the amount of wind tendency due to waves. Comparing two QBO profiles with different jet strength, we can't correctly attribute the change in tendency either to a change in QBO forcing, such as an increase wave activity, or to a change in tendency due to the change in jet strength. A very similar argumentation holds for the tendency associated with the secondary circulation and the upwelling. While we treat the large-scale upwelling associated with the Brewer-Dobson circulation as a QBO forcing, the secondary circulation of the QBO with its associated horizontal and vertical advection depends on

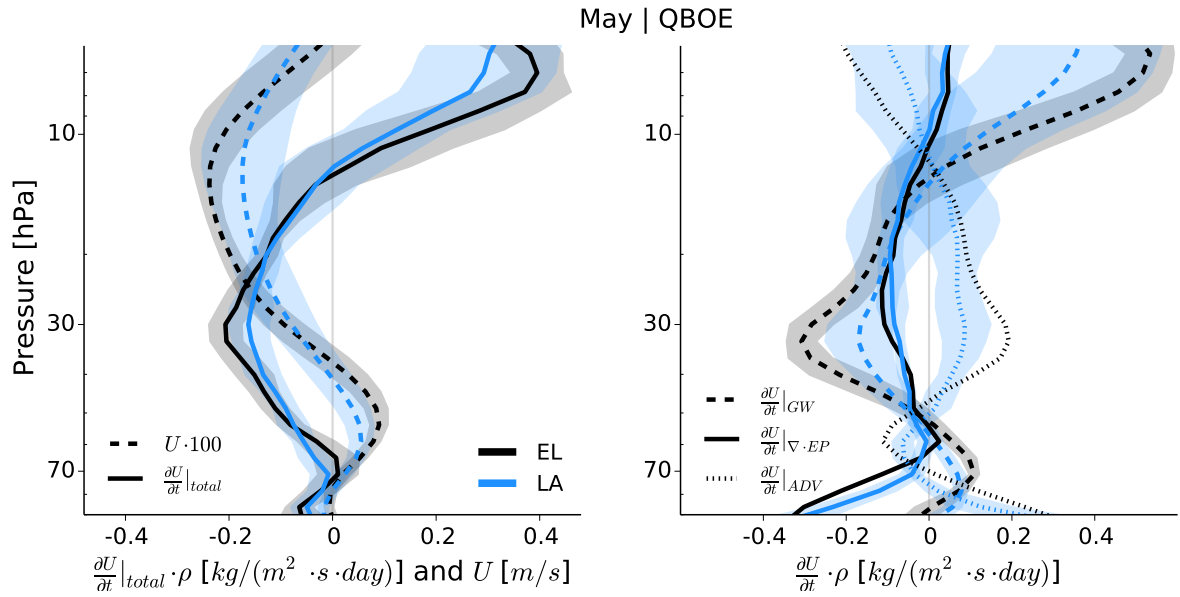


Figure 4.12: Vertical profile of zonal wind U and its tendency $\frac{\partial U}{\partial t}$ for QBOE in May of the second year for El Niño (black) and La Niña (blue) conditions. Lines show the ensemble means and shading indicates the range of two standard deviations (2σ). Left panel: Zonal wind (dashed), scaled by a factor 100, and total tendency $\frac{\partial U}{\partial t}|_{total}$ (solid). Right panel: Tendency components of resolved waves $\frac{\partial U}{\partial t}|_{\nabla \cdot EP}$ (solid), gravity waves $\frac{\partial U}{\partial t}|_{GW}$ (dashed) and advection $\frac{\partial U}{\partial t}|_{ADV}$ (dotted).

the QBO jet strength. Two QBOs with different wind profiles will necessarily exhibit different tendency profiles, even if the two QBOs experience the identical QBO forcing.

In order to illustrate the sometimes limited informative value of comparing tendency profiles of different QBOs, we show tendency profiles for the month of May in the second year for the QBOE initial condition. At this time, the QBO under El Niño and La Niña has evolved in the course of the experiment and shows a different wind profile for El Niño and La Niña conditions. While the onset of the westerly jet coincides at ~ 40 hPa for both El Niño and La Niña conditions, the amplitude of the jets differ, see left panel of figure 4.12. The total tendency $\frac{\partial U}{\partial t}|_{total}$ for El Niño exceeds La Niña conditions and the larger tendency for El Niño is consistent with the identical downward propagation speed for El Niño and La Niña. In order to descend with a similar speed, the QBO in El Niño with stronger amplitude requires more tendency than the QBO in La Niña with a weaker amplitude. The individual tendency profiles, which add up to the total tendency, each differ under El Niño and La Niña conditions, see right panel in figure 4.12. While the wind tendency due to gravity waves $\frac{\partial U}{\partial t}|_{GW}$ and the tendency due to advection $\frac{\partial U}{\partial t}|_{ADV}$ change by about a factor 2, the tendency due to the resolved wave $\frac{\partial U}{\partial t}|_{\nabla \cdot EP}$ increases only slightly during El Niño compared to La Niña conditions. Since in this case, both the background wind and the QBO forcing mechanisms differ at the same time, we can't identify the contribution of either of the two causes to changes in the tendency profile.

Having pointed out the limitations of an analysis of QBO tendency profiles, we nevertheless can deduce informative value from tendency profiles of QBOs, if the QBOs exhibit a similar wind structure. For both QBOW and QBOE, we choose the onset

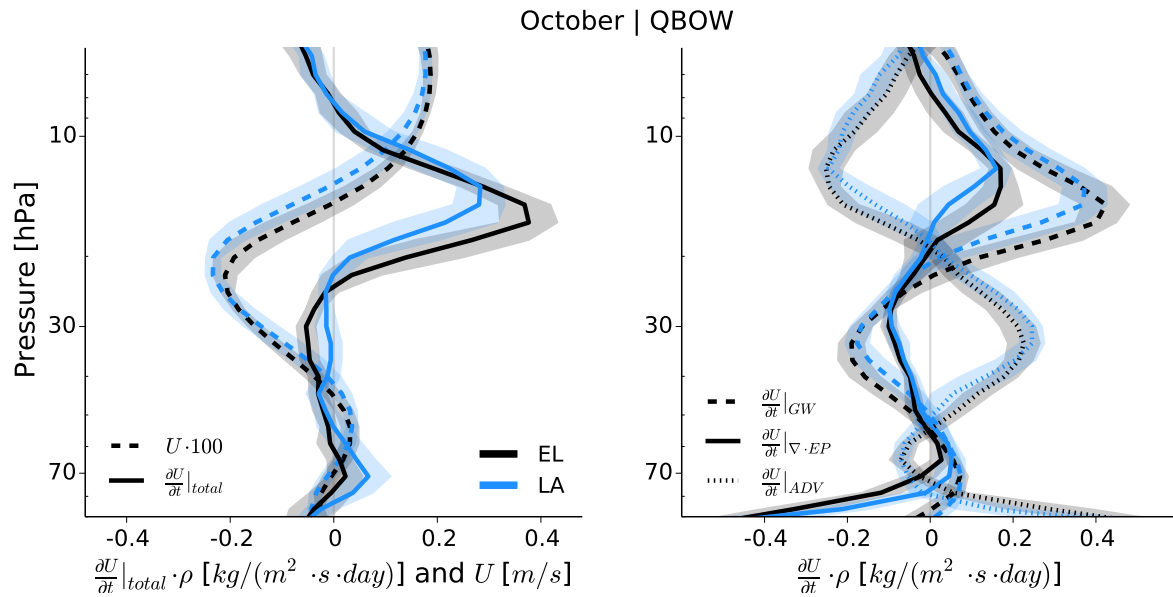


Figure 4.13: Same as figure 4.12, but for October of the first year instead of May of the second year and for QBO instead of QBOE.

of the ENSO signal in October of the first year, four months after the start of the simulation, to compare tendency profiles of El Niño and La Niña conditions. Even though the ENSO signal peaks later in time, and the difference in QBO forcing would then be strongest, we choose the onset of the ENSO signal because the QBO profiles are still similar in October of the first year. At a later point in time, the wind profiles differ strongly and do not allow for sound reasoning as pointed out in the previous paragraph.

4.4.1 QBOW

In October, the onset of the westerly jet of QBOW is situated at ~ 15 hPa with an easterly jet below, see left panel in figure 4.13. The profiles under El Niño and La Niña conditions still show comparable characteristics but differ already. The onset of the westerly jet is lower during El Niño conditions than during La Niña conditions. As a consequence, also the profile of the total tendency $\frac{\partial U}{\partial t}|_{total}$ peaks at a lower position during El Niño than during La Niña conditions. However also the peak value during El Niño exceeds the peak value during La Niña conditions, which we don't associate with the slightly lower westerly jet, but with a change in QBO forcing. The change in the total tendency is caused by the resolved waves $\frac{\partial U}{\partial t}|_{\nabla \cdot EP}$ and the parameterized waves $\frac{\partial U}{\partial t}|_{GW}$, see right panel in figure 4.13. While the exerted acceleration increases for both wave components during El Niño, the tendency due to advection $\frac{\partial U}{\partial t}|_{ADV}$ only changes the vertical position, following the wind profile, but does not change its peak value.

We conclude from this analysis that the increase in wave forcing, as described in chapter 4.2.2, exerts more acceleration and therefore leads to a quicker downward propagation of the westerly jet during El Niño conditions, compared to La Niña conditions. We

base this conclusion on findings from chapter 3.1.2, which shows that the amount of exerted acceleration correlates with the speed of the QBO jet downward propagation. We don't detect any signal of the observed increase in upwelling in the tendency profile. In addition, the strength of the underlying easterly jet weakens in the course of the experiment for El Niño compared to La Niña conditions, see right panel in figure 4.8. A weaker easterly jet, which is positioned under the westerly jet, also favors a quicker downward propagation of the westerly jet, because the easterly jet requires less momentum to be eroded. Summarizing the two aspects, the increase in wave forcing and the weaker easterly jet lead to a quicker downward propagation of the westerly jet during El Niño compared to La Niña conditions.

4.4.2 QBOE

In October, the QBO tendency profile for QBOE shows similar characteristic changes during El Niño as for QBOW. For QBOE in October, the easterly jet above ~ 15 hPa is situated above a westerly jet which extends down to 70 hPa, see left panel of figure 4.14. The total tendency increases during El Niño compared to La Niña, along with a lower peak in the gravity wave component in agreement with the slightly lower position of the onset of the easterly jet during El Niño. As for QBOW, both wave components, dominated by the gravity waves, cause the increase in total tendency while the tendency due to advection remains unchanged in strength, see right panel in figure 4.14.

Following the previously presented argumentation that increased total tendency leads to a quicker downward propagation of the QBO jet, we would expect a faster downward propagation speed of the easterly jet in QBOE. However, we observe no change in downward propagation speed of the easterly jet in QBOE during El Niño compared to La Niña conditions, see figure 4.10. We explain this apparent discrepancy by considering the second aspect that also controls the downward propagation speed, which is the strength of the underlying jet. While for QBOW the underlying easterly jet is weaker during El Niño, the underlying westerly jet in QBOE is stronger during El Niño, see left panel in figure 4.11. While a relatively weaker underlying jet favors a faster downward progression of the above jet, a relatively stronger underlying jet inhibits a faster downward propagation of the above jet.

For QBOE we conclude that the increase in wave forcing, and therefore the increase in exerted acceleration, is balanced by the increase in the underlying jet strength during El Niño compared to La Niña conditions. The changes of the two opposing mechanisms cancel each other which leads to no changes in the downward propagation of the easterly jet during El Niño and La Niña conditions. For QBOW in contrast, the weaker underlying jet, in addition to an increase in wave forcing, both favor a faster downward propagation speed of the jet.

4.5 Summary

In an idealized experimental setup we generate two ensembles, each containing 10 members, with opposing QBO initial conditions. While QBOW includes a westerly jet

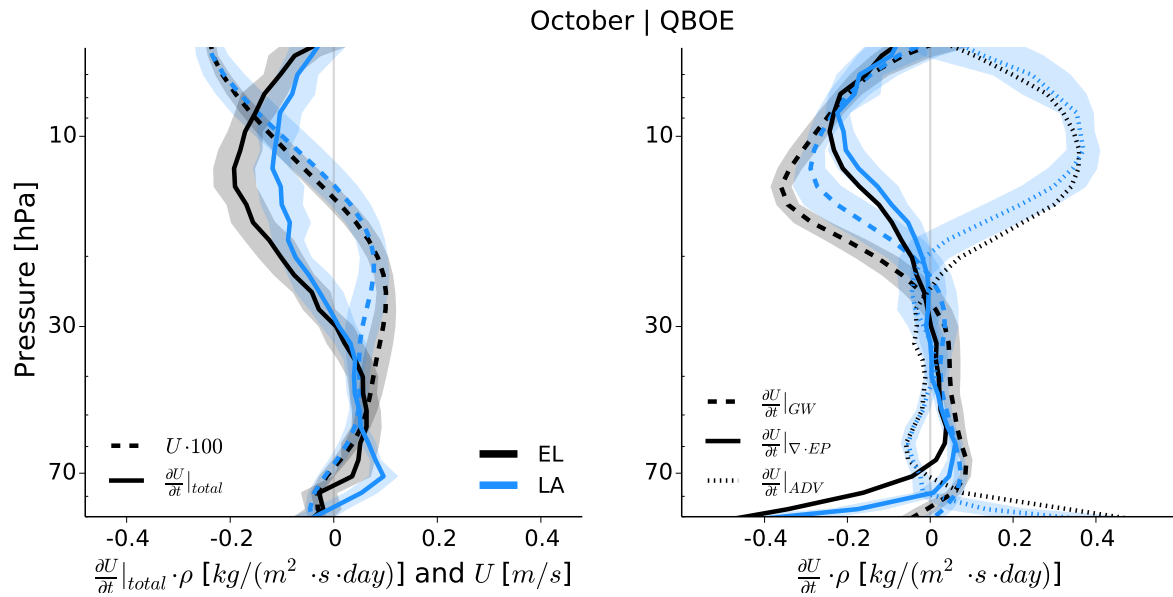


Figure 4.14: Same as figure 4.12, but for October of the first year instead of May of the second year.

above 10 hPa and an easterly jet below, QBOE contains an easterly jet above 10 hPa and a westerly jet below. In atmosphere-only simulations, both QBOW and QBOE ensembles experience El Niño and La Niña boundary conditions, which we composite from observed SSTs and SICs of particularly strong El Niño and La Niña events of the last decades. We compare the evolution of the two QBO phases, QBOW and QBOE, under the two different boundary conditions of El Niño and La Niña to isolate the effect of ENSO on the QBO. See figure 4.1 for an illustration of the ensemble generation and the experimental setup.

During El Niño conditions, the globally higher SSTs and the associated increased tropospheric convection is a manifestation of an increase in wave activity. Stronger wave activity has two opposing effects on the net QBO forcing. On one hand an increase in tropospheric wave activity, the main QBO forcing, leads to stronger QBO forcing. On the other hand, stronger wave activity leads to an intensification of the tropical upwelling in the lower stratosphere, which counteracts QBO wave forcing. While studies show an increase in upwelling during El Niño (Hardiman et al., 2007; Randel et al., 2009), Ortland and Alexander (2014) show in detail that increased wave activity in the tropics increases upwelling in the lowermost stratosphere.

The ENSO signal of El Niño and La Niña causes differences in QBO behaviour, depending on the initial condition of the QBO. During El Niño the westerly jet in QBOW descends faster and the underlying easterly jet is weaker than during La Niña conditions. The easterly jet in QBOE descends with similar speed during both El Niño and La Niña conditions while the underlying westerly jet is stronger during El Niño compared to La Niña. An analysis of the zonal wind tendency profile helps to explain the results. The increase in total tendency at the beginning of the ENSO signal shows an increase in the tendency due to both resolved and parameterized waves. Despite the stronger diagnosed upwelling, the tendency due to advection does not change.

The presented results agree with findings of Calvo et al. (2010), who show no change in QBO downward progression speed for the easterly jet, but observe a faster downward progression during El Niño for the westerly jet. Furthermore Calvo et al. (2010) observe no change in amplitude in both the easterly and the westerly jet during El Niño conditions. This also agrees with our results that do not show any systematic change in amplitude of the upper QBO jets. We can't compare our results with the observational study of Taguchi (2010) in a detailed way, because the authors use vertically integrated values of QBO quantities including both the upper and the lower QBO jet. However, Taguchi (2010) also find a faster downward propagation speed during El Niño, dominated by the westerly jet. Apart from confirming findings of previous studies on the influence of ENSO on the QBO, we further show the mechanisms and reasons for the observed changes in QBO downward propagation. For the presented mechanism and reasons for the observed changes in QBO downward propagation see the conclusions in chapter 6.

Chapter 5

Sensitivity of the QBO to different gravity wave parameterizations in a warmer climate

Changes in QBO period, due to a warmer climate, differ depending on the GCMs of various modeling centers. Those GCMs include different gravity wave parameterizations. In this chapter we analyze how the choice and the tuning of the gravity wave parameterization explains the spread in the changes in QBO period simulated by different GCMs.

5.1 Experimental Setup

We use the atmospheric general circulation model ECHAM6 (Stevens et al., 2013) to perform atmosphere-only simulations for two different climates, a present day climate and a warmer climate. The boundary conditions for the present day climate correspond to AMIP conditions, defined as in Taylor et al. (2012), including observed sea surface temperatures (SST) and sea ice concentrations for the period 1979 until 2008. The warmer climate uses the same SST patterns as in AMIP, but increased uniformly by 4K (AMIP4K), while all other boundary conditions remain unchanged. We omit additional changes in CO₂ concentrations in our experimental setup because changes in SSTs dominate QBO changes in a warmer climate (Kawatani et al., 2012). Unless otherwise stated we analyze monthly, zonal and meridional, $\pm 10^\circ$ latitude, mean data of a 30 year period for each of the experiments. For comparison of QBO properties in chapter 5.2.1 we use the reanalysis product ERA-Interim (Dee et al., 2011).

5.1.1 Setup of gravity wave parameterizations

In this study we compare four different setups of non-orographic gravity wave parameterizations in the tropics. In the extratropics all four parameterization setups share

Acronym	Hines	AD	AD+Beres	ADfixBeres
Propagation	Hines	AD	AD	AD
ϵ	-	0.001	0.0025	0.0025
λ_h	126 km	100 km	100 km	100 km
Sources	prescribed	prescribed	interactive	prescribed
Launch level	600 hPa	600 hPa	cloud top	130 hPa
Spectrum shape	symmetric	symmetric	asymmetric	as AD+Beres
c_{max}	-	8 m/s	$\pm \sim 20$ m/s	as AD+Beres

Table 5.1: Overview of different gravity wave parameterization setups: The experiment acronym as used in this work, the propagation scheme, the intermittency value ϵ of the propagation scheme AD99, the horizontal wavelength λ_h , the nature of momentum flux sources (interactive or prescribed), the waves’ launch level, details on the symmetry of the source spectrum and the phase speed c_{max} where the momentum flux source spectrum peaks. Note that “as AD+Beres” refers to the zonal, meridional and time mean.

the identical gravity wave parameterizations. The different gravity wave parameterization setups consist of either a gravity wave propagation scheme with fixed gravity wave sources or a combination of a gravity wave propagation scheme coupled to an interactive gravity wave source parameterization. The gravity wave parameterization setups or parts of the gravity wave parameterization setups are employed in various GCMs of different modeling centers. (1|Hines) is the standard parameterization setup of ECHAM6 and the model version employed for CMIP5. We set up (2|AD) as an analogue to (1|Hines), such that (2|AD) also launches a prescribed, constant spectrum of gravity waves at the same height as (1|Hines). However the propagation scheme’s design and wave breaking criteria differ among the two gravity wave parameterization setups. (3|AD+Beres) is a gravity wave parameterization setup introduced in chapter 2.1 with the aim to gain physical coupling between the modeled convection and the excited gravity waves. Finally we design (4|ADfixBeres) to analyze the effect of the interactive source spectrum of (3|AD+Beres). We summarize the different gravity wave parameterization setups in table 5.1 and explain the detailed parameterization setups individually in the following paragraphs.

1 | Hines The standard ECHAM6 model version, which is part of CMIP5, employs the gravity wave scheme after Hines which is based on the Doppler spread theory (Hines, 1997a,b). The scheme launches a broad band spectrum of waves at 600 hPa with constant amplitude in time and longitude. In the CMIP5 model setup, a latitudinal amplitude enhancement is introduced around the equator in order to obtain a QBO with a realistic period (Schmidt et al., 2013). The latitudinal enhancement is achieved by setting u_{rms} , the parameter for the gravity wave source strength, to 1.2 m/s near the equator, latitude $|\Phi| \leq 5^\circ$, while $u_{rms} = 1$ m/s outside the tropics.

For the following three parameterization setups, we disable the Hines scheme in the tropics ($\pm 20^\circ$ latitude) and keep it active only in the extratropics. Since the following three gravity wave parameterization setups excite waves only in the tropics, all four parameterizations share the identical Hines gravity wave parameterization setup in the

extratropics.

2 | AD The spectral gravity wave propagation scheme after Alexander and Dunkerton (1999, hereafter AD99) is based on the assumption that momentum fluxes carried by waves are deposited entirely at the initial onset of linear instability, which corresponds to the breaking criterion after Lindzen (1981). We use the scheme with modifications reducing the scheme’s computational cost (Ortland and Alexander, 2006). The gravity wave source spectrum of momentum flux B remains constant in space and time and is calculated by equation (29) of AD99

$$B(c) = B_m \rho \left(\frac{c}{c_{max}} \right) \exp \left(1 - \left| \frac{c}{c_{max}} \right| \right) \quad (5.1)$$

with phase speed c , peak phase speed $c_{max} = 8 \text{ m/s}$, density ρ and maximum flux magnitude $B_m = 7 \cdot 10^{-4} \text{ m}^2/\text{s}^2$. The shape of the chosen source spectrum lies within the range of observed spectra (Alexander and Holton, 1997; Piani and Durran, 2001; Alexander et al., 2006; Kuester et al., 2008).

3 | AD+Beres We couple the convection based gravity wave source parameterization after Beres et al. (2004) to the gravity wave propagation routine AD99. On each model grid point and each timestep, the gravity wave source parameterization generates an interactive source spectrum based on the latent heating properties and the background wind. The scheme’s advantages over a prescribed, constant spectrum are twofold. First, the shape of source spectrum is generated interactively dependent on physical properties and therefore, secondly, the source spectrum includes spatial and temporal variability. Waves are launched at the top of the convective heating, ranging from 3.5 km up to 17 km . For details on the implementation of the scheme in ECHAM6 and the scheme’s physical coupling to the sources see Schirber et al. (2014) or chapter 2.1.

4 | ADfixBeres We extract the zonal, meridional and time mean spectrum of the AD+Beres AMIP experiment and prescribe this spectrum as a fixed and constant spectrum for AD99. In present day climate AD+Beres and ADfixBeres show an identical source spectrum. While the source spectrum for ADfixBeres remains constant in both present and warmer climate, the source spectrum of AD+Beres will change in a warmer climate, due to its interactive nature. Therefore the setup ADfixBeres allows to analyze the effect of the interactive source spectrum of AD+Beres in the warmer climate. The ADfixBeres setup launches waves at 130 hPa which corresponds to the height where the Beres scheme shows the peak momentum fluxes in ECHAM6, see figure 2.6. We consider the high temporal and spatial intermittency of the Beres source parameterization in present climate by launching waves only on a small spatial fraction of gridpoints in ADfixBeres. Note that the tuning of the propagation scheme AD99 in ADfixBeres is identical to AD+Beres, with horizontal wavelength $\lambda_h = 100 \text{ km}$ and intermittency factor $\epsilon = 0.0025$.

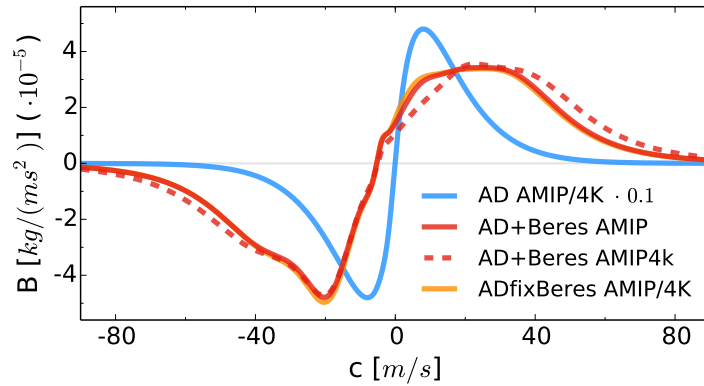


Figure 5.1: Momentum flux (B) source spectrum as a function of horizontal phase speed (c) for the experiments AD, AD+Beres and ADfixBeres; time, zonal and meridional mean. While the spectra of AD (blue) and ADfixBeres (orange) remain unchanged under AMIP and AMIP4K boundary conditions, the interactive source spectrum of AD+Beres (solid red) changes under the warmer climate of AMIP4K (dashed red). Note that the spectrum of AD is scaled by 0.1 for visualization reasons. ADfixBeres is hidden for the most part by AD+Beres AMIP.

We tune all four parameterization setups individually to simulate the QBO of present day climate, with a focus on the QBO period. While the parameterizations provide a variety of tuning parameters, we restrict our tuning to two aspects in the three AD based parameterization setups. First, the intermittency ϵ and the horizontal wavelength λ_h of AD99 influence the breaking levels where gravity waves become convectively unstable. Second, the amplitude of the source spectrum determines the amount of emitted source momentum flux. Relevant parameters for the latter aspect are B_m for AD and c_f and L for Beres with details in chapter 2.1.2.

5.1.2 Source spectra of momentum flux

The momentum flux source spectra of the three AD based parameterization setups are shown in figure 5.1. The spectra B are scaled by density ρ and calculated at the respective launch levels, ranging from 600 hPa in AD to 130 hPa ADfixBeres and distributed over the entire troposphere in AD+Beres. Since AD launches waves at a much lower level than AD+Beres and ADfixBeres, the amount of source momentum flux in AD is an order of magnitude larger than AD+Beres and ADfixBeres, see 5.1. However in the lower stratosphere below the QBO relevant heights, see figure 5.8, the absolute amount of momentum flux for each of the four parameterization setups lies within the range of observations, with mean absolute momentum fluxes varying between 1 – 5 mPa (Sato and Dunkerton, 1997; Piani et al., 2000; Grimsdell et al., 2010; Geller et al., 2013).

The symmetric source spectrum of AD peaks at 8 m/s , while the interactively generated spectrum of AD+Beres is asymmetric and shows a peak around 20 m/s phase speed. Due to its physically based character, the source spectrum of AD+Beres in AMIP4K is different to the source spectrum under AMIP boundary conditions, while both the AD and ADfixBeres source spectra are by construction constant under different boundary

conditions. Note that the source spectrum of Hines does not appear in figure 5.1, because the parameterization's design does not allow a straightforward calculation of a momentum flux source spectrum as a function of horizontal phase speed. As for AD and ADfixBeres, we set the source characteristics of Hines constant under the different boundary conditions of AMIP and AMIP4K.

5.2 Results

5.2.1 QBO characteristics in a warmer climate

In the warmer climate several QBO characteristics are changing in the different parameterization setups. The QBO composites in figure 3.2 show differences in QBO amplitude, in the vertical extent of easterly and westerly jets, in their downward propagation speeds, in the QBO period and in the position of the tropopause. In order to systematically analyze the QBO changes across the suite of parameterization setups, we focus on the two main QBO characteristics: The QBO period and the QBO amplitude. We determine the QBO period calculating the onsets of the westerly jet at 20 *hPa* in time. Changing the vertical level or analyzing the onset of the easterly jet gives qualitatively similar results for the QBO period. We determine the QBO amplitude calculating the maximum value of the easterly and the westerly jet of each QBO oscillation on each level. Given a timeseries of 30 years, we then average over the maximum jet values and also calculate a standard deviation on each level for both the easterly and the westerly jet.

In the present climate the mean QBO periods among the different parameterization setups range between ~ 26 and ~ 29 months which lies in the observed range of QBO periods with a mean of ~ 28 months, indicated by ERA-Interim, see figure 5.3. In the warmer climate the QBO period remains, to a first approximation, constant for the parameterization setups Hines and ADfixBeres. However, the QBO period becomes shorter by roughly 30% or 8 to 9 months for the AD and AD+Beres parameterization setup. While the spread of the distribution increases in both Hines and ADfixBeres in a warmer climate, the spread of the distribution in AD and AD+Beres remains unchanged under AMIP and AMIP4K boundary conditions.

While we present the QBO period changes, we further highlight the individual descent durations of the easterly and the westerly jet, see figure 5.4. The descent durations of the easterly and the westerly QBO jet remain roughly constant for Hines and ADfixBeres, while the QBO jet descent durations decrease for AD and AD+Beres. In the latter two cases, note that both easterly and westerly descent durations change comparably. Therefore we show that not one particular phase of the QBO contributes to the reduction in QBO period, but a decreased descent duration in both easterly and westerly QBO jets.

The changes in QBO amplitude in the warmer climate depend on the parameterization setup, but also show one common feature. In all parameterization setups, the easterly jet below 10 *hPa* becomes weaker in the warmer climate, see figure 5.5. While the easterly jet loses strength also above 10 *hPa* in AD+Beres, an amplitude reduction

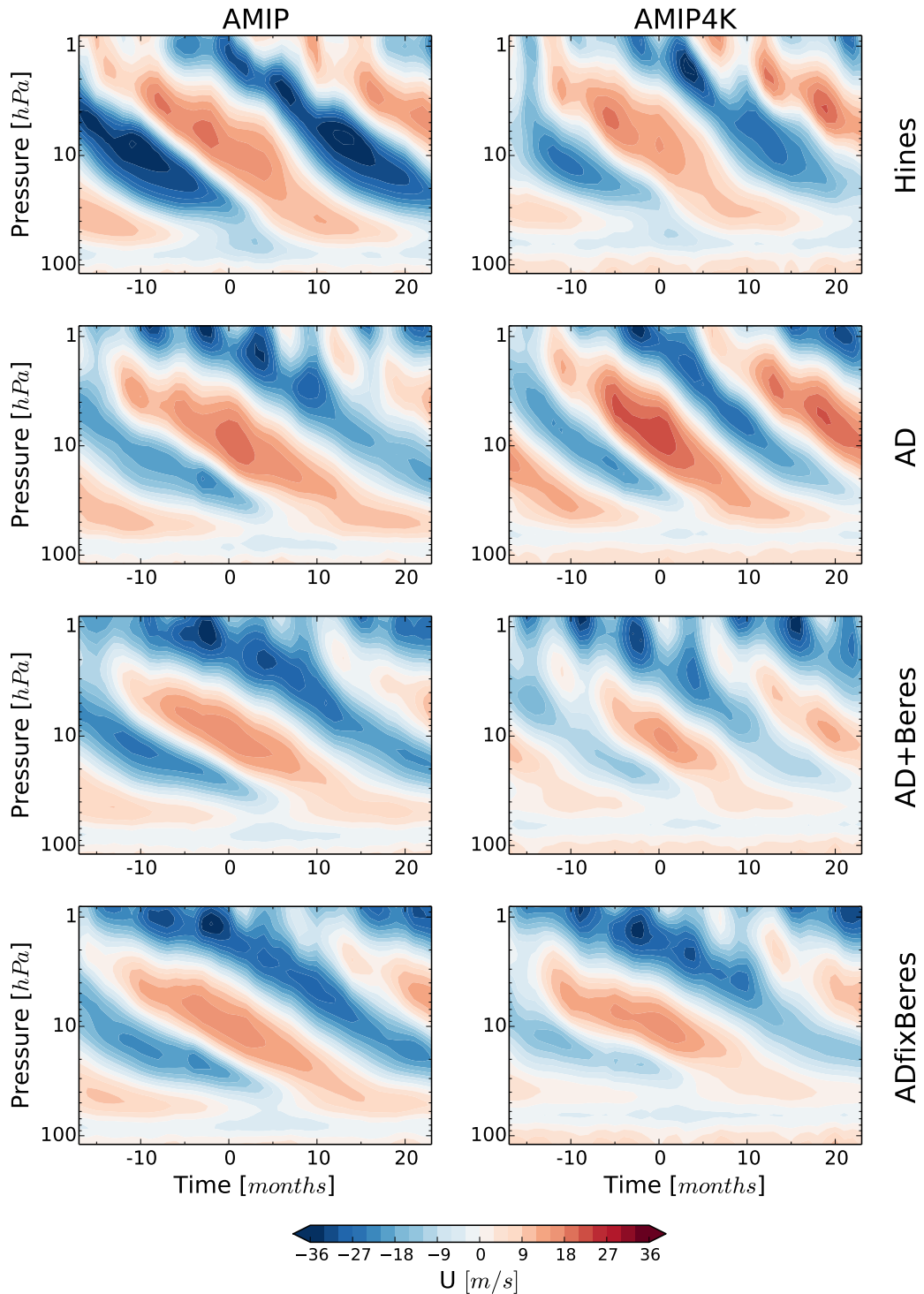


Figure 5.2: QBO composites for the experiments Hines, AD, AD+Beres and ADfixBeres, each for present day (left column) and warmer climate (right column). The onset of the westerly jet at 20 hPa is chosen as the criterion to calculate the composite, compiled from zonal and meridional mean zonal wind.

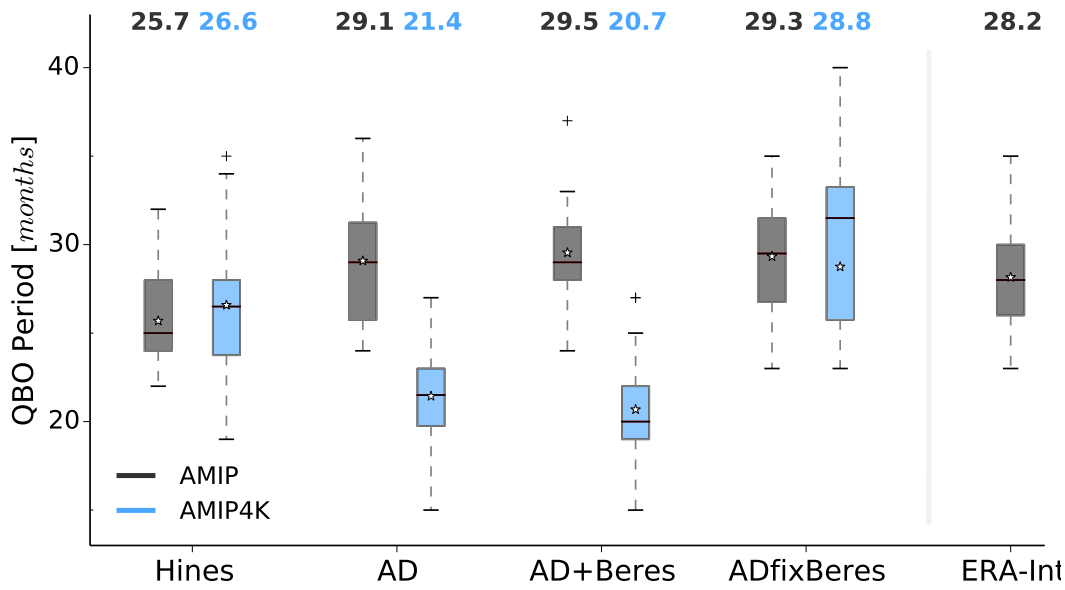


Figure 5.3: Distribution of QBO periods for the experiments Hines, AD, AD+Beres and ADfixBeres, each for present day (black) and warmer climate (blue), and the reanalysis ERA-Interim for present day climate. Periods are determined at the onset of the westerly jet at 20 hPa , compiled from zonal and meridional mean zonal wind. The distribution median is depicted by the horizontal line within each box, the distribution mean by the star whose value is drawn above. The box covers the interquartile range, distribution outliers are denoted by +.

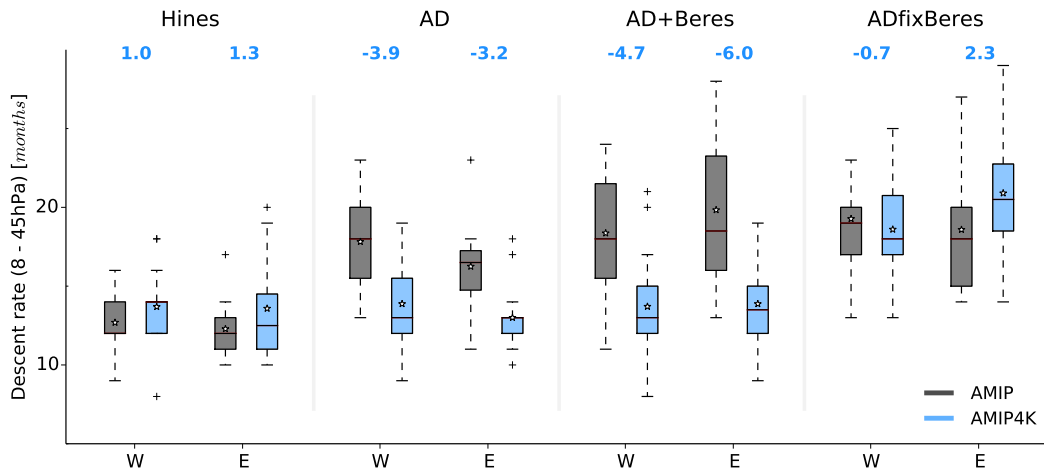


Figure 5.4: Distribution of QBO jet descent rates for the experiments Hines, AD, AD+Beres and ADfixBeres, each for present day (black) and warmer climate (blue), compiled from zonal and meridional mean zonal wind. The descent rate is determined for the westerly (W) and easterly (E) jet by calculating the time the wind maxima take from 8 hPa until 45 hPa . The difference (AMIP4K-AMIP) in the mean is drawn above. For details on box properties see figure 5.3.

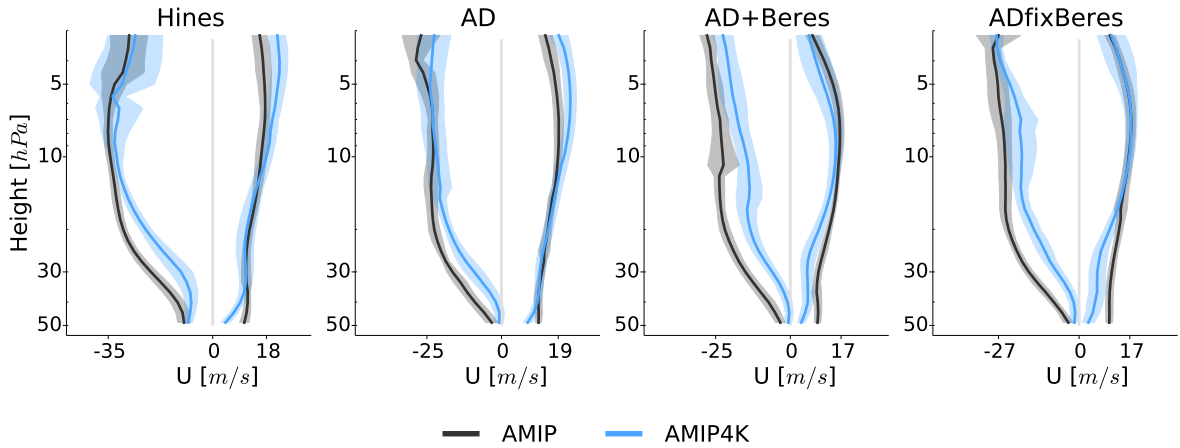


Figure 5.5: Vertical QBO amplitude profiles for the experiments Hines, AD, AD+Beres and ADfixBeres, each for present day (black) and warmer climate (blue), compiled from zonal and meridional mean zonal wind. The amplitude is calculated as the mean maximum wind speed of the QBO easterly ($U < 0$) and westerly ($U > 0$) jets on each vertical level. The shading illustrates the range of two standard deviations σ . The labels on the x-axis show the maximum value of the AMIP profiles.

above 10 hPa is less clear for Hines, AD and ADfixBeres. The westerly jet below 20 hPa remains unchanged for Hines and AD, whereas the westerly jet becomes weaker by $\sim 40\%$ for AD+Beres and ADfixBeres below 20 hPa . Above 20 hPa the westerly jet increases for Hines and AD while it remains rather unchanged for AD+Beres and ADfixBeres. We don't observe any consistent, detailed trend in variance of QBO amplitude among the different parameterization setups. However generally speaking, we qualitatively state that the variance of QBO amplitude tends to increase rather than decrease in a warmer climate. Note that a longer simulation with more resolved QBO cycles would be needed for a more precise statement on the variance of QBO amplitude.

5.2.2 Resolved waves and upwelling

The changes in resolved waves, due to a warmer climate, exhibit a consistent behaviour among the simulations of all parameterization setups. In the regions below the QBO, we show the vertical component F_z of the Eliassen-Palm (EP) flux vector as a measure of the resolved wave activity, see figure 5.6. In the warmer climate, F_z increases for both westerly and easterly waves while the westerly waves show a stronger increase in magnitude than the easterly waves, see left panel in figure 5.6. Since the QBO is driven by a range of waves with different scales, we show the integral of F_z for the two components. A more detailed spectral analysis, which we do not present here, shows that the increase in resolved wave activity occurs at all wave numbers and is not dominated by a particular wave mode. The combined magnitude of easterly and westerly resolved waves, the absolute value $|F_z|$, increases in the warmer climate, see center panel of figure 5.6. The combined magnitude of easterly and westerly resolved waves, the absolute value $|F_z|$, increases in the warmer climate, see center panel of figure

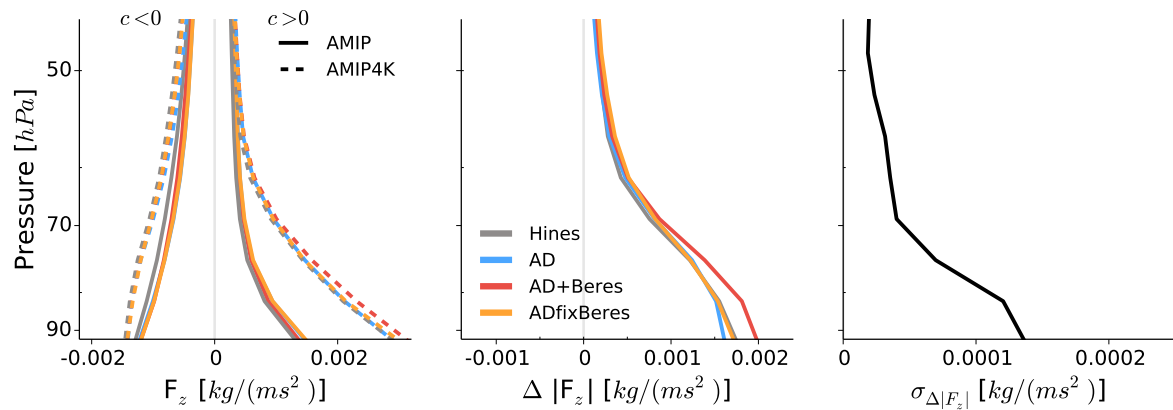


Figure 5.6: Vertical profile of vertical component F_z of the spectral EP-Flux vector for the experiments Hines, AD, AD+Beres and ADfixBeres; time (10years, based on 6 hourly data), zonal and meridional mean. F_z shows the integral over frequencies and wave numbers. Left panel: F_z of easterly ($c < 0$) and westerly ($c > 0$) waves for present day (solid) and warmer climate (dashed). Center panel: Change of the absolute value $\Delta|F_z| = |F_z|_{AMIP4K} - |F_z|_{AMIP}$ from present day climate to the warmer climate, with $|F_z| = |F_{z,c<0}| + |F_{z,c>0}|$. Right Panel: Standard deviation σ of $\Delta|F_z|$ of the four parameterization setups.

5.6. We quantify the spread of the changes in $|F_z|$ among the simulations of the different parameterization setups in the right panel of figure 5.6. The standard deviation $\sigma_{\Delta|F_z|}$ of $\Delta|F_z|$ among the different parameterization setups is an order of magnitude smaller than $\Delta|F_z|$. Therefore, the differences of $\Delta|F_z|$ between the parameterization setups are small, with $\sim 10\%$, compared to changes between present day and the warmer climate in $|F_z|$.

The change in upwelling Δw^* , due to a warmer climate, also exhibits a consistent behaviour among all parameterization setups. The profiles of the residual vertical velocity w^* of a transformed Eulerian mean analysis shows a minimum at ~ 50 hPa, increasing above and below, see left panel in figure 5.7. In the warmer climate, the profiles exhibit a general shift to higher values of w^* , while the increase in the lower stratosphere exceeds the increase at higher stratospheric levels, see center panel in figure 5.7. The standard deviation $\sigma_{\Delta w^*}$ of Δw^* among the different parameterization setups is an order of magnitude smaller than Δw^* , see right panel in figure 5.7.

Summarizing the above results, we see that the response of the resolved waves and the upwelling to a changing climate is independent of the applied gravity wave parameterization setup. The changes among the simulations of the different gravity wave parameterization setup are more than an order of magnitude smaller than the changes from present day climate to the warmer climate. This result, which we desire by the design of the experimental setup, allows to relate changes in the QBO to the different gravity wave parameterization setups.

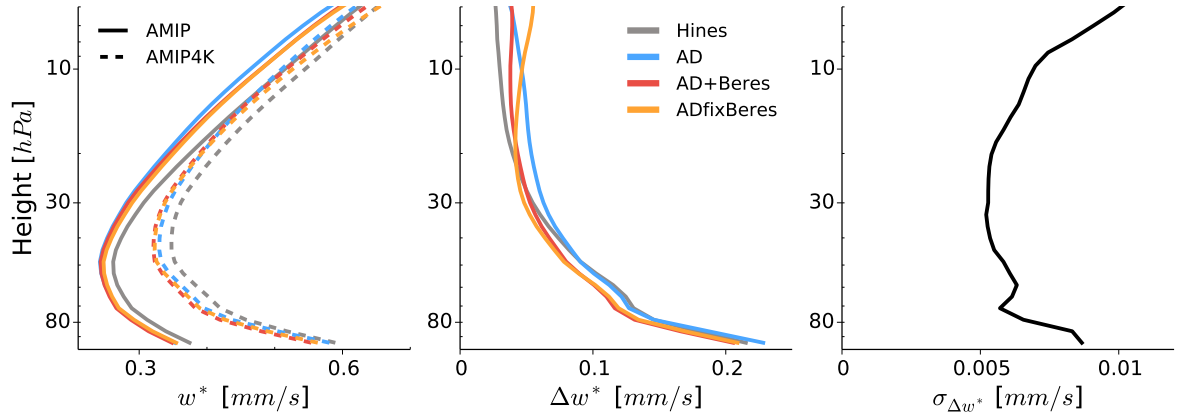


Figure 5.7: Vertical profile of residual vertical velocity w^* of a transformed Eulerian mean analysis for the experiments Hines, AD, AD+Beres and ADfixBeres; time, zonal and meridional ($\pm 25^\circ$ latitude) mean data. Left panel: w^* for present day (solid) and warmer climate (dashed). Center panel: Increase of w^* from present day climate to warmer climate, with $\Delta w^* = w^*_{AMIP4K} - w^*_{AMIP}$. Right Panel: Standard deviation σ of Δw^* of the four parameterization setups.

5.2.3 Gravity wave momentum fluxes and acceleration due to gravity waves

To complete the picture of QBO-driving mechanisms, we show the contribution of the different gravity wave parameterization setups. The gravity wave momentum flux (B) profiles reflect the differences between properties of the individual parameterization setups, see left panel in figure 5.8. AD and Hines launch gravity waves at 600 hPa in the middle troposphere, ADfixBeres launches waves at 130 hPa and AD+Beres launches gravity waves interactively at the top of the modeled convection. Therefore AD, Hines and ADfixBeres show a monotonic decrease in gravity wave momentum fluxes with height, whereas the momentum fluxes in Beres peak in the high troposphere where deep convective clouds inject large values of momentum fluxes. For a detailed distribution of momentum flux launch levels of the Beres scheme in ECHAM6 see figure 2.6.

In a warmer climate momentum fluxes B in Hines and ADfixBeres remain, as a first approximation, unchanged. This is illustrated by the small difference of solid and dashed profiles of Hines and ADfixBeres in the left panel of figure 5.8. The absolute changes $\Delta|B|$ between the warmer and the present day climate show neither a systematic increase nor a systematic decrease, but follow the zero-change line in the right panel in figure 5.8. However the parameterization setup AD shows less momentum fluxes below and within the lower QBO domain in AMIP4K. Given that the gravity wave sources in AD are constant in present day and warmer climate, a reduction in momentum fluxes in the lower stratosphere indicates stronger tropospheric wave filtering for AD in a warmer climate. The peak in the gravity wave momentum flux profile of AD+Beres shifts to higher vertical levels, following the increased vertical extent of deep convection in a warmer climate. This vertical shift of launch levels in AD+Beres leads to a relative decrease in momentum fluxes below 100 hPa and a relative increase in momentum fluxes above 100 hPa , see right panel in figure 5.8. The peak values of

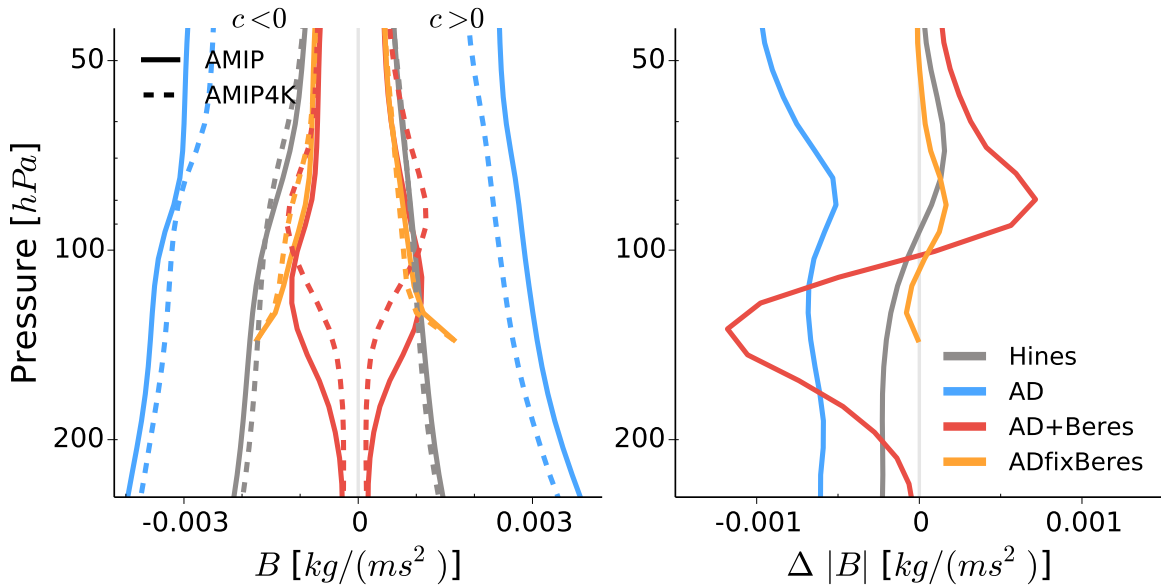


Figure 5.8: Vertical profile of gravity wave momentum flux (B) for the experiments Hines, AD, AD+Beres and ADfixBeres; time, zonal and meridional mean data. Left panel: B of easterly ($c < 0$) and westerly ($c > 0$) for present day (solid) and warmer climate (dashed). Right panel: Change of total momentum flux $\Delta|B| = |B|_{AMIP4K} - |B|_{AMIP}$, with $|B| = |B_{c<0}| + |B_{c>0}|$.

B in AD+Beres, however, remain essentially unchanged in the warmer climate.

After the momentum flux profiles of the different gravity wave parameterization setups, we present the resulting zonal wind tendency due to gravity waves ($\frac{\partial U}{\partial t}|_{GW}$). Please note, that an analysis of tendencies is only of limited informative value in this comparison of different gravity wave parameterization setups. Even though it is the tendencies, and not the momentum fluxes, that ultimately accelerates the QBO jets and drives the QBO, the tendency depends at the same time on the detailed wind profile of the modeled QBO. In both present and warmer climate, the QBOs and therefore the wind profiles that the gravity wave parameterization react to, differ among the four parameterization setups. Therefore, the tendency profiles will necessarily differ among the gravity wave parameterization setups. As a consequence we don't compare the tendency profiles of the different gravity wave parameterization setups with each other, but we focus on the relative change between present and warmer climate for each gravity wave parameterization setup individually.

We calculate the absolute amount of zonal wind tendency due to gravity waves $|\frac{\partial U}{\partial t}|_{GW}$ as the sum of the tendency of westerly gravity waves $|\frac{\partial U}{\partial t}|_{GW,c>0}$ and the tendency of easterly gravity waves $|\frac{\partial U}{\partial t}|_{GW,c<0}$. The amount of the tendency due to gravity waves $|\frac{\partial U}{\partial t}|_{GW}$, scaled by density, peaks in the lower domain of the QBO at $\sim 80\text{-}100$ hPa and decreases above, see left panel on figure 5.9. The relative change of gravity wave tendency due to the warmer climate

$$\Delta \left| \frac{\partial U}{\partial t} \right|_{GW} = \frac{|\frac{\partial U}{\partial t}|_{GW,AMIP4K} - |\frac{\partial U}{\partial t}|_{GW,AMIP}}{|\frac{\partial U}{\partial t}|_{GW,AMIP}}$$

is shown in the right panel of figure 5.9. In the warmer climate, the parameterization

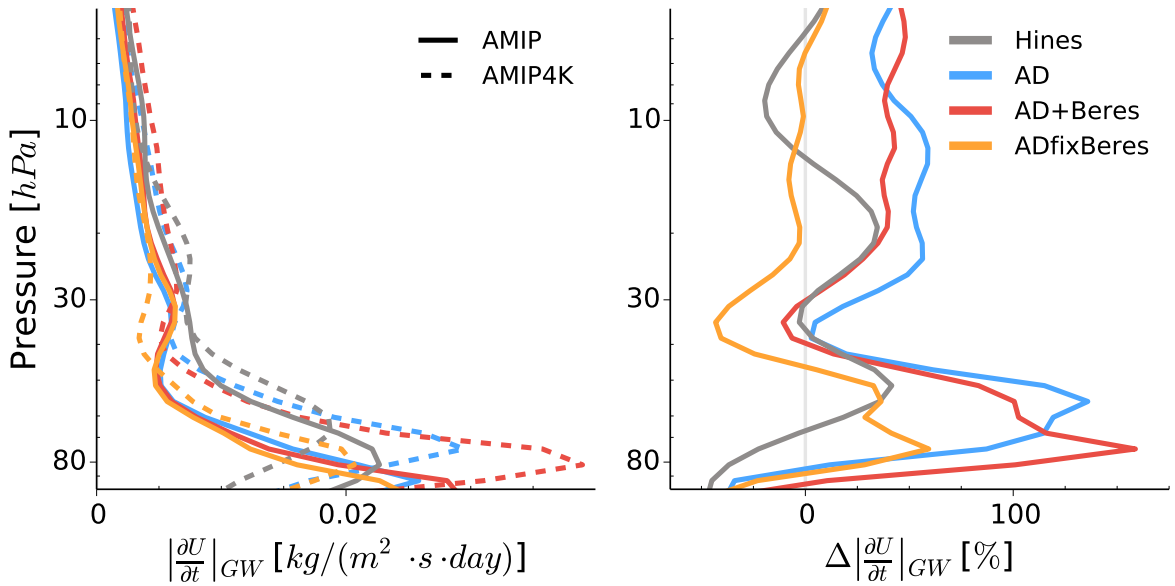


Figure 5.9: Vertical profile of zonal wind tendency due to gravity waves ($\frac{\partial U}{\partial t}|_{GW}$) for the experiments Hines, AD, AD+Beres and ADfixBeres; time, zonal and meridional mean data; $\frac{\partial U}{\partial t}$ is scaled by density ρ . Left panel: Absolute tendency due to gravity waves with $|\frac{\partial U}{\partial t}|_{GW} = |\frac{\partial U}{\partial t}|_{GW,c>0} + |\frac{\partial U}{\partial t}|_{GW,c<0}$ for present day (solid) and warmer climate (dashed). Right panel: Relative change of absolute tendency due to gravity waves $\Delta |\frac{\partial U}{\partial t}|_{GW}$.

setups ADfixBeres and Hines show both an increase and decrease of $|\frac{\partial U}{\partial t}|_{GW}$, depending on the vertical level. However AD and AD+Beres show a systematic increase in the tendency due to gravity waves in the warmer climate, with an increase of $\sim 50\%$ above 25 hPa and exceeding 100% in the lower QBO domain between 40 hPa and 80 hPa.

5.3 Summary and discussion

In this chapter we address the sensitivity of QBO changes, due to a warmer climate, to four different gravity wave parameterization setups which are summarized in table 5.1. We run atmosphere-only experiments with prescribed SSTs in both present day (AMIP) and a 4 K warmer climate (AMIP4K). The only difference in the model setups are the different gravity wave parameterizations in the tropics, while the gravity wave parameterization in the extratropics remains identical. This experimental setup minimizes the spread of future changes of the two model-intrinsic QBO driving mechanisms, the resolved waves and the upwelling, among the four parameterization setups, see figure 5.6 and 5.7. Therefore, the differences in QBO changes in a warmer climate are driven by the differences in the tropical gravity wave parameterizations. While we tune all parameterization setups individually to simulate a QBO with properties of present day climate, we analyze for each parameterization setup the response of the QBO to a warmer climate.

While both Hines and ADfixBeres show small changes in QBO period in the warmer climate, both AD and AD+Beres show a reduction in QBO period by 8 to 9 months,

see figure 5.3. In the two cases of a QBO period shortening, we observe an increase in exerted acceleration in QBO regions, see right panel in 5.8. Due to a weaker easterly jet, the QBO amplitude below 10 hPa shows a reduction in all four parameterization setups, see figure 5.5, which is consistent with results from Kawatani and Hamilton (2013). Analyzing the overall changes in QBO amplitude among the different parameterization setups, we see that Hines and AD on one hand, and AD+Beres and ADfixBeres on the other hand show a rather similar behaviour in QBO amplitude in the warmer climate.

Summarizing changes in both QBO properties, we show that changes in QBO period are not related to changes in QBO amplitude. For example, both AD and AD+Beres exhibit a reduction in QBO period, while their changes in QBO amplitude differs, except for the easterly jet below 10 hPa . Given the amplitude reduction of the easterly jet below 10 hPa , one could assume that the easterly jet descends faster in the warmer climate compared to the present day climate, because a weaker jet requires less forcing to descend. However we show in figure 5.4 that the descent duration of both the easterly and westerly jets reduce comparably in AD and AD+Beres. This result underscores the previous statement that changes in QBO amplitude are independent of changes in QBO period.

Our results show that the response of the QBO to a warmer climate is sensitive not only to the choice of the gravity wave parameterization setups, like Hines versus AD, but also to the tuning and to individual properties of the gravity wave parameterizations. Both AD and ADfixBeres use the propagation scheme after Alexander and Dunkerton, both with a fixed source spectrum. The two parameterizations setups however differ in the launch level, the spectral shape and the tuning of the propagation. The difference in properties of the gravity wave parameterization suffices to lead to no change in QBO period for ADfixBeres and a reduction in QBO period for AD. However, properties of the source spectrum or the tuning of the propagation scheme alone do not determine future QBO changes either. Both AD+Beres and ADfixBeres employ a very similar source spectrum in the future climate and identical tuning of the propagation scheme, see 5.1. Yet, the QBO period only changes for AD+Beres in the future climate.

We add a more detailed discussion on the different response of AD+Beres and ADfixBeres to the warmer climate. The experimental setup AD+Beres is the only setup which considers changes in the gravity wave sources due to a warmer climate, while ADfixBeres uses the diagnosed AD+Beres source spectrum of present day climate in both the present and warmer climate. The substantial differences in QBO period changes between these two experimental setups highlights the impact of a physically based and therefore changing gravity wave source parameterization. We discuss possible reasons for the differences between AD+Beres and ADfixBeres. The source spectrum in AD+Beres increases slightly in the warmer climate, see figure 5.1, but the overall amount of excited momentum flux at the source level does not increase substantially, indicated by the similar peak values for AD+Beres for present and warmer climate in the left panel of figure 5.8. However, due to a deeper vertical extent of convection in the warmer climate, the launching height of the peak source momentum flux in AD+Beres increases by roughly 20 hPa , see the left panel of figure 5.8. A higher launch level entails less wave filtering and more available momentum flux that drives the QBO. We do not identify a clear reason for the difference between AD+Beres and ADfixBeres, but

we speculate that the changes in launch level in AD+Beres partly cause the changes between the two experimental setups.

On one hand, neither Hines nor ADfixBeres show a change in QBO period in a warmer climate or show a change in exerted acceleration on the QBO. Therefore we conclude that, in these two cases, the increased forcing of resolved waves is balanced by the increased upwelling, which counteracts wave forcing.

On the other hand, both AD and AD+Beres show a decrease in QBO period in a warmer climate. In the case of AD+Beres, the total amount of emanating momentum flux does not increase substantially, see figure 5.1 and left panel in figure 5.8, but the mean launching height of gravity waves increases in the warmer climate. In the case of AD, the amount of momentum flux below the QBO domain decreases in the warmer climate. The decrease in gravity wave momentum flux opposes the assumed increase in wind tendency due to gravity waves, as expected from a shorter QBO period in the warmer climate. In the warmer climate, however, both AD and AD+Beres do exert more acceleration in QBO regions than in present day climate, see right panel in figure 5.9. Since the QBO period decreases for AD and AD+Beres, we conclude that the increase in resolved wave forcing and the increase in exerted gravity wave acceleration outweighs the increase in upwelling.

Chapter 6

Conclusions

In this work, we improve the representation of convection based gravity wave (gravity wave) sources in the atmospheric GCM ECHAM6. Since convection is present on nearly all latitudes, ECHAM6 benefits from the new gravity wave parameterizations in the tropics and mid-latitudes. In this thesis we focus on the excitation of equatorial gravity waves which drive the stratospheric quasi-biennial oscillation (QBO). We analyze the effect of a convection based gravity wave parameterization on the QBO on seasonal, interannual and climatological timescales, asking: (I) Does the seasonal cycle in the physically based gravity waves improve QBO quantities on the seasonal timescale? (II) How does the interannual variability of wave activity associated with El Niño / Southern Oscillation project on the QBO? (III) How does a physically based gravity wave parameterization compare to other gravity wave parameterizations with fixed gravity wave sources in driving the QBO in a warmer climate? After summarizing the presented results, we draw conclusions and we discuss and evaluate different domains of QBO- and gravity wave-related research for the future, based on the answers of the above questions.

Technical implementation and the link to the sources

Due to the physical link to convection in the gravity wave parameterization, the excited gravity waves show spatial and temporal variability. Furthermore, instead of prescribing spectral characteristics of gravity waves, these gravity wave properties depend on the background wind and the heating properties of the convection. The gravity wave properties are particularly sensitive to the vertical extend of convective heating and the amount of heating, which are determined by the convection parameterization. Since the parameterized heating properties differ from observations, the gravity wave source parameterization inherits possible deficiencies of the convection parameterization. This highlights the importance of a good representation of convective processes in GCMs not only for convection itself, but also for processes depending on convection, like the excitation of gravity waves.

While the employed model version uses a physically based gravity wave parameterization in the tropics, based on convection, gravity wave sources in the extratropics remain constant and prescribed. In order to further advance the representation of

gravity waves on the entire globe (Richter et al., 2010), one could consider the gravity wave parameterization based on frontal system following Charron and Manzini (2002) for future experimental setups which focus not only on the tropics.

Not only the chosen experimental setup, but also the Beres parameterization itself allows further improvement. The implemented version of the Beres parameterization does not include the “obstacle effect” which generates stationary waves similar to gravity waves forced by orography. When trying to include the formulation for the effect of stationary waves into the present gravity wave source parameterization, we explored a mistake in the theoretical derivation of Beres (2004). Revisiting the theoretical derivation and solving the equation for stationary waves, with $c = 0$ m/s, is necessary in order to further improve the Beres gravity wave source parameterization.

Improvements on the QBO

Compared to the QBO simulated with the previously employed gravity wave parameterization with constant sources, the physically based gravity wave parameterizations produces a QBO with improvements on the QBO amplitude. Furthermore, the QBO simulated with temporally varying gravity wave sources suggests an improvement on the seasonal timescale. Due to the physically based gravity wave sources, the downward propagation rate of the QBO jets is modeled more realistically, closer to observations.

While the shape, the asymmetries, the launching height, the temporal, and the spatial variability of the gravity wave source spectrum remain entirely based on physical quantities, the gravity wave parameterization still requires tuning. The total amount of excited momentum flux and the breaking levels of the propagation parameterization are important factors to produce a QBO in the chosen model setup. The physically based nature of a parameterization does not entirely remove the subjectiveness of choosing tuning parameters. However the convection based gravity wave parameterization reduces the degrees of freedom in the space of tuning parameters, because the shape of the source spectrum and the launching height are now interactively determined by the parameterization - instead of being subjectively determined.

How ENSO modulates the QBO

We show that the interannual variability of wave activity associated with ENSO modulates QBO properties. Comparing El Niño (EL) to La Niña (LA) conditions, changes in QBO properties are driven by QBO forcings of primarily parameterized waves and secondarily resolved waves, while changes in upwelling do not contribute substantially. We explain the different behaviour in downward propagation speed of the QBO jets in QBOE and QBOW by considering two QBO mechanisms. First, an increase in wave forcing and, second, a weaker underlying jet both favor a faster downward propagation speed of a QBO jet. During El Niño, wave activity increases for both QBOE and QBOW and affects the jets in a very similar way at the onset of the ENSO signal. In QBOW, the underlying easterly jet is weaker during El Niño, while in QBOE the underlying westerly jet is stronger during El Niño. In QBOW, both the increase in QBO wave forcing and the weaker underlying easterly jet favor a faster downward

propagation of the westerly jet. In QBOE however, the increase in QBO wave forcing is balanced by the stronger underlying westerly, so that the downward propagation speed under El Niño and La Niña conditions remains unchanged.

Despite the consistent and physically solid argument that considers the effect of the underlying jet on the downward propagation speed, we are not able to explain why the strength of the underlying jet behaves differently for QBOE and QBOW. A reason or hypothesis for the change in QBO amplitude appears challenging to identify - due to the strong coupling between individual QBO forcings in this case. Additionally the strong feedbacks between changes in QBO forcing, changes in QBO amplitude and changes in QBO downward progression in a complex GCM impede a logical chain of argumentation or reasoning. Following up on this thought see below the outlook for future research on this topic, including suggestions how to disentangle the QBO feedbacks and advance the physical understanding of the QBO mechanisms.

Sensitivity of the QBO in a warmer climate to different gravity wave parameterizations

We show that the choice of the gravity wave parameterization setup determines the QBO period in a warmer climate. Even though we diagnose an increased acceleration due to gravity waves in those gravity wave parameterization setups that show a shortening of the QBO period, we are not able to explain why certain gravity wave parameterization setups change specific QBO properties. However we can state the differences in the experimental setup of gravity wave parameterizations that lead to changes in QBO properties. Results of this work suggest that changes in QBO properties in a warmer climate do not only depend on the gravity wave scheme, but also on source spectrum properties like the launch level, the spectral shape, the physical link to the sources, and the tuning of the propagation scheme. Small changes in any of the mentioned properties can lead to pronounced changes in QBO properties in a warmer climate. In a warmer climate, QBO properties and in particular the QBO period are highly sensitive to the employed gravity wave parameterization, its detailed setup and its tuning. Therefore the different gravity wave parameterizations employed in CMIP5 models may explain the spread of simulated QBO period changes in different CMIP5 models. Of the four different gravity wave parameterization setups employed in our study, the physically based gravity wave parameterization setup simulates a QBO reduction by 9 months in a 4 K warmer climate.

Combining the last two sections, we compare the response of the QBO to the forcing of ENSO and of a warmer climate. In both cases, the climate system is forced by warmer SSTs, with a peak of 1.5 K increase between El Niño and La Niña conditions and 4 K increase in the warmer climate. Focusing on the gravity wave parameterization with physically based gravity wave sources, we compare the response of the QBO period to increased SSTs in both cases. Combining the response of QBOE and QBOW to the warmer El Niño conditions, the QBO period shortens during El Niño conditions. This response is consistent with the QBO period reduction that AD+Beres experience in a warmer climate. The short simulation time in the ENSO experiments does not

provide any statistical statement on the QBO amplitude and therefore does not allow a comparison with changes in QBO amplitude of the climate run.

We finalize this chapter by abstracting our results and putting our findings into the greater picture of more general earth system models. In a warmer climate, we explore the response of a phenomenon, the QBO, focusing on the sensitivity to the parameterization that partly drives the phenomenon. We find that the response of the phenomenon to a warmer climate depends on the choice of the gravity wave parameterization and/or the tuning of the parameterization. Depending on the choice or the tuning of the gravity wave parameterization, we can therefore determine the future behaviour of the phenomenon simulated in a GCM. In a thought experiment, we can extend this result from a single phenomenon in the stratosphere to any process or physical quantity in the earth system that depend directly on parameterizations: Cloud cover, convection, rain formation, sub-grid turbulence, moisture and heat exchange at the surface. More generally also the large scale circulations, internal variability and climate sensitivity depend, indirectly, on parameterized processes. We can tune each process or phenomenon in present day climate, but how confident are we about the changes to forcings? Is the simulated response of a GCM to an external forcing, like a warmer climate, a robust feature or solely dependent on the choice and the tuning of the parameterization? Can we obtain, depending on the tuning or the choice of a parameterizations in a GCM, different answers to the same question? Or formulated differently in an extreme case, does a quantity like climate sensitivity depend on parameterizations and can we therefore tune the future climate (Stainforth et al., 2005; Bender, 2008; Klocke et al., 2011; Mauritsen et al., 2012)?

In order to answer those question, we need to focus on understanding physical processes along with testing hypothesis and explaining the response of the earth system to a specific forcing. Only after we understand the response of a physical process or phenomenon to a forcing, we are able to asses its robustness and we are able to separate the noise due to the choice of the parameterization from the robust signal. In the next chapter, we also suggest how to advance the physical understanding of the QBO.

6.1 Concluding remarks and outlook

In this thesis we analyze the response of one of climate's important dynamical phenomenon, the QBO, to changes in tropospheric forcings on different timescales. In chapter 3 we identify a clear reasoning for changes in QBO properties: Due to the implementation of physically based gravity wave sources and the consequently resolved seasonal cycle in gravity wave forcing, the model simulates the seasonality in QBO downward propagation more realistically. We are able to explain the results in this case, because only one of the three QBO forcing mechanisms changes. While the resolved waves and the upwelling remain constant, we improve the representation of gravity waves whose improvement projects on the QBO. In exploration of two other phenomena on longer timescales, ENSO in chapter 4 and the warmer climate in chapter 5, all three QBO forcing mechanisms change simultaneously. The QBO responds to all forcing mechanisms at the same time, including feedbacks between individual

QBO forcings, the QBO amplitude and the QBO downward propagation. The strong feedbacks between QBO forcings and QBO properties strongly hinders to establish a direct relation between changes in QBO forcing and changes in QBO properties, see also the discussion in chapter 4.4. More generally, the non trivial problem of disentangling forcings and feedbacks is not unique to QBO dynamics, but applies to many processes in earth system science.

We present three suggestions for future work on large scale waves, gravity waves and wave - mean flow interactions in the context of the QBO and the related QBO forcings. Regarding the QBO mechanism, we think that only the third suggestions ultimately helps in disentangling the feedbacks acting on the QBO and in separating changes in QBO amplitude from changes in QBO period.

1. Observations

Observations of tropical waves can improve on horizontal, vertical and temporal scales. Better observations of waves in the lower stratosphere would better constrain the tuning, see chapter 3.2, and properties of gravity wave parameterizations, see chapter 2.2, as well as the benchmarking of resolved waves of GCMs. Observations therefore should include the entire range of waves, from small scale gravity waves, intermediate gravity waves, mixed Rossby-gravity waves to Kelvin waves. Given the lack of detailed observations, the observed total amount of gravity waves in the lower stratosphere ranges between 1 *mPa* and 5 *mPa* (Sato and Dunkerton, 1997; Piani et al., 2000; Grimsdell et al., 2010; Geller et al., 2013). Within that large observational range, gravity wave parameterizations can be employed to compensate for deficiencies in the resolved waves of GCMs. However, compensating deficiencies in the representation of resolved waves should not be the role of gravity wave parameterizations in GCMs.

The tuning of gravity wave parameterizations would benefit from better observational data in several aspects. First, a better estimate of the total amount of gravity waves entering the stratosphere narrows down the present broad observational range of 1 *mPa* to 5 *mPa*. Second, a separation of the total amount of gravity waves into easterly and westerly waves would help to identify asymmetries in gravity wave source spectra. Third, observations and numerical simulations with cloud resolving models are used to derive detailed gravity wave source spectra only for single, localized events, see the exemplary figure 1.3 in chapter 1.2. However gravity wave source parameterizations require an estimate of detailed gravity wave source spectra on a global scale. Evan et al. (2012) show a first attempt to provide such information by running the WRF model with 40 *km* horizontal resolution in an equatorial global channel for selected single months. Inspired by Jewtoukoff et al. (2013), a comprehensive measuring campaign with balloons on constant pressure surfaces in the lower stratosphere is envisaged to start in 2017/2018, which addresses some of the shortcomings of present day observations.

2. High resolution models

The use of high resolution models, that resolve a sufficient amount of waves, reduces the necessity of gravity wave parameterizations. Within the realm of MPI, a high resolution version of an atmospheric GCM, such as the icosahedral non-hydrostatic general circulation model ICON, would provide a promising testbed for providing and analyzing resolved wave spectra. Furthermore a GCM with high resolution allows to advance our understanding of wave - mean flow interactions without the need of a gravity wave parameterization. Finally such a model can be used to test hypothesis developed with conceptual models, see further below. Until models with sufficient resolution become the standard of state-of-the-art GCMs, a physically based gravity wave parameterization like AD+Beres remains the most realistic approach considering the effect of gravity waves in a GCM.

Note that increasing resolution can, but will not necessarily, improve the representation of resolved waves or of parameterized gravity waves. Changing resolution requires a re-tuning of the convection parameterization, which will project directly on the representation of resolved waves and also on the representation of convection based gravity waves, see chapter 2.2.3. Increasing resolution to an extent which approaches the “gray zone“, the domain where parts of the convective parameterization are resolved, introduces non-trivial issues for the role of parameterizations in GCMs.

However increasing resolution to a degree which allows to omit the convection parameterization entirely is alluring. Such a high resolution setup removes the disadvantages of the convection parameterization because the convective processes are resolved. A global LES-type simulation along the equator in the tropics would provide resolved, unique wave spectra of unprecedented detail and spatial coverage. Following this approach in the future within MPI, we suggest to setup a nested version of ICON with cloud resolving resolution in the tropics and lower resolution in the extratropics.

We conclude that while increasing model resolution yields attractive and novel possibilities, this approach does not consequently lead to an ad hoc improvement of the convection parameterization and therefore the representation of waves driving the QBO. Pursuing the approach of high resolution modeling, we propose to critically evaluate first the representation of convection in such a model before analyzing wave spectra or wave-driven phenomena in the stratosphere.

3. Conceptual model

While both better observations and high resolution modeling will help constrain gravity wave parameterizations, provide a benchmark for resolved wave properties and help understand QBO mechanisms to a certain degree, the two approaches will not help in disentangling the complex feedbacks acting on the QBO. Continuing research with GCMs to understand QBO feedbacks is limited, because we can't apply a classic feedback analysis for the QBO in GCMs. Following a classical approach in feedback analysis, one would keep two QBO forcing mechanisms constant and only perturb the single, remaining forcing mechanisms. This approach would allow to diagnose the linear response of the QBO to a specific forcing, see Hansen et al. (1984); Gregory

et al. (2004). Having applied this diagnostic to all QBO forcings individually, the approach aims at identifying the sensitivity of individual QBO forcings and allows to compare the different QBO forcings in a linear framework. However we can't apply this classical approach in the case of the QBO because in a GCM, the resolved waves, the upwelling and secondary circulation of the QBO are model-intrinsic QBO forcings which we can't artificially disable or hold constant in a GCM. The same applies to 2D models like Plumb and Bell (1982), in which the secondary circulation develops intrinsically in the model. Therefore we propose to employ a conceptual, simple 1D model as introduced in chapter 1.1.2.

Historically, work on conceptual models ends in the late 90s of the last century at a time when the first GCMs successfully started simulating QBOs or producing QBO-like oscillations. About 20 years of QBO research with GCMs produced tremendous knowledge and advanced the understanding of the QBO fundamentally. However in GCMs, we find considerable uncertainties and alarming sensitivity to tuning parameters in a highly complex model, see chapter 5. Due to the complex physical processes and feedbacks acting on the QBO, see chapter 4 and 5, we think that QBO research would benefit from revisiting conceptual models. Rather than increasing model resolution, we suggest that a conceptual model allows to disentangle QBO forcings, acting simultaneously in a GCM or 2D model, and allows to systematically analyze and determine QBO feedbacks. We further envisage that conceptual models help in separating changes in QBO period from changes in QBO amplitude. Performing sensitivity experiments with a gravity wave parameterization, Scaife et al. (2000) identify the tuning parameters which govern the QBO amplitude on one hand and which govern the QBO period on the other hand. We plan to extend this work of the effect of a single gravity wave parameterization to the remaining QBO forcings including more general waves, the upwelling and the secondary circulation.

See the appendix for more details on the conceptual 1D model and first steps in the development of a new, more comprehensive model that considers all QBO mechanisms. We think that this improved conceptual basis is crucial and should be considered a necessity - along improved observations and a more detailed analysis of wave spectra and wave-mean flow interactions in high resolution models - to advance the physical understanding of QBO dynamics.

Appendix

1D model of the QBO

Since GCMs and 2D models inherently include QBO mechanisms like the secondary circulation, we choose a 1D model to apply a thorough feedback and sensitivity analysis. However, the existing 1D model of the QBO lacks the effect of the secondary circulation $SC(u)$, see equation 1.2 in the introduction 1.1.2

$$\overline{u_t} = -\frac{F_z}{\bar{\rho}} + \frac{\nu}{\bar{\rho}}(\overline{\rho u_z})_z - \overline{w} \cdot \overline{u_z} + SC.$$

Dunkerton (1997) present a formulation for $SC(u)$ combining the effect of upwelling due to the Brewer-Dobson circulation $\overline{w_{BD}}$ with the vertical component of the secondary circulation as a function of the vertical shear $\overline{u_z}$ which yields

$$\begin{aligned} \overline{u_t} &= -\frac{F_z}{\bar{\rho}} + \frac{\nu}{\bar{\rho}}(\overline{\rho u_z})_z - \overline{w} \cdot \overline{u_z} \\ \overline{w} &= \overline{w_{BD}} + \alpha \cdot \overline{u_z} \end{aligned} \quad (1)$$

with a regression coefficient α . However this approach only considers the vertical component of the secondary circulation, omitting the effects of the horizontal component which we need to include to consider the full effect of the secondary circulation. The formulation 1 is the starting point for determining a formulation including both the vertical and the horizontal component of the secondary circulation. In detail, we plan to analyze reanalysis products such as ERA-Interim to diagnose the effect of the SC on the QBO. We choose reanalysis products over conventional climate model simulations, because the QBO amplitude strongly alters the effect of the SC and the QBO amplitude in reanalysis products is closer to reality. Aiming to exclude the effect of the Brewer-Dobson circulation on the vertical and horizontal component of advection, we suggest to remove the seasonal cycle in the reanalysis product. Using this data product, we regress the zonal wind tendency due to horizontal and vertical advection with the vertical wind shear, yielding regression coefficients. Finally this will give

$$\overline{u_t} = -\frac{F_z}{\bar{\rho}} + \frac{\nu}{\bar{\rho}}(\overline{\rho u_z})_z - \overline{w_{BD}} \cdot \overline{u_z} + \beta_h \cdot \overline{u_z} + \beta_v \cdot \overline{u_z}.$$

with the regression coefficients β_h and β_v for the effect of the horizontal and vertical component of the SC.

Once a physically correct formulation for SC is found, we are able to disentangle the effect of individual QBO forcing. Additionally we envisage to disentangle the effect of changes in the QBO amplitude from changes in the QBO propagation speed. This approach might help to identify which physical mechanisms controls the QBO amplitude and which mechanisms controls the QBO propagation speed.

Symbols

B_0	Gravity wave source momentum flux [m^2/s^2]
B	Gravity wave source momentum flux scaled by density [Pa] = [$kg/(m \cdot s^2)$]
$ B $	Total amount of gravity wave source momentum flux scaled by density
B_{max}	Maximum momentum flux amplitude
β_h	Regression coefficient for horizontal component of SC
β_v	Regression coefficient for vertical component of SC
c	Horizontal phase speed
c_{max}	Peak horizontal phase speed
C_F	Fraction of convection within GCM gridbox
ϵ	Intermittency factor
EOF	Empirical Orthogonal Function
F	Wave momentum flux
F_z	Vertical component of the Eliassen-Palm flux vector
$ F_z $	Amount of total $ F_z = F_{z,c<0} + F_{z,c>0} $
F_y	Meridional component of the Eliassen-Palm flux vector
H_b	Cloud base
H_q	Convective heating depth
H_t	Cloud top
L	Spatial averaging domain
λ_h	Horizontal wavelength
ν	Kinematic viscosity
pc	Principal components of the EOF analysis
Φ	Latitude
ϕ	Angular component of polar coordinate
$ \psi $	Radial component of polar coordinate
Q_0	Vertical mean heating rate
Q_{max}	Peak heating rate within GCM gridbox
σ	Standard deviation
σ_x	Horizontal extent of convective cell
ρ	Density
ρ_0	Density at cloud top
$\frac{\partial U}{\partial t} _{GW}$	Gravity wave drag
$\frac{\partial U}{\partial t} _{\nabla \cdot EP}$	Drag due to resolved waves
$\frac{\partial U}{\partial t} _{ADV}$	Drag due to advection
$\frac{\partial U}{\partial t} _{Total}$	Total drag
$\langle \frac{\partial U}{\partial z} \rangle$	Wind shear within convective heating
u_{rms}	Parameter for source strength in Hines parameterization
u_{700}	Horizontal wind speed at 700 hPa
w^*	Vertical velocity of the transformed Eulerian Mean analysis

Acronyms

AD	Alexander and Dunkerton GW propagation parameterization
AD+Beres	Beres GW source parameterization coupled to AD
ADfixBeres	AD with fixed GW source spectrum obtained by Beres
AMIP	Atmospheric Model Intercomparison Project
AMIP4K	SSTs from AMIP homogeneously increased by 4 <i>K</i>
GW	Gravity Wave
ECHAM6	Version 6 of the atmospheric general circulation model ECHAM developed at MPI
ECHAM6-Beres	ECHAM6 with Beres GW parameterization
ECHAM6-Hines	ECHAM6 with Hines GW parameterization
ECMWF	European Center for Medium-range Weather Forecast
EL	El Niño
ENSO	El Niño / Southern Oscillation
EOF	Empirical Orthogonal Function
EP	Eliasson-Palm
ERA-Interim	Reanalysis product developed by ECMWF
GPCP	Global Precipitation Climatology Project
Hines	Hines GW parameterization
ICON	Icosahedral non-hydrostatic general circulation model
LA	La Niña
MIROC	Model for Interdisciplinary Research on Climate
MPI	Max Planck Institute
MPI-ESM	Max Planck Institute Earth System Model
MSU	Microwave Sounding Unit
NCEP	Reanalysis product developed by the National Center for Environmental Prediction
QBO	Quasi-Biennial Oscillation
QBOE	QBO with the onset of the easterly jet at 10hPa
QBOW	QBO with the onset of the westerly jet at 10hPa
SAO	Semi-Annual Oscillation
SC	Secondary Circulation of the QBO
SIC	Sea Ice Concentration
SST	Sea Surface Temperature
TEM	Transformed Eulerian Mean
TRMM	Tropical Rainfall Measurement Mission
WRF	Weather Research and Forecasting model

Abstract (English)

In order to simulate stratospheric phenomena such as the Quasi-Biennial Oscillation (QBO) of equatorial zonal winds, atmospheric general circulation models (GCM) require parameterizations of unresolved, small scale gravity waves (GW). In the tropics the main source of GWs is convection, showing high spatial and temporal variability in occurrence and strength. However many GCMs employ GW parameterizations with constant and prescribed GW sources. In this work we implement in the GCM ECHAM6 a source parameterization for GWs forced by convection. The GW source parameterization is based on the convective heating depth, convective heating rate and the background wind. We show that the heating depth distribution of convective properties strongly influences the waves' source spectra, which highlights the widespread importance of a realistic parameterization of convective processes in a GCM.

With the convection based GW scheme as the unique source of GWs in the tropics, the GCM ECHAM6 simulates a QBO with realistic features. In this thesis we analyze the effect of a more physical, convection based GW parameterization on the QBO on seasonal, interannual and climatological timescales. Due to the seasonality of the physically-based gravity wave sources, the seasonality of the QBO jets downward propagation is modeled more realistically. Furthermore, the wind speeds of the jet maxima and the variance of wind alteration show a clear improvement.

In an idealized experimental setup, we show that El Niño / Southern Oscillation (ENSO) modulates QBO properties on the interannual timescale. Comparing experiments with El Niño (EL) and La Niña (LA) boundary conditions, we show that the increased wave activity during EL increases both resolved wave and parameterized GW forcings on the QBO. The increase in wave forcing, dominated by the GWs, leads to a faster downward propagation speed of the westerly jet during EL compared to LA.

Finally we explore how different GW parameterization setups determine the response of QBO properties to a warmer climate. Atmosphere-only experiments in both present day and warmer climate serve as testbed to analyze the effect of four different GW parameterization setups, active in the tropics. Having tuned the GW parameterizations to produce a realistic QBO in present day climate, we analyze changes of QBO properties in the warmer climate. The QBO period decreases in two parameterization setups by $\sim 30\%$, while the QBO period remains unchanged in the remaining two parameterization setups. In the chosen experimental design, the inconsistent future change in QBO period among the suite of experiments depends solely on the choice of the GW parameterization setup.

In the future, research on GWs and the QBO should focus on three aspects, ideally considered in a combined effort. First, better observations help to constrain the tuning of GW parameterizations, to evaluate parameterized GW source spectra and to benchmark the resolved waves. Second, high resolution models reduce the need to parameterize GWs and constitute a tool to increase the understanding of wave - mean flow interactions. Third, conceptual low dimensional models are needed to advance the understanding of QBO mechanisms. This approach helps to disentangle individual

QBO forcing mechanisms, reduces the QBO feedbacks and allows to separate effects of the QBO amplitude from effects of the QBO downward propagation.

Abstract (German)

Um stratosphärische Phänomene wie die quasi-zweijährige Oszillation (QBO) der äquatorialen Zonalwinde zu simulieren benötigen atmosphärische allgemeine Zirkulationsmodelle (GCM) Parametrisierungen von unaufgelösten, kleinskaligen Schwerewellen (SW). In den Tropen stellt Konvektion die größte Quelle von SW dar und Konvektion variiert räumlich und zeitlich stark im Auftreten und in der Stärke. Jedoch kommen in vielen GCMs Parametrisierungen von SW mit konstanten und vorgeschriebenen Quellen zum Einsatz. In dieser Arbeit implementieren wir in das GCM ECHAM6 eine Parametrisierung für Quellen von Schwerewellen, welche an die Konvektion gekoppelt sind. Die Parametrisierung von SW Quellen basiert auf der vertikalen Erstreckung der konvektiven Heizraten, der Amplitude der konvektiven Heizraten und dem Hintergrundwind. Die starke Abhängigkeit der spektralen Eigenschaften der SW von der Konvektion zeigt sehr deutlich wie wichtig eine realistische Parametrisierung der konvektiven Prozesse in einem GCM ist.

Mit einem auf der Konvektion basierten SW Schema als einzige Quelle von SW in den Tropen simuliert das GCM ECHAM6 eine QBO mit realistischen Eigenschaften. In dieser Arbeit analysieren wir die Wirkung von einer physikalischeren, auf Konvektion basierten Parametrisierung von SW auf die QBO auf saisonaler, mehrjähriger und klimatologischer Zeitskala. Aufgrund der Saisonalität von physikalisch basierten Quellen von SW wird die Saisonalität des Absinkens der QBO Jets realistischer modelliert.

Des Weiteren zeigt die Windstärke der Jetmaxima und die Varianz der Windänderungen eine klare Verbesserung. In einem idealisierten Experimentaufbau zeigen wir, dass El Niño / Südliche Oszillation (ENSO) Eigenschaften der QBO verändert. Indem wir Experimente mit Randwerten von El Niño (EL) und La Niña (LA) vergleichen zeigen wir, dass eine Zunahme der Wellenaktivität während EL zu einer Zunahme sowohl der aufgelösten Wellen als auch der parametrisierten SW führt. Die Zunahme der Wellenaktivität, welche von den SW dominiert wird, führt zu einem schnelleren Absinken des westlichen QBO Jets in EL, verglichen mit LA.

Schließlich untersuchen wir wie verschiedene Setups von SW Parametrisierungen die Reaktion von Eigenschaften der QBO auf ein wärmeres Klima bestimmen. Nur-atmosphärische Experimente in einem heutigen und einem wärmeren Klima dienen als Testumgebung um den Effekt von vier verschiedenen Setups von SW Parametrisierungen, die in den Tropen aktiv sind, zu analysieren. Nachdem wir die SW Parametrisierung eingestellt haben um eine realistische QBO im aktuellen Klima zu erhalten, analysieren wir die Änderung der QBO Eigenschaften im wärmeren Klima. Die Periode der QBO verlangsamt sich in zwei Setups von SW Parametrisierungen um $\sim 30\%$, während die QBO Periode in den anderen beiden Setups unverändert bleibt. In dem gewählten Experimentaufbau hängt die inkonsistente Veränderung der QBO Periode in der Zukunft innerhalb den verschiedenen Experimenten allein von der Wahl des Setups der SW Parametrisierung ab.

In der Zukunft sollte die Forschung von SW und der QBO den Fokus auf drei Aspekte lenken, die idealerweise in einem übergreifendem Ansatz bewältigt werden. Erstens helfen bessere Beobachtungen beim Einstellen von SW Parametrisierungen,

beim Bewerten von parametrisierten Quellspektren von SW und beim Bewerten der aufgelösten Wellen. Zweitens reduzieren hoch aufgelöste Modelle die Notwendigkeit SW zu parametrisieren und stellen ein Werkzeug dar um das Verständniss der Interaktion von Wellen mit der Hintergrundbewegung zu erweitern. Drittens werden konzeptionelle Modelle benötigt um das Verständniss von QBO Mechanismen voranzubringen. Dieser Ansatz hilft die individuellen QBO Antriebsmechanismen zu entkoppeln, die Rückkopplungen zu reduzieren und erlaubt die Effekte der QBO Amplitude von Effekten des Absinkens der QBO zu trennen.

Acknowledgements

I give sincere thanks to Elisa Manzini for her initial ideas for this thesis, scientific input, fruitful and long discussions, her open door and the supervision of this thesis. I especially appreciate her continuous support even though the thesis ended having a different focus than initially anticipated.

I thank Bjorn Stevens for being my panel chair and for giving advice on the chosen path of research during this thesis. I also thank Marco Giorgetta for being part of my advisory panel board and for his scientific input on this work. For my 4-week stay in Boulder, I'd like to thank Joan Alexander for hosting me at NWRA and providing theoretical and practical advice on the implementation of the gravity wave source parameterization and the gravity wave propagation parameterization into ECHAM6.

I enjoyed the helpful and productive discussions with Thomas Krismer and would like to thank him for his continuous scientific support and ample discussions on QBO dynamics and mechanisms. Without his support and QBO knowledge, I would have not been able to cover the range of topics covered in this thesis within less than three years of conducted research.

I would like to thank the IMPRS-ESM which supported me administratively so that I could focus on conducting research throughout the last three years. Including my bachelor and diploma thesis, I nearly spent 5 years at the MPI-M. I would like to thank all members of the atmosphere department for the friendly, cooperative and inspiring atmosphere during this time.

I thank Thomas Krismer, Louise Nuijens and Thomas Keitzl for proofreading parts of this thesis and for providing me comments and valuable suggestions on refining this thesis.

Special thanks belong to my family and friends who supported me throughout the last years.

Sebastian Schirber
Hamburg, November 4, 2014

List of Figures

- 1.1 The QBO in ERA Interim. Timeseries of meridional (5°N to 5°S lat) and zonal mean zonal wind U in the stratosphere. 3
- 1.2 The QBO mechanism. Schematic representation of the temporal evolution (a-d) of QBO jets (solid line), driven by vertically propagating waves (curved arrows). Vertical axis depicts height, horizontal axis depicts zonal wind and horizontal phase speed. Double arrows illustrate wave-driven acceleration of the QBO jets, single arrows depict acceleration due to viscosity. Waves break where their horizontal phase speed c is close to the value of the QBO jets, the background wind. Illustration from Plumb (1984); Baldwin et al. (2001). . . . 4
- 1.3 gravity waves excited by a squall-line modeled with a 2D cloud resolving model. Background colors show temperature perturbations of gravity waves in K and the white contour shows the location of the convective heating in the troposphere. The horizontal axis shows the horizontal extent in km , the vertical axis height in km . Figure adopted from Alexander and Barnet (2007). . . . 9
- 2.1 Illustration of the setup of gravity wave parameterizations. The *Lott & Miller* scheme parameterizes orographic gravity waves and the *Hines* schemes covers frontal system and more general instabilities (orange). The implemented, convectively based *Beres* gravity wave source parameterization is coupled to the gravity wave propagation parameterization *AD* (blue). While the *Lott & Miller* and the *Beres + AD* schemes include the link to physical sources, *Hines* launches gravity waves independent of the physical background state. The illustration does not account for the schemes' spatial distribution of gravity wave activity. 15
- 2.2 Source spectrum B of zonal momentum flux and its seasonal variability. (a) Latitudinal distribution of time and zonal mean source momentum flux as a function of phase speed. The dashed black line shows the zonal mean wind at 700hPa, the basis for the Doppler shift of the spectrum. (b) Zonal and meridional (5°N to 5°S lat) mean source spectra of zonal momentum flux in the four seasons. (c) Annual cycle of total zonal momentum flux B , zonal and meridional (5°N to 5°S lat) mean integrated over phase speed. All time averages cover 30 years (a-c). 18

2.3	Effect of the background wind on the source spectrum, shown for two selected regions, centered over Indonesia (60° - 160° lon) (a,b) and over South America (280° - 340° lon) (c,d). Colors illustrate different regimes of heating depth: contribution from shallow heating depths (2.5 - 10 km, orange) and from deep heating depths (10 - 18 km, blue) to the entire range (2.5 - 18 km, black). Zonal, meridional (5° N to 5° S lat) and time (5 years) mean source spectra of zonal momentum flux (a,c). The spectral asymmetry is caused by wind shear, approximated as the mean wind relative to the zonal wind at 700 hPa ΔU , within the vertical extent of the heating. The histogram of ΔU is shown for different regimes of cloud heating depths (b,d) while the vertical lines denote the distribution mean.	20
2.4	Zonal, meridional (5° N to 5° S lat) and time mean vertical wind profile for two regions, covering the eastern Indian ocean and Indonesia (60° - 160° lon, solid) and South america (280° - 340° lon, dashed). Comparison of ECHAM6-Beres simulation (black) with two reanalysis products: NCEP (orange) and ERA-Interim (blue). ECHAM6-Beres covers 30 years, NCEP 62 years and ERA-Interim 20 years.	21
2.5	Separation of source spectrum into regimes of heating depth H_q . Zonal, meridional (5° N to 5° S lat) and time (5 years) mean source spectrum B for all cloud heating depths (black), shallow cloud heating depths (orange) and deep cloud heating depths (blue).	22
2.6	Influence of convection properties on the source momentum flux B (a) as a function of heating depth. Heating depth distribution (b) and maximum heating rate within a GCM grid box (c) (black) are compared to estimated observations (green) derived from geostationary infrared satellite data and TRMM.	23
3.1	The QBO in ECHAM6-Beres. Timeseries of meridional (5° N to 5° S lat) and zonal mean zonal wind from a 30year model run with a purely convection based gravity wave source parameterization.	26
3.2	QBO composites of meridional (5° N to 5° S lat) and zonal mean zonal wind. Criterion for the composite is the onset of the westerly jet at 20 hPa. Comparison of the gravity wave parameterization with constant sources (ECHAM6-Hines) with the convection based gravity wave parameterization (ECHAM6-Beres) and reanalysis (ERA-Interim).	26
3.3	Variance over time (30 years) of meridional (5° N to 5° S lat) and zonal mean zonal wind. In order to compute the variance of the Semi-annual Oscillation $\text{Var}(U_{SAO})$ in orange and $\text{Var}(U_{QBO})$ in blue, a Fourier transform in time is applied to the winds, the periods between 5 and 7 months (SAO) and between 23 and 35 months (QBO) are selected to calculate each variance contribution. The variance over all periods $\text{Var}(U)$ is depicted in black. Comparison of the gravity wave parameterization with constant sources (ECHAM6-Hines) with the convection based gravity wave parameterization (ECHAM6-Beres) and reanalysis (ERA-Interim). The label on the x-axis shows the maximum value of $\text{Var}(U_{QBO})$	27

- 3.4 Comparison of zonal wind tendency ($\frac{\partial U}{\partial t}|_{GW}$) profiles due to gravity waves in ECHAM6-Beres (orange) with ECHAM6-Hines (blue), tendencies are scaled by density. Maxima in the tendency profiles are highlighted by horizontal lines in according colors, wind profiles are dashed. Zonal and meridional (5°N to 5°S lat) mean over one month. 28
- 3.5 Empirical orthogonal functions (*EOF*) (a)-(c) and principal components (*pc*) (d)-(f) of zonal wind U (a,d), tendency of zonal wind due to gravity waves $\frac{\partial U}{\partial t}|_{GW}$ (b,e) and the total tendency of all components $\frac{\partial U}{\partial t}|_{GW+\nabla \cdot EP+ADV}$ (c,f). The numbers in the legend (a)-(c) indicate the fraction of variance that each EOF accounts for. The *pcs* in (d) are scaled to unit variance, units on individual plots are arbitrary. The *EOFs* and *pcs* of $\frac{\partial U}{\partial t}|_{\nabla \cdot EP}$ and $\frac{\partial U}{\partial t}|_{ADV}$ are not shown individually; they are qualitatively similar to $\frac{\partial U}{\partial t}|_{GWC}$ in (b,e). 29
- 3.6 Sesaonal cycle of progression of QBO phases (blue) and seasonal cycle of amount of zonal wind tendency (orange) for the Beres (a,b) and the Hines scheme (c,d). Comparison of qbo phase progression (blue) with amount of all tendency components (orange) for the Beres (a) and the Hines (c) scheme. Comparison of the individual tendency components of the entire tendency budget for the Beres (b) and the Hines (d) scheme. The drawn tendency is proportional to the actual tendency values, units are arbitrary. Note the two different y-axis in (a,c). 31
- 3.7 Sesaonal cycle of progression of qbo phases ϕ' . The comparison with radiosonde observations from FU Berlin (black) shows an improvement of the convection based gravity wave parameterization in ECHAM6-Beres (orange) over ECHAM6-Hines with a gravity wave parameterization with constant sources (blue). Shaded areas show the 2- σ range. 32
- 4.1 Illustration of the experimental setup. First part of the time axis until Jul 1st shows the generation of an ensemble with similar QBO characteristics (thick gray), the second part of the time axis after Jul 1st shows how the same ensemble reacts differently to El Niño (black) and La Niña (blue) conditions. The upper figure shows the position of the onset of the QBO jet, valid for both an easterly and a westerly jet, the lower figure illustrates the different SSTs to generate the ensemble and the different SSTs during El Niño and La Niña. The actual ensemble comprises 10 members, not three as illustrated in the figure and the actual number of model runs from which the ensemble is drawn is 30, not seven as illustrated in the figure. 38
- 4.2 Timeseries of zonal and meridional mean temperature at 2 *m* (left) and precipitation (right) for El Niño (black) and La Niña (blue) conditions during QBOE phase. Temperature at 2 *m* and precipitation for QBOW phase (not shown) is qualitatively similar to QBOE phase. The shown precipitation is the total precipitation. Solid lines show the ensemble means and shading indicates the range of two standard deviations (2 σ). 40

- 4.3 Vertical component F_z of the spectral EP-Flux vector for El Niño (black) and La Niña (blue) conditions during QBOW phase. Vertical EP-Flux vector F_z for QBOE phase (not shown) is qualitatively similar to QBOW phase. Zonal and meridional mean of F_z , scaled by density ρ , shows the integral over all frequencies and wave numbers. Solid lines show the ensemble means and shading indicates the range of two standard deviations (2σ). Left panel: Vertical profile of time mean F_z for easterly ($c < 0$) and westerly ($c > 0$) waves. Right panel: Timeseries of absolute $|F_z|$ at 86 hPa , with $|F_z| = |F_{z,c<0}| + |F_{z,c>0}|$. 41
- 4.4 Gravity wave source momentum flux B for El Niño (black) and La Niña (blue) conditions during QBOE phase. Gravity wave source momentum flux B for QBOW phase (not shown) is qualitatively similar to QBOE phase. Zonal and meridional mean of B , scaled by density ρ , is determined at the top of convection. Solid lines show the ensemble means and shading indicates the range of two standard deviations (2σ). Left panel: Source spectrum of B as a function of horizontal phasespeed c_p , time mean between October and March. Right panel: Timeseries of total amount of source momentum flux $|B|$ integrated over c_p 42
- 4.5 Upwelling w^* for El Niño (black) and La Niña (blue) conditions during QBOW phase. Upwelling w^* for QBOE phase (not shown) is qualitatively similar to QBOW phase. Zonal and meridional mean between -25° and $+25^\circ$ latitude. Solid lines show the ensemble means and shading indicates the range of two standard deviations (2σ). Left panel: Vertical profile of time mean. Right panel: Timeseries at 30 hPa 43
- 4.6 Evolution of the QBO for El Niño (left) and La Niña (right) conditions during QBOW phase. Timeseries of the profile of meridional and zonal mean zonal wind U for the ensemble mean. 44
- 4.7 Timeseries of the onset of the westerly jet in QBOW for El Niño (black) and La Niña (blue) conditions. Solid lines show the ensemble means and shading indicates the range of two standard deviations (2σ). 44
- 4.8 Timeseries of the strength of the westerly (left) and easterly (right) jet of QBOW for El Niño (black) and La Niña (blue) conditions. Solid lines show the ensemble means and shading indicates the range of two standard deviations (2σ). 45
- 4.9 Evolution of the QBO for El Niño (left) and La Niña (right) conditions during QBOE phase. Timeseries of the profile of meridional and zonal mean zonal wind U for the ensemble mean. 46
- 4.10 Timeseries of the onset of the easterly jet in QBOE for El Niño (black) and La Niña (blue) conditions. Solid lines show the ensemble means and shading indicates the range of two standard deviations (2σ). Note that the ensemble consists of only one member during the last months of La Niña. 46
- 4.11 Timeseries of the strength of the westerly (left) and easterly (right) jet of QBOE for El Niño (black) and La Niña (blue) conditions. Solid lines show the ensemble means and shading indicates the range of two standard deviations (2σ). Note that the ensemble for the westerly jet consists of only one member during the last months of La Niña. 47

4.12	Vertical profile of zonal wind U and its tendency $\frac{\partial U}{\partial t}$ for QBOE in May of the second year for El Niño (black) and La Niña (blue) conditions. Lines show the ensemble means and shading indicates the range of two standard deviations (2σ). Left panel: Zonal wind (dashed), scaled by a factor 100, and total tendency $\frac{\partial U}{\partial t} _{total}$ (solid). Right panel: Tendency components of resolved waves $\frac{\partial U}{\partial t} _{\nabla \cdot EP}$ (solid), gravity waves $\frac{\partial U}{\partial t} _{GW}$ (dashed) and advection $\frac{\partial U}{\partial t} _{ADV}$ (dotted). . . .	48
4.13	Same as figure 4.12, but for October of the first year instead of May of the second year and for QBOW instead of QBOE.	49
4.14	Same as figure 4.12, but for October of the first year instead of May of the second year.	51
5.1	Momentum flux (B) source spectrum as a function of horizontal phase speed (c) for the experiments AD, AD+Beres and ADfixBeres; time, zonal and meridional mean. While the spectra of AD (blue) and ADfixBeres (orange) remain unchanged under AMIP and AMIP4K boundary conditions, the interactive source spectrum of AD+Beres (solid red) changes under the warmer climate of AMIP4K (dashed red). Note that the spectrum of AD is scaled by 0.1 for visualization reasons. ADfixBeres is hidden for the most part by AD+Beres AMIP.	56
5.2	QBO composites for the experiments Hines, AD, AD+Beres and ADfixBeres, each for present day (left column) and warmer climate (right column). The onset of the westerly jet at $20 hPa$ is chosen as the criterion to calculate the composite, compiled from zonal and meridional mean zonal wind.	58
5.3	Distribution of QBO periods for the experiments Hines, AD, AD+Beres and ADfixBeres, each for present day (black) and warmer climate (blue), and the reanalysis ERA-Interim for present day climate. Periods are determined at the onset of the westerly jet at $20 hPa$, compiled from zonal and meridional mean zonal wind. The distribution median is depicted by the horizontal line within each box, the distribution mean by the star whose value is drawn above. The box covers the interquartile range, distribution outliers are denoted by +. . .	59
5.4	Distribution of QBO jet descent rates for the experiments Hines, AD, AD+Beres and ADfixBeres, each for present day (black) and warmer climate (blue), compiled from zonal and meridional mean zonal wind. The descent rate is determined for the westerly (W) and easterly (E) jet by calculating the time the wind maxima take from $8 hPa$ until $45 hPa$. The difference (AMIP4K-AMIP) in the mean is drawn above. For details on box properties see figure 5.3.	59
5.5	Vertical QBO amplitude profiles for the experiments Hines, AD, AD+Beres and ADfixBeres, each for present day (black) and warmer climate (blue), compiled from zonal and meridional mean zonal wind. The amplitude is calculated as the mean maximum wind speed of the QBO easterly ($U < 0$) and westerly ($U > 0$) jets on each vertical level. The shading illustrates the range of two standard deviations σ . The labels on the x-axis show the maximum value of the AMIP profiles.	60

- 5.6 Vertical profile of vertical component F_z of the spectral EP-Flux vector for the experiments Hines, AD, AD+Beres and ADfixBeres; time (10years, based on 6 hourly data), zonal and meridional mean. F_z shows the integral over frequencies and wave numbers. Left panel: F_z of easterly ($c < 0$) and westerly ($c > 0$) waves for present day (solid) and warmer climate (dashed). Center panel: Change of the absolute value $\Delta|F_z| = |F_z|_{AMIP4K} - |F_z|_{AMIP}$ from present day climate to the warmer climate, with $|F_z| = |F_{z,c<0}| + |F_{z,c>0}|$. Right Panel: Standard deviation σ of $\Delta|F_z|$ of the four parameterization setups. 61
- 5.7 Vertical profile of residual vertical velocity w^* of a transformed Eulerian mean analysis for the experiments Hines, AD, AD+Beres and ADfixBeres; time, zonal and meridional ($\pm 25^\circ$ latitude) mean data. Left panel: w^* for present day (solid) and warmer climate (dashed). Center panel: Increase of w^* from present day climate to warmer climate, with $\Delta w^* = w^*_{AMIP4K} - w^*_{AMIP}$. Right Panel: Standard deviation σ of Δw^* of the four parameterization setups. 62
- 5.8 Vertical profile of gravity wave momentum flux (B) for the experiments Hines, AD, AD+Beres and ADfixBeres; time, zonal and meridional mean data. Left panel: B of easterly ($c < 0$) and westerly ($c > 0$) for present day (solid) and warmer climate (dashed). Right panel: Change of total momentum flux $\Delta|B| = |B|_{AMIP4K} - |B|_{AMIP}$, with $|B| = |B_{c<0}| + |B_{c>0}|$ 63
- 5.9 Vertical profile of zonal wind tendency due to gravity waves ($\frac{\partial U}{\partial t}|_{GW}$) for the experiments Hines, AD, AD+Beres and ADfixBeres; time, zonal and meridional mean data; $\frac{\partial U}{\partial t}$ is scaled by density ρ . Left panel: Absolute tendency due to gravity waves with $|\frac{\partial U}{\partial t}|_{GW} = |\frac{\partial U}{\partial t}|_{GW,c>0} + |\frac{\partial U}{\partial t}|_{GW,c<0}$ for present day (solid) and warmer climate (dashed). Right panel: Relative change of absolute tendency due to gravity waves $\Delta|\frac{\partial U}{\partial t}|_{GW}$ 64

List of Tables

4.1	Overview of number of ensemble members for the experimental setup with two initial QBO phases (QBOW and QBOE) and two different ENSO boundary conditions (El Niño and La Niña).	39
5.1	Overview of different gravity wave parameterization setups: The experiment acronym as used in this work, the propagation scheme, the intermittency value ϵ of the propagation scheme AD99, the horizontal wavelength λ_h , the nature of momentum flux sources (interactive or prescribed), the waves' launch level, details on the symmetry of the source spectrum and the phase speed c_{max} where the momentum flux source spectrum peaks. Note that "as AD+Beres" refers to the zonal, meridional and time mean.	54

References

- Alexander, M. and Barnett, C. (2007). Using satellite observations to constrain parameterizations of gravity wave effects for global models. *Journal of the atmospheric sciences*, pages 1652–1665.
- Alexander, M. and Holton, J. (1997). A model study of zonal forcing in the equatorial stratosphere by convectively induced gravity waves. *Journal of the atmospheric sciences*, 54:408–419.
- Alexander, M. J. and Dunkerton, T. J. (1999). A spectral parameterization of mean-flow forcing due to breaking gravity waves. *Journal of the Atmospheric Sciences*, 56(24):4167–4182.
- Alexander, M. J., Geller, M., McLandress, C., Polavarapu, S., Preusse, P., Sassi, F., Sato, K., Eckermann, S., Ern, M., Hertzog, A., Kawatani, Y., Pulido, M., Shaw, T. a., Sigmund, M., Vincent, R., and Watanabe, S. (2010). Recent developments in gravity-wave effects in climate models and the global distribution of gravity-wave momentum flux from observations and models. *Quarterly Journal of the Royal Meteorological Society*, 136(July):1103–1124.
- Alexander, M. J., Richter, J. H., and Sutherland, B. R. (2006). Generation and Trapping of Gravity Waves from Convection with Comparison to Parameterization. *Journal of the Atmospheric Sciences*, 63(11):2963–2977.
- Angell, J. K. (1986). On the Variation in Period and Amplitude of the Quasi-biennial Oscillation in the Equatorial Stratosphere, 1951-85. *Monthly Weather Review*, 114:2272–2278.
- Baldwin, M., Gray, L., Dunkerton, T. J., Hamilton, K., Haynes, P. H., Randel, W. J., Holton, J. R., Alexander, M. J., Hirota, I., Horinouchi, T., Jones, D. B. A., Kinnerson, J. S., Marquardt, C., Sato, K., and Takahashi, M. (2001). The quasibiennial oscillation. *Reviews of Geophysics*, 39(2):179–229.
- Baldwin, M. P. and Dunkerton, T. J. (2001). Stratospheric harbingers of anomalous weather regimes. *Science (New York, N.Y.)*, 294(5542):581–4.
- Barnett, T. (1991). The interaction of multiple time scales in the tropical climate system. *Journal of Climate*, 4:269–285.
- Bender, F. (2008). A note on the effect of GCM tuning on climate sensitivity. *Environmental Research Letters*, 3(1):014001.

- Beres, J., Alexander, M. J., and Holton, J. R. (2002). Effects of tropospheric wind shear on the spectrum of convectively generated gravity waves. *Journal of the atmospheric sciences*, 59(1998):1805–1824.
- Beres, J. H. (2004). Gravity Wave Generation by a Three-Dimensional Thermal Forcing. *Journal of the Atmospheric Sciences*, 61(14):1805–1815.
- Beres, J. H., Alexander, M. J., and Holton, J. R. (2004). A Method of Specifying the Gravity Wave Spectrum above Convection Based on Latent Heating Properties and Background Wind. *Journal of the Atmospheric Sciences*, 61(3):324–337.
- Beres, J. H., Garcia, R. R., Boville, B. a., and Sassi, F. (2005). Implementation of a gravity wave source spectrum parameterization dependent on the properties of convection in the Whole Atmosphere Community Climate Model (WACCM). *Journal of Geophysical Research*, 110(D10):1–13.
- Bergman, J. and Salby, M. (1994). Equatorial wave activity derived from fluctuations in observed convection. *Journal of the atmospheric sciences*, 51(24):3791–3806.
- Brewer, A. (1949). Evidence for a world circulation provided by the measurements of helium and water vapour distribution in the stratosphere. *Quarterly Journal of the Royal Meteorological Society*, 75:351–363.
- Calvo, N., Giorgetta, M. A., and Pena-Ortiz, C. (2010). Impact of warm ENSO events on the tropical QBO using MAECHAM5 simulations. *Poster at EGU Conference 2010*.
- Charron, M. and Manzini, E. (2002). Gravity Waves from Fronts: Parameterization and Middle Atmosphere Response in a General Circulation Model. *Journal of the Atmospheric Sciences*, 59(5):923–941.
- Choi, H.-J. and Chun, H.-Y. (2011). Momentum Flux Spectrum of Convective Gravity Waves. Part I: An Update of a Parameterization Using Mesoscale Simulations. *Journal of the Atmospheric Sciences*, 68(4):739–759.
- Chun, H.-Y. and Baik, J.-J. (2002). An Updated Parameterization of Convectively Forced Gravity Wave Drag for Use in Large-Scale Models. *Journal of the Atmospheric Sciences*, 59(5):1006–1017.
- Collimore, C., Martin, D., Hitchman, M., Huesmann, A., and Waliser, D. (2003). On the relationship between the QBO and tropical deep convection. *Journal of climate*, 16(15):2552–2568.
- Dee, D. P., Uppala, S. M., Simmons, a. J., Berrisford, P., Poli, P., Kobayashi, S., Andrae, U., Balmaseda, M. a., Balsamo, G., Bauer, P., Bechtold, P., Beljaars, a. C. M., van de Berg, L., Bidlot, J., Bormann, N., Delsol, C., Dragani, R., Fuentes, M., Geer, a. J., Haimberger, L., Healy, S. B., Hersbach, H., Hólm, E. V., Isaksen, L., Kållberg, P., Köhler, M., Matricardi, M., McNally, a. P., Monge-Sanz, B. M., Morcrette, J.-J., Park, B.-K., Peubey, C., de Rosnay, P., Tavolato, C., Thépaut, J.-N., and Vitart, F. (2011). The ERA-Interim reanalysis: configuration and performance of

- the data assimilation system. *Quarterly Journal of the Royal Meteorological Society*, 137(656):553–597.
- Dobson, G. (1956). Origin and distribution of the polyatomic molecules in the atmosphere. *Proceedings of the Royal Society of London. Series A*, 236(1205):187–193.
- Dunkerton, T. and Baldwin, M. (1991). Quasi-biennial modulation of planetary-wave fluxes in the Northern Hemisphere winter. *Journal of the Atmospheric Sciences*, 48(8):1043–1061.
- Dunkerton, T. J. (1997). The role of gravity waves in the quasi-biennial oscillation. *Journal of Geophysical Research*, 102(D22):26053–26076.
- Ern, M., Ploeger, F., and Preusse, P. (2014). Interaction of gravity waves with the QBO: A satellite perspective. *Journal of Geophysical Research: Atmospheres*, 119:2329–2355.
- Evan, S., Alexander, M. J., and Dudhia, J. (2012). WRF simulations of convectively generated gravity waves in opposite QBO phases. *Journal of Geophysical Research: Atmospheres*, 117(D12):1–17.
- Fritts, D. C. and Alexander, M. (2003). Gravity wave dynamics and effects in the middle atmosphere. *Reviews of Geophysics*, 41(1):1–64.
- Geller, M. a., Alexander, M. J., Love, P. T., Bacmeister, J., Ern, M., Hertzog, A., Manzini, E., Preusse, P., Sato, K., Scaife, A. a., and Zhou, T. (2013). A Comparison Between Gravity Wave Momentum Fluxes in Observations and Climate Models. *Journal of Climate*, 26(17):6383–6405.
- Geller, M. a., Zhou, T., Ruedy, R., Aleinov, I., Nazarenko, L., Tausnev, N. L., Sun, S., Kelley, M., and Cheng, Y. (2011). New Gravity Wave Treatments for GISS Climate Models. *Journal of Climate*, 24(15):3989–4002.
- Giorgetta, M. a., Bengtsson, L., and Arpe, K. (1999). An investigation of QBO signals in the east Asian and Indian monsoon in GCM experiments. *Climate Dynamics*, 15(6):435–450.
- Giorgetta, M. a. and Doege, M. C. (2005). Sensitivity of the quasi-biennial oscillation to CO₂ doubling. *Geophysical Research Letters*, 32:L08701.
- Giorgetta, M. a., Jungclaus, J., Reick, C. H., Legutke, S., Bader, J., Böttinger, M., Brovkin, V., Crueger, T., Esch, M., Fieg, K., Glushak, K., Gayler, V., Haak, H., Hollweg, H.-D., Ilyina, T., Kinne, S., Kornblueh, L., Matei, D., Mauritsen, T., Mikolajewicz, U., Mueller, W., Notz, D., Pithan, F., Raddatz, T., Rast, S., Redler, R., Roeckner, E., Schmidt, H., Schnur, R., Segschneider, J., Six, K. D., Stockhause, M., Timmreck, C., Wegner, J., Widmann, H., Wieners, K.-H., Claussen, M., Marotzke, J., and Stevens, B. (2013). Climate and carbon cycle changes from 1850 to 2100 in MPI-ESM simulations for the coupled model intercomparison project phase 5. *Journal of Advances in Modeling Earth Systems*, 5:1–26.

- Giorgetta, M. A., Manzini, E., and Roeckner, E. (2002). Forcing of the quasi-biennial oscillation from a broad spectrum of atmospheric waves. *Geophysical Research Letters*, 29(8):8–11.
- Gregory, J. M., Ingram, W. J., Palmer, M. A., Jones, G. S., Stott, P. A., Thorpe, R. B., Lowe, J. A., Johns, T. C., and Williams, K. D. (2004). A new method for diagnosing radiative forcing and climate sensitivity. *Geophysical Research Letters*, 31(3):L03205.
- Grimsdell, A. W., Alexander, M. J., May, P. T., and Hoffmann, L. (2010). Model Study of Waves Generated by Convection with Direct Validation via Satellite. *Journal of the Atmospheric Sciences*, 67(5):1617–1631.
- Gu, G., Adler, R. F., Huffman, G. J., and Curtis, S. (2007). Tropical Rainfall Variability on Interannual-to-Interdecadal and Longer Time Scales Derived from the GPCP Monthly Product. *Journal of Climate*, 20(15):4033–4046.
- Hamilton, K., Wilson, R. J., and Hemler, R. S. (1999). atmosphere simulated with high vertical and horizontal resolution versions of a GCM: Improvements in the cold pole bias and generation of a QBO-like oscillation in. *Journal of the Atmospheric Sciences*, 56(22):3829–3846.
- Hansen, J., Lacis, A., and Rind, D. (1984). Climate sensitivity: Analysis of feedback mechanisms. *Climate Processes and Climate Sensitivity*, 5:130–163.
- Hardiman, S. C., Butchart, N., Haynes, P. H., and Hare, S. H. E. (2007). A note on forced versus internal variability of the stratosphere. *Geophysical Research Letters*, 34(12):L12803.
- Hines, C. (1997a). Doppler-spread parameterization of gravity-wave momentum deposition in the middle atmosphere. Part 1: Basic formulation. *Journal of Atmosphere and Solar-Terrestrial Physics*, 59(4):371–386.
- Hines, C. (1997b). Doppler-spread parameterization of gravity-wave momentum deposition in the middle atmosphere. Part 2: Broad and quasi monochromatic spectra, and implementation. *Journal of Atmosphere and Solar-Terrestrial Physics*, 59(4):387–400.
- Ho, C.-H., Kim, H.-S., Jeong, J.-H., and Son, S.-W. (2009). Influence of stratospheric quasi-biennial oscillation on tropical cyclone tracks in the western North Pacific. *Geophysical Research Letters*, 36(6):1–4.
- Holton, J. and Alexander, M. (1999). Gravity waves in the mesosphere generated by tropospheric convection. *Tellus A*, 51A-B:45–58.
- Holton, J. and Lindzen, R. (1972). An updated theory for the quasi-biennial cycle of the tropical stratosphere. *Journal of Atmospheric Sciences*, pages 1076–1080.
- Holton, J. and Tan, H. (1980). The influence of the equatorial quasi-biennial oscillation on the global circulation at 50 mb. *Journal of the Atmospheric Sciences*, 37:2200–2208.

- Jewtoukoff, V., Plougonven, R., and Hertzog, A. (2013). Gravity waves generated by deep tropical convection: estimates from balloon observations and mesoscale simulations. *Journal of Geophysical Research: Atmospheres*, 118:9690–9707.
- Kane, R. (1992). Relationship between QBOs of stratospheric winds, ENSO variability and other atmospheric parameters. *International journal of climatology*, 12:435–447.
- Kane, R. P. (2004). Comparison of Stratospheric Zonal Winds and El NiñoSouthern Oscillation in Recent Decades. *International Journal of Climatology*, 24(4):525–532.
- Kawatani, Y. and Hamilton, K. (2013). Weakened stratospheric quasibiennial oscillation driven by increased tropical mean upwelling. *Nature*, 497(7450):478–81.
- Kawatani, Y., Hamilton, K., and Noda, A. (2012). The Effects of Changes in Sea Surface Temperature and CO₂ Concentration on the Quasi-Biennial Oscillation. *Journal of the Atmospheric Sciences*, 69(5):1734–1749.
- Kawatani, Y., Hamilton, K., and Watanabe, S. (2011). The Quasi-Biennial Oscillation in a Double CO₂ Climate. *Journal of the Atmospheric Sciences*, 68(2):265–283.
- Kim, Y.-H., Bushell, a. C., Jackson, D. R., and Chun, H.-Y. (2013). Impacts of introducing a convective gravity-wave parameterization upon the QBO in the Met Office Unified Model. *Geophysical Research Letters*, 40(9):1873–1877.
- Kistler, R., Collins, W., Saha, S., White, G., Woollen, J., Kalnay, E., Chelliah, M., Ebisuzaki, W., Kanamitsu, M., Kousky, V., van den Dool, H., Jenne, R., and Fiorino, M. (2001). The NCEPNCAR 50Year Reanalysis: Monthly Means CDROM and Documentation. *Bulletin of the American Meteorological Society*, 82(2):247–267.
- Klocke, D., Pincus, R., and Quaas, J. (2011). On Constraining Estimates of Climate Sensitivity with Present-Day Observations through Model Weighting. *Journal of Climate*, 24(23):6092–6099.
- Krismer, T. R. and Giorgetta, M. a. (2014). Wave Forcing of the Quasi-Biennial Oscillation in the Max Planck Institute Earth System Model. *Journal of the Atmospheric Sciences*, page 140214114452004.
- Krismer, T. R., Giorgetta, M. a., and Esch, M. (2013). Seasonal aspects of the quasi-biennial oscillation in MPI-ESM and ERA-40. *Journal of Advances in Modeling Earth Systems*, 5:406–421.
- Kuester, M. a., Alexander, M. J., and Ray, E. a. (2008). A Model Study of Gravity Waves over Hurricane Humberto (2001). *Journal of the Atmospheric Sciences*, 65(10):3231–3246.
- Lane, T., Reeder, M., and Clark, T. (2001). Numerical modeling of gravity wave generation by deep tropical convection. *Journal of the atmospheric sciences*, 58:1249–1274.
- Liess, S. and Geller, M. a. (2012). On the relationship between QBO and distribution of tropical deep convection. *Journal of Geophysical Research*, 117(D3):1–12.

- Lindzen, R. (1981). Turbulence and stress owing to gravity wave and tidal breakdown. *Journal of Geophysical Research*, 86:9707–9714.
- Lindzen, R. and Holton, J. (1968). A theory of the quasi-biennial oscillation. *Journal of the Atmospheric Sciences*, 25:1095–1107.
- Lott, F. and Guez, L. (2013). A stochastic parameterization of the gravity waves due to convection and its impact on the equatorial stratosphere. *Journal of Geophysical Research: Atmospheres*, 118:8897–8909.
- Lott, F. and Miller, M. (1997). A new subgridscale orographic drag parametrization: Its formulation and testing. *Quarterly Journal of the Royal Meteorological Society*, 123:101–127.
- Mauritsen, T., Stevens, B., Roeckner, E., Crueger, T., Esch, M., Giorgetta, M., Haak, H., Jungclaus, J., Klocke, D., Matei, D., Mikolajewicz, U., Notz, D., Pincus, R., Schmidt, H., and Tomassini, L. (2012). Tuning the climate of a global model. *Journal of Advances in Modeling Earth Systems*, 4(3):1–18.
- McFarlane, N. (1987). The effect of orographically excited gravity wave drag on the general circulation of the lower stratosphere and troposphere. *Journal of the atmospheric sciences*, 44(14):1775–1800.
- McLandress, C., Alexander, M. J., and Wu, D. L. (2000). Microwave Limb Sounder observations of gravity waves in the stratosphere: A climatology and interpretation. *Journal of Geophysical Research*, 105(D9):11947.
- McLandress, C. and Scinocca, J. (2005). The GCM response to current parameterizations of nonorographic gravity wave drag. *Journal of the atmospheric sciences*, 62(7):2394–2413.
- Nordeng, T. E. (1996). Extended versions of the convective parametrization scheme at ECMWF and their impact on the mean and transient activity of the model in the tropics. *Tech. Memo 206*, (Res. Dep., Eur. Cent. for Medium-Range Weather Forecasting, Reading, UK).
- Ortland, D. a. and Alexander, M. J. (2006). Gravity wave influence on the global structure of the diurnal tide in the mesosphere and lower thermosphere. *Journal of Geophysical Research*, 111(A10S10):1–15.
- Ortland, D. a. and Alexander, M. J. (2014). The Residual-Mean Circulation in the Tropical Tropopause Layer Driven by Tropical Waves. *Journal of the Atmospheric Sciences*, 71(4):1305–1322.
- Ortland, D. a., Alexander, M. J., and Grimsdell, A. W. (2011). On the Wave Spectrum Generated by Tropical Heating. *Journal of the Atmospheric Sciences*, 68(9):2042–2060.
- Pfister, L., Scott, S., Lowenstein, M., Bowen, S., and Legg, M. (1993). Mesoscale Disturbances in the Tropical Stratosphere Excite by Convection: Observations and

- Effects on the Stratospheric Momentum Budget. *Journal of the atmospheric sciences*, 50(8):1058–1075.
- Piani, C. and Durran, D. (2001). A numerical study of stratospheric gravity waves triggered by squall lines observed during the TOGA COARE and COPT-81 experiments. *Journal of the atmospheric sciences*, 58(1997):3702–3723.
- Piani, C., Durran, D., Alexander, M. J., and Holton, J. R. (2000). A Numerical Study of Three-Dimensional Gravity Waves Triggered by Deep Tropical Convection and Their Role in the Dynamics of the QBO. *Journal of the Atmospheric Sciences*, 57(22):3689–3702.
- Plumb, R. (1977). The interaction of two internal waves with the mean flow: Implications for the theory of the quasi-biennial oscillation. *Journal of the Atmospheric Sciences*, 34(12):1847–1858.
- Plumb, R. and Bell, R. (1982). A model of the quasibiennial oscillation on an equatorial betaplane. *Quarterly Journal of the Royal Meteorological Society*, 108:335–352.
- Plumb, R. and McEwan, A. (1978). The Instability of a Forced Standing Wave in a Viscous Stratified Fluid: A Laboratory Analogue of the Quasi-Biennial Oscillation. *Journal of the atmospheric sciences*, 35:1827–1839.
- Plumb, R. A. (1984). The quasi-biennial oscillation, in *Dynamics of the Middle Atmosphere*, edited by J. R. Holton and T. Matsuno. *Terra Science, Tokyo*, pages 217–251.
- Pohlmann, H., Müller, W. a., Kulkarni, K., Kameswarrao, M., Matei, D., Vamborg, F. S. E., Kadow, C., Illing, S., and Marotzke, J. (2013). Improved forecast skill in the tropics in the new MiKlip decadal climate predictions. *Geophysical Research Letters*, 40(21):5798–5802.
- Randel, W. and Cobb, J. (1994). Coherent variations of monthly mean total ozone and lower stratospheric temperature. *Journal of Geophysical Research: Atmospheres*, 99(D3):5433–5447.
- Randel, W. J., Garcia, R. R., Calvo, N., and Marsh, D. (2009). ENSO influence on zonal mean temperature and ozone in the tropical lower stratosphere. *Geophysical Research Letters*, 36(15):1–5.
- Richter, J. (2014). On the simulation of the quasi-biennial oscillation in the Community Atmosphere Model, version 5. *Journal of Geophysical Research: Atmospheres*, 119:3045–3062.
- Richter, J. H., Sassi, F., and Garcia, R. R. (2010). Toward a Physically Based Gravity Wave Source Parameterization in a General Circulation Model. *Journal of the Atmospheric Sciences*, 67(1):136–156.
- Ryu, J.-H., Alexander, M. J., and Ortland, D. a. (2011). Equatorial Waves in the Upper Troposphere and Lower Stratosphere Forced by Latent Heating Estimated from TRMM Rain Rates. *Journal of the Atmospheric Sciences*, 68(10):2321–2342.

- Salby, M. and Garcia, R. (1987). Transient response to localized episodic heating in the tropics. Part I: Excitation and short-time near-field behavior. *Journal of the atmospheric sciences*, 44(2):458–498.
- Saravanan, R. (1990). A multiwave model of the quasi-biennial oscillation. *Journal of the atmospheric sciences*, 47(21):2465–2474.
- Sato, K. and Dunkerton, T. (1997). Estimates of momentum flux associated with equatorial Kelvin and gravity waves. *Journal of geophysical research*, 102(D22):26,247–26,261.
- Scaife, A., Athanassiadou, M., Andrews, M., Arribas, A., Baldwin, M., Dunstone, N., Knight, J., MacLachlan, C., Manzini, E., Mueller, W., Pohlmann, H., Smith, D., Stockdale, T., and Williams, A. (2014). Predictability of the quasibiennial oscillation and its northern winter teleconnection on seasonal to decadal timescales. *Geophysical Research Letters*, 41:1–7.
- Scaife, A., Butchart, N., Warner, C. D., Stainforth, D., Norton, W., and Austin, J. (2000). Realistic quasi biennial oscillations in a simulation of the global climate. *Geophysical Research Letters*, 27(21):3481–3484.
- Schirber, S., Manzini, E., and Alexander, M. J. (2014). A convection based gravity wave parameterization in a general circulation model: Implementation and improvements on the QBO. *Journal of Advances in Modeling Earth Systems*, 6:264–279.
- Schmidt, H., Rast, S., Bunzel, F., Esch, M., Giorgetta, M., Kinne, S., Krismer, T., Stenchikov, G., Timmreck, C., Tomassini, L., and Walz, M. (2013). Response of the middle atmosphere to anthropogenic and natural forcings in the CMIP5 simulations with the Max Planck Institute Earth system model. *Journal of Advances in Modeling Earth Systems*, 5(1):98–116.
- Shibata, K. and Deushi, M. (2005). Partitioning between resolved wave forcing and unresolved gravity wave forcing to the quasi-biennial oscillation as revealed with a coupled chemistry-climate model. *Geophysical Research Letters*, 32(12):L12820.
- Soden, B. (2000). The sensitivity of the tropical hydrological cycle to ENSO. *Journal of Climate*, 13:538–549.
- Song, I., Chun, H., and Lane, T. (2003). Generation mechanisms of convectively forced internal gravity waves and their propagation to the stratosphere. *Journal of the atmospheric sciences*, 60:1960–1980.
- Stainforth, D. a., Aina, T., Christensen, C., Collins, M., Faull, N., Frame, D. J., Kettleborough, J. a., Knight, S., Martin, A., Murphy, J. M., Piani, C., Sexton, D., Smith, L. a., Spicer, R. a., Thorpe, a. J., and Allen, M. R. (2005). Uncertainty in predictions of the climate response to rising levels of greenhouse gases. *Nature*, 433(7024):403–6.
- Stevens, B., Giorgetta, M., Esch, M., Mauritsen, T., Crueger, T., Rast, S., Salzmann, M., Schmidt, H., Bader, J., Block, K., Brokopf, R., Fast, I., Kinne, S., Kornblueh,

- L., Lohmann, U., Pincus, R., Reichler, T., and Roeckner, E. (2013). Atmospheric component of the MPIM Earth System Model: ECHAM6. *Journal of Advances in Modeling Earth Systems*, 5:1–27.
- Taguchi, M. (2010). Observed connection of the stratospheric quasi-biennial oscillation with El Niño/Southern Oscillation in radiosonde data. *Journal of Geophysical Research*, 115(D18):1–12.
- Taylor, K. E., Stouffer, R. J., and Meehl, G. a. (2012). An Overview of CMIP5 and the Experiment Design. *Bulletin of the American Meteorological Society*, 93(4):485–498.
- Tiedtke, M. (1989). A comprehensive mass flux scheme for cumulus parameterization in large-scale models. *Monthly Weather Review*, 117(8):1779–1800.
- Trenberth, K. (1997). The definition of el nino. *Bulletin of the American Meteorological Society*, (August):2771–2777.
- Trenberth, K. and Caron, J. (2000). The Southern Oscillation revisited: Sea level pressures, surface temperatures, and precipitation. *Journal of Climate*, (1974):4358–4365.
- Tsuda, T., Ratnam, M. V., Alexander, S. P., Kozu, T., and Takayabu, Y. (2009). Temporal and spatial distributions of atmospheric wave energy in the equatorial stratosphere revealed by GPS radio occultation temperature data obtained with the CHAMP satellite during 2001–2006. *Earth Planets and Space*, 61:525–533.
- Wallace, J., Panetta, R., and Estberg, J. (1993). Representation of the equatorial stratospheric quasi-biennial oscillation in EOF phase space. *Journal of the atmospheric sciences*, 50(12):1751–1762.
- Wang, C. and Fiedler, P. C. (2006). ENSO variability and the eastern tropical Pacific: A review. *Progress in Oceanography*, 69(2-4):239–266.
- Wang, L. and Alexander, M. J. (2010). Global estimates of gravity wave parameters from GPS radio occultation temperature data. *Journal of Geophysical Research*, 115(D21122).
- Wang, L. and Geller, M. A. (2003). Morphology of gravity-wave energy as observed from 4 years (1998–2001) of high vertical resolution U.S. radiosonde data. *Journal of Geophysical Research*, 108(D16):ACL 1–1–ACL 1–12.
- Watanabe, S. (2005). Kelvin waves and ozone Kelvin waves in the quasi-biennial oscillation and semiannual oscillation: A simulation by a high-resolution chemistry-coupled general circulation model. *Journal of Geophysical Research*, 110(D18):D18303.
- Watanabe, S. and Kawatani, Y. (2012). Sensitivity of the QBO to Mean Tropical Upwelling under a Changing Climate Simulated with an Earth System Model. *Journal of the Meteorological Society of Japan*, 90A:351–360.

- Watanabe, S. and Miura, H. (2008). Development of an atmospheric general circulation model for integrated Earth system modeling on the Earth Simulator. *Journal of the Earth Simulator*, 9(March):27–35.
- Yuan, W., Geller, M. a., and Love, P. T. (2013). ENSO influence on QBO modulations of the tropical tropopause. *Quarterly Journal of the Royal Meteorological Society*.

Aus dieser Dissertation hervorgegangene Veröffentlichungen

Schirber, S., E. Manzini, and M. J. Alexander (2014), A convection-based gravity wave parameterization in a general circulation model: Implementation and improvements on the QBO, *J. Adv. Model. Earth Syst.*, 6, 264279, doi:10.1002/2013MS000286.

Schirber, S., E. Manzini, T. Krismer and M. Giorgetta (2014), The Quasi-Biennial Oscillation in a warmer climate: Sensitivity to different gravity wave parameterizations, submitted to *Climate Dynamics*.

Schirber, S. (2014), S., How El Niño / Southern Oscillation modulates the Quasi-Biennial Oscillation: Results from a general circulation model, submitted to *JGR*.

Erklärung

Hiermit erkläre ich an Eides statt, dass ich die vorliegende Dissertationsschrift selbst verfasst und keine anderen als die angegebenen Quellen und Hilfsmittel benutzt habe.

Hamburg, den 18. August 2014

Hinweis / Reference

Die gesamten Veröffentlichungen in der Publikationsreihe des MPI-M
„Berichte zur Erdsystemforschung / Reports on Earth System Science“,
ISSN 1614-1199

sind über die Internetseiten des Max-Planck-Instituts für Meteorologie erhältlich:
<http://www.mpimet.mpg.de/wissenschaft/publikationen.html>

*All the publications in the series of the MPI -M
„Berichte zur Erdsystemforschung / Reports on Earth System Science“,
ISSN 1614-1199*

*are available on the website of the Max Planck Institute for Meteorology:
<http://www.mpimet.mpg.de/wissenschaft/publikationen.html>*

